Online ISSN: 1920-3853

Vol. 15, No. 3, October 2021
Print ISSN : 1715-9997

Canadian Journal of pure & applied sciences

an International Journal

Published three times a year (Feb, June and Oct.)

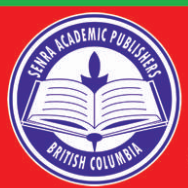

SENRA
Academic Publishers, British Columbia

Print ISSN 1715-9997
Online ISSN 1920-3853

Volume 15, Number 2
June 2021

CANADIAN JOURNAL OF PURE AND APPLIED SCIENCES

The Canadian Journal of Pure and Applied Sciences (CJPAS) is a peer reviewed multi-disciplinary international journal aimed at promoting research in all field of science and technology on the basis of its originality. The CJPAS is indexed in major indexing databases of different indexing services and universities.

Every effort is made by the editors, board of editorial advisors and publishers to see that no inaccurate or misleading data, opinions, or statements appear in this journal, they wish to make clear that data and opinions appearing in the articles are the sole responsibility of the contributor concerned. The CJPAS accept no responsibility for the misleading data, opinion or statements.

The CJPAS is Abstracted/ Indexed in several indexing databases of different indexing services and universities.

Four Years Global Impact Factor
2012 2.657, 2013 2.756,
2014 2.845, 2015 2.988

Frequency:
3 times a year (Feb, June and Oct.)

Editorial Office
E-mail: editor@cjpas.ca, editor@cjpas.net

SENRA Academic Publishers
5919 129 B Street Surrey
British Columbia V3X 0C5 Canada
www.cjpas.net
E-mail: senra@cjpas.ca

BOARD OF EDITORIAL ADVISORS

Canadian Journal of pure & applied sciences

Volume 15, Number 3
October 2021

CONTENTS

Canadian Journal of Pure and Applied Sciences
Vol. 15, No. 3, pp. 5283-5295, Oct 2021
Online ISSN: 1920-3853; Print ISSN: 1715-9997
Available online at www.cjpas.net

Canadian Journal of pure&applied sciences

AN ALTERNATIVE TO UNDERSTAND THE ORIGIN OF UNIVERSAL GRAVITATION AND THE COSMIC BACKGROUND MICROWAVE RADIATION FROM A SUPER PHOTON THEORY

Wenzhong David Zhang
Hembury Avenue, Manchester, M19 1FH, UK

ABSTRACT

Through analysing the interactions between the immersed matter particles and the thermal bath of a vast Super photon ocean, the Super photon theory is developed quantitatively. The correlation between the Gravitational constant and the Hubble constant is deduced. The generalised law of Universal Gravitation, the Tully-Fisher law, and the Modified Newtonian Dynamics relation are derived theoretically. The dynamic equilibrium and circulation of mass and energy of the Universe are discussed. Flavour oscillation observed in neutrinos is taken as an evidence of immersed matter particles that undergo two-way energy exchange with the thermal bath of the vast Super photon ocean having local fluctuations. Gravitational waves are viewed as periodic density and pressure oscillations of the Super photon particles propagating through the vast Super photon ocean. The temperature and the spectrum of the Cosmic Microwave Background Radiation are explained theoretically and determined accurately using the Super photon theory together with the fluctuation-dissipation theorem. The capability of a photon particle travelling at the constant speed of light in the free space with a friction force is verified theoretically. Further supporting evidences to the Super photon theory are provided. An experiment is proposed for the further proof of the Super photon theory.

Keywords: Universal Gravitation, super photon, dynamic equilibrium and circulation, Tully-Fisher law, modified Newtonian dynamics, cosmic background microwave radiation, fluctuation-dissipation theorem.

INTRODUCTION

It is interesting to know that Hubble remained cautiously against the Big-Bang hypothesis until the end of his life. In order to account for cosmic redshifts in a nonexpanding Universe, Hubble called for a new principle of nature, like the kind of Tired-Light mechanism (Hubble, 1937; Assis, 1992). On the other hand, he was aware of the theoretical difficulties of such a radical assumption that was in conflict with Einstein's General Relativity. The differential geometry used in Einstein's General Relativity is technically useful and predictive, however, it has limitations. Einstein's General Relativity spring out of Maxwell's equations, hence, the ideal approximations of massless photon and frictionless free space are inherited, it also does not include the self-rotational effect (Zhang, 2021a, 2021b). The dynamic absorption and dissipation of energy are not handled by the geometric theory of gravitation (the General Relativity.)

Photon particles propagate at constant velocities (c and v) in the free space and other spaces of transparent media (Pound and Rebka, 1960; Broberg, 1993; Kardar and Golestanian, 1999; Manjavacas and García, 2010). They interact with each other, although the interactions are extremely weak. Photon particles experience an extremely weak force (F_{vis}) resembling friction in the spaces they travelling through (Zhang, 2021a, 2021b), i.e.

$$F_{vis} = -R_m v \quad (1)$$

where R_m is the viscous resistance coefficient of the space, v is the constant velocity of the photon particle travelling through the space. From a mechanical perspective, a lightly damped oscillator model was applied to elucidate the properties and propagations of the photon particles in the free space. Based on the analysis of the lightly damped oscillator model for the photon particles, an alternative for the understanding of the physical origin of the Cosmic Redshift and the Hubble constant were elucidated. An equation was deduced displaying the exponential relationship between the Cosmic Redshift z and the Hubble constant H with clearly defined physical meaning of every parameter involved (Zhang, 2021a). The Hubble constant was derived as an extremely low frequency with its origin from the time constant, the ratio between the viscous resistance R_m of the free space and the inertial mass m of the photon particle travelling through, i.e.

Corresponding author e-mail: WenzhongZhang2008@gmail.com

$$H \approx f_\tau = \frac{1}{\tau} = \frac{R_m}{2m} \quad (2)$$

The energy dissipated by a photon particle during one cycle was deduced as the product of the Planck constant and the Hubble constant, which was defined as a Super photon (Zhang, 2021a, 2021b). A Super photon is a fundamental unit of energy and mass in dynamic circulation. There is an unnoticeable and vast Super photon ocean in the Universe. The normal photons and the Super photons in gigantic number in the Universe interact with each other and create a thermal bath, a vast photon ocean, or more fundamentally a vast Super photon ocean. Through the analysing of the interactions between the Super photons and the normal photons, the foundation of the Super photon theory was developed quantitatively (Zhang, 2021a, 2021b). A normal photon particle is a dynamic packet of a number (N) of the Super photon particles in a local agglomeration. The interacting strength between a normal photon (having energy $= N\,E_s$) and a Super photon (having energy E_S) as an effective cross-section area $\sigma_p = N\sigma_S$ was introduced, where σ_s is the interacting strength thus effective cross-section area between two Super photons. The average numerical density of the Super photons (including the Super photons in the dynamic packets of the normal photons) in a unit of the free space was defined as ρ_n. During the time interval Δt, a normal photon sweeps through an effective volume of space as $\sigma_p\, c\, \Delta t = N\sigma_s\, c\, \Delta t$, where c is the speed of light in the free space. Therefore, the normal photon particle meets a number ($\rho_n N\sigma_S\, c\, \Delta t$) of the Super photons during the time interval Δt. The number of $\rho_n N\sigma_S\, c\, \Delta t$ Super photons interacts with the normal photon particle during the time interval Δt. Hence, the normal photon particle exchanging energy with the Super photon ocean during the time interval Δt (Zhang, 2021a) is

$$\Delta N = -\rho_n N\sigma_S\, c\, \Delta t \quad (3)$$

The Super photons are spread out in the observable Universe and they have a giant number. Hence, the average mass density of the Super photons (ρ_0) must be a constant on a cosmological scale. Two other Universal constants (R_0 and V_0) were proposed together with ρ_0 (Broberg, 1993; Zhang, 2021a), where R_0 is the ratio between the effective cross-section area and the inertial mass of a photon particle, V_0 is the volume of the free space, which is swept through by the effective cross-section area of a photon particle during one cycle. These constants are applicable to both the normal photons and the Super photons. Some defined or derived relations (Zhang, 2021a) useful for this article, are listed as follows:

$$\rho_0 = m_s\rho_n = \frac{h}{c\lambda_s}\rho_n \quad (4)$$

$$R_0 = \frac{\sigma_p}{m} = \frac{H}{\rho_0\, c} \quad (5)$$

$$V_0 = R_0\, m\, \lambda = \frac{h\, H}{\rho_0\, c^2} \quad (6)$$

where h is the Planck constant, H is the Hubble constant, c is the speed of the photons in the free space, λ_s and m_s are subsequently the wavelength and the inertial mass of the Super photon.

In this article, the correlation between the Universal Gravitational constant and the Hubble constant is deduced. A generalised law of Universal Gravitation is derived. The Virial relation within the Solar system, the Tully-Fisher law, and the Modified Newtonian Dynamics relation and acceleration in Galaxies are derived theoretically. The capability of a photon particle travelling at the constant speed of light in the free space with a friction force is theoretically verified. The temperature and the spectrum of the Cosmic Microwave Background Radiation (CMBR) are explained theoretically and determined accurately using the Super photon theory and the fluctuation-dissipation theorem. Further supporting evidences to the Super photon theory are provided. An experiment is proposed for the further proof of the Super photon theory.

The interactions between Super photon particles and concrete matter particles, the origin of the Universal Gravitation

Imagining a relatively stationary concrete matter particle (Zhang, 2021b) immersed in the ocean of Super photon particles as shown schematically in Figure 1, the matter particle with the inertial mass m_p and the equivalent effective interacting cross-section area $\sigma_p = 4\pi r_c^2$ would receive an inflow of the Super photon particles and neutrinos at light speed from its surrounding space. This article focuses on the Super photon particles (including the normal photon particles that are dynamic packets of the Super photon particles locally) because neutrinos are fermions that are supposed to make negligible contribution to the long-distance force of the Universal Gravitation.

A Super photon is a photon with the smallest unit of energy and mass, a photon is a dynamic packet of Super photons locally. All photons including the normal photons and the Super photons have wave and particle dualities. The average numerical density of the Super photon particles in a unit of the free space was defined as ρ_n

(Zhang, 2021a), assuming a percentage $\beta_1(-100\% \leq \beta_1 \leq 100\%)$ of the ρ_n Super photon particles from the free space flowing into the matter particle with the momentum of every Super photon particle as follows:

$$p_s = \frac{h}{\lambda_s} = \frac{E_s}{c} = m_s\, c \tag{7}$$

where p_s, λ_s, E_s, and m_s are subsequently the momentum, the wavelength, the energy, and the inertial mass of the Super photon particle.

It is interesting to point out that the Super photon particle has a momentum, so there must be pressure in the Super photon ocean. Gravitational waves may be viewed as periodic Super photon density and pressure oscillations propagating through the vast ocean of the Super photons with relatively long wavelengths. The number of Super photon particles flowing into the matter particle during the time Δt is

$$\Delta N = \beta_1 \rho_n \sigma_p c \Delta t \tag{8}$$

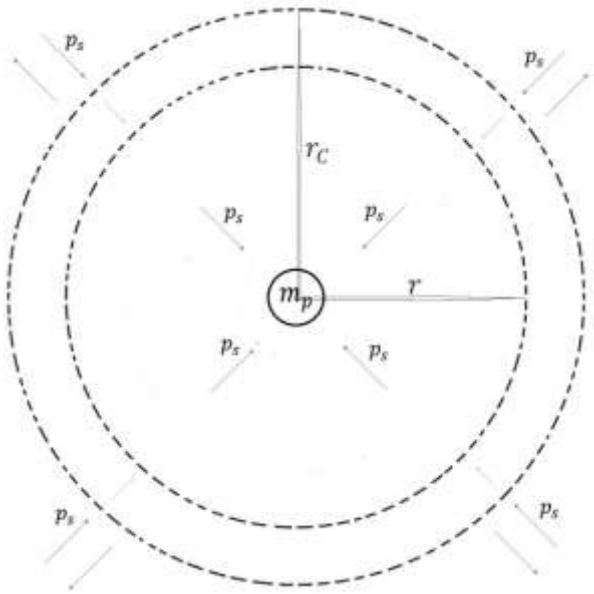

Fig. 1. The schematic diagram showing the inward flow of the Super photon particles with momentum p_s per Super photon towards a relatively stationary matter particle with the mass m_p.

If $\beta_1 = 1$, it means that the matter particle absorbs all the Super photons from its surrounding space. The 100% absorbing without emitting cannot last forever from a dynamic equilibrium point of view, eventually it will emit to achieve a dynamic equilibrium with its surrounding space. At this extreme, the matter particle behaves similar to some Black Hole but without the problem of singularity. Another extreme, if $\beta_1 = -1$, it means that the matter particle emits its mass and energy out, the mass and energy of the matter particle will eventually be spread out into the vast space of the Super photon ocean if keeping $\beta_1 = -1$ enough time. The restricted occasion of a net number of the Super photon particles flowing into the matter particle will be investigated first, which means $0 < \beta_1 \leq 1$. The corresponding mass and energy flowing into the matter particle are

$$\Delta m_p = \Delta N\, m_s = \beta_1 m_s \rho_n \sigma_p\, c\, \Delta t \tag{9}$$

$$\Delta E_p = \Delta N E_s = \beta_1 m_s \rho_n \sigma_p c^3\, \Delta t \tag{10}$$

where m_p and E_p are subsequently the mass and energy of the matter particle.

Inserting $\sigma_p = R_0 m_p$ and $\rho_0 = m_s \rho_n$ from equations (4) and (5) into equations (9) and (10) leads to

$$\Delta m_p = \frac{\Delta E_p}{c^2} = \beta_1 R_0 \rho_0 m_p\, c\, \Delta t \tag{11}$$

Because $H = A_0\, \rho_0\, c$ from equation (4), hence,

$$\Delta m_p = \frac{\Delta E_p}{c^2} = \beta_1 H m_p \Delta t \tag{12}$$

The mass and energy of the matter particle as the function of time can be derived through the integration of equations (11) and (12) as follows:

$$m_p(t) = m_p(0) e^{\beta_1 H t} \tag{13}$$

$$E_p(t) = E_p(0)\, e^{\beta_1 H t} \tag{14}$$

where $m_p(0)$ and $E_p(0)$ are the mass and energy of the matter particle at its state of the lowest mass and energy at $t = 0$.

Remembering H is approximately $2.29 \times 10^{-18}\ [\mathrm{s}^{-1}]$ (Zhang, 2021a) and $0 < \beta_1 \leq 1$. Therefore, during a relatively short period of time, for instance, days or years, the mass and energy increasing are extremely tiny. However, the tiny change of mass and energy accompanies an inward force, the force leads to contracting, vibrating and spinning of the matter particle around its equilibrium position because the interacting with photons with linear and circular polarizations. It may be explained further as following. It is verified that the effect of the two kinds of polarization of photons (linear and circular) at a certain range of frequencies on silica nano-particles is quite different (Ahn *et al.*, 2018). Linear polarization causes the silica particles to vibrate along the line of polarization while circular polarization causes the silica particles to spin. This may help to explain the

spinning and vibrating of the galaxies, the stars, the planets, and elementary particles. The contracting, vibrating, and spinning of the compositions of the matter particle induce internal friction forces, which cause the increase of the internal temperature and pressure. This increase of temperature and pressure inside the matter particle trigger off expanding and radiation, therefore, photons are released into surrounding space. Part of the energy and mass absorbed is emitted out. It can be predicted that the total energy radiated will be at the maximum while the radius of the matter particle is at its minimum and the total energy radiated will be at the minimum while its radius is at the maximum.

While the author searched literature for supporting evidence, it was found that the above prediction has been confirmed by the quantitative measurement of the relation between the total irradiance and the radius variations of the Sun (Pap *et al.*, 2001) and the amplitude of the fluctuation is approximately 0.015%. It shall be viewed as a supporting evidence of the dynamic circulation and equilibrium of the immersed matter particle with the thermal bath of the Super photon ocean. To maintain a relatively stable state of temperature and movement (including the spinning and the orbital velocity) the matter particle needs absorbing mass and energy through interacting with the thermal bath of the Super photon ocean at its surrounding, which means $0 < \beta_1 \leq 1$. The matter particle also emits photons because of compressing, frictions, and radiations. The mass and energy radiated can be slightly more or less than the mass and energy absorbed, which causes a mass and energy oscillation of the matter particle. A dynamic circulation and equilibrium state with fluctuation will be achieved. Flavour oscillation observed in neutrinos (Cai *et al.*, 2017) may be taken as an evidence of immersed matter particles that undergo two-way energy exchange with the thermal bath of the Super photon ocean having local fluctuations.

The secret of the dynamic circulation and equilibrium of mass and energy of the Universe is uncovered. Quantitative details of the mechanism need further research. For a normal photon, it releases a Super photon every cycle, its wavelength increases cycle by cycle slowly. It is the normal photons that are expanding, it is not the space itself. The matter particles absorb mass and energy through interacting with the thermal bath of the Super photon ocean to maintain their characterized temperatures and movements. And the matter particles release mass and energy by radiations, the released mass and energy mainly as photons, which eventually return the mass and energy to the free space by releasing Super photons every cycle while travelling at light speed to achieve mass and energy balance with the thermal bath of the vast Super photon ocean. The nuclear reactions and element generations inside the centre of galaxies and inside stars are probably merely by-processes because of the impinging of photons, neutrinos, and cosmic rays from all directions, and the high temperature and high pressure induced by impinging and frictions, which worth further research.

For a general illustration in a parable, all the galaxies, stars and planets are music instruments with different keys and strings, meanwhile, the Super photons, the normal photons, neutrinos and cosmic rays flowing towards the music instruments are the fingers of a glorious musician. All sorts of emitted matters, visible and invisible lights are like melodies spew out from the music instruments. It is interesting that the melodies can eventually turn back to the wonderful fingers of the glorious musician. Matter particles with different size and mass absorb and release different range of frequency and wavelength of photons to sustain their characterized movements and temperatures, and achieve dynamic equilibriums with their surrounding spaces such as the thermal bath of the vast Super photon ocean. Dynamic equilibriums are achieved, which is manifested by the relatively stationary spectrums of radiations from the galaxies, the stars, the planets, the fundamental particles and elements, with their characteristic range of temperatures, colours, brightness, and movements.

Although we are still lacking of technologies to detect a Super photon particle directly, we are capable to figure out the mass and energy balance of galaxies, stars, and planets. The Super photon particles are mainly either single Super photon particles or packets of Super photon particles as the normal photon particles in the free space. However, when they are approaching the mass centre of the galaxies, stars, and planets, a large percentage of them would pack together in superposition and change appearance to detectable normal photons and matter particles. For instance, we are able to prove the energy balance of the Earth through measuring and calculating the energy absorbed by the Earth and the energy emitted by the Earth. Certainly, through measuring and calculating the energy and mass flowing towards the Sun and the energy and mass the Sun radiated, we will be able to prove approximately the energy and mass balance of the Sun in average, although there are small fluctuations as observed on the total irradiance variations of the Sun (Pap *et al.*, 2001). Another exciting point is that Newton's law of gravitation in the Solar System, the Tully-Fisher law, and the Modified Newtonian Dynamics relation and acceleration in Galaxies can be derived from the Super photon theory quantitatively, which can help us to gain deeper insight into the origin of the Universal gravitation.

As shown schematically in Figure 1, we define r_c to represent the radius of the effective interacting cross-

section area ($\sigma_p = 4\pi r_c^2 = R_0 m_p$) of the matter particle with a mass m_p, hence,

$$r_c = \sqrt{\frac{R_0 m_p}{4\pi}} \tag{15}$$

Outside the ball of the effective radius r_c, there will be a random distribution of the Super photon particles. From equation (8) written above, the number of the Super photon particles flowing through the effective interacting cross-section area ($4\pi r_c^2$) towards the matter particle during the period Δt is

$$\Delta N = \beta_1 \rho_n \sigma_p \, c \, \Delta t = \beta_1 R_0 \rho_n m_p \, c \, \Delta t \tag{16}$$

Because the matter particle is in a dynamic equilibrium with its surrounding, around the effective interacting radius, the number of Super photon particles flowing towards the matter particle should be approximately 50% of the total number of Super photon particles to maintain a random distribution of the Super photon particles in average, hence, $\beta_1 \approx 0.5$ (fluctuating around 0.5 with an average at 0.5). At a distance $r \leq r_c$ from the matter centre, the fluid towards the matter particle must carry the same number of Super photon particles, but flow through a smaller area, if we define the local numerical density of Super photon particles as $\rho_n(r)$, i.e.

$$4\pi r^2 \rho_n(r) \, c = \beta_1 R_0 \rho_n m_p \, c \tag{17}$$

The local numerical density with a local gradient of the Super photon particles around the matter particle as a function of r is therefore,

$$\rho_n(r) = \frac{\beta_1 R_0 m_p \rho_n}{4\pi r^2} \tag{18}$$

Similar to equation (16) but applied at the radius r, the inward flowing rate of the Super photon particles is

$$\frac{dN}{dt} = \rho_n(r) \, \sigma_p \, c = R_0 \rho_n(r) m_p \, c \tag{19}$$

This represents a directed rate of momentum or a force transferred to the matter particle corresponding to

$$F = -\frac{dp}{dt} = -p_s \frac{dN}{dt} = -\frac{\beta_1 R_0^2 c^2 \rho_0}{4\pi} \frac{m_p^2}{r^2} \tag{20}$$

The force in equation (20) represents the Universal Gravitation force between the centre mass m_p and an equivalent effective mass ($-m_p$), which represents the average counter interactions from the rest of the Universe through the vast Super photon ocean to achieve an energy and force balance. The negative sign in front of m_p simply means when the centre m_p of the matter particle is absorbing the Super photons and contracting, the equivalent effective mass of the rest of the Universe ($-m_p$) is releasing the Super photons and expanding. While the centre m_p of the matter particle is releasing the Super photons and expanding, the equivalent effective mass ($-m_p$) is absorbing the Super photons and contracting. There is a mass and energy balance across the Universe. If locally two matter particles with different masses interact with each other, like the Sun and the Earth, a net gravitational attracting force is induced between them because they shield each other in the ocean of roaming Super photon particles. Hence, they tend to become closer to each other. If the Sun and the Earth are viewed together as a whole, the contracting and local increasing of the density of mass and energy happens, thus a counter force emerged to cancel out the attracting force. These reactions are for achieving a dynamic equilibrium of mass and energy and to maintain relatively stable distribution of mass and energy on a cosmological scale. Detailed analysis and calculation will be done in next section.

Now let us compare equation (20) with Newton's law of gravitation, they are the same if we assign that

$$G = \frac{\beta_1 R_0^2 c^2 \rho_0}{4\pi} \tag{21}$$

By using equation (5), we get

$$G = \frac{\beta_1 R_0 H \, c}{4\pi} = \frac{\beta_1 H^2}{4\pi \rho_0} \tag{22}$$

The Universal Gravitational Constant may be interpreted as the interacting and coupling constant of a matter particle with the rest of the Universe through its interacting with the vast ocean of Super photons. Physical science is mainly about the correlation of physical quantities. The correlation between the Universal Gravitational constant and the Hubble constant is disclosed quantitatively from equation (22). For fully understanding its implications, further research is worthwhile. By inserting $H \approx 2.29 \times 10^{-18} [\mathrm{s}^{-1}]$, $G \approx 6.6739 \times 10^{-11}$ [m^3/kg s^2] and $\beta_1 \approx 0.5$ into equation (22), the average mass density of Super photons on a cosmology scale as a Universal constant can be derived as follows:

$$\rho_0 \approx 3.13 \times 10^{-27} \, [\mathrm{kg/m}^3] \tag{23}$$

The value of the Universal constant R_0, the ratio between the effective cross-section area and the inertial mass of a photon particle (applicable to the Super photon as well) can be estimated as follows:

$$R_0 \approx 2.44 \, [\mathrm{m}^2/\mathrm{kg}] \tag{24}$$

Then we can derive that

$$G \approx 1.273 \times 10^{25} H^2 \quad (25)$$

The accuracy of the numbers in equations (23), (24), and (25) depends on the accuracy of the values of G and H. Having ρ_0 and R_0 at hand, we can do some interesting calculations. As an example, let us start from using equation (15)to calculate the effective radius of the Solar System and the Milky Way Galaxy based on their known total masses. In the Solar System, 99.86% of the system's known mass concentrates in the Sun (Woolfson, 2000), the total mass in the Solar System is approximately 1.99×10^{30}. Inserting this value and R_0 into equation (15), we get $r_C \approx 6.21 \times 10^{14}$ [m]. The border where the Solar System terminates is not precisely defined because its outer boundaries are shaped by two separate forces: the solar wind and the Sun's gravity. The limit of the solar wind's influence is roughly four times Pluto's distance from the Sun, the heliopause, the outer boundary of the heliosphere, is considered the beginning of the interstellar media, which is approximately 2×10^{13} [m]. The Sun's Hill sphere, the effective range of its gravitational dominance, is thought to extend up to a thousand times further, which approximately reaches 10^{16} [m] (Littmann, 2004). Our calculation of $r_C \approx 6.21 \times 10^{14}$ [m] sits approximately in the middle of these estimated radius based on the observations and calculations.

Regarding the Milky Way Galaxy, recent studies (Phelps *et al*., 2013; Kafle *et al*., 2014) indicate a range in mass, as large as 4.5×10^{12} $M_\odot$ and as small as $8 \times 10^{11} M_\odot$, where $M_\odot$ is the standard mass of the Sun. If we take both the values, which are approximately from 1.59 to 8.95×10^{42} [kg], and insert them into equation (15), we have $r_C$from 5.56×10^{20} to 1.31×10^{21} [m]. The Milky Way is the second-largest galaxy in the Local Group, with its stellar disk approximately 30 kpc in the diameter. If we believe that the ring-like filament of stars wrapping around the Milky Way belongs to the Milky Way itself, which are rippling above and below the relatively flat galactic plane, its stellar disk can reach a diameter of 46 to 55 kpc (Xu *et al*., 2015). The radius based on a diameter from 30 kpc to 55 kpc are between approximately 9.27×10^{20} and 1.70×10^{21} [m], which are in good agreement with our calculated values from equation (15), which is between 5.56×10^{20} and 1.31×10^{21} [m].

Vice versa, the total mass based on the observed effective radius may be estimated. For instance, if we use the observed approximately 9.27×10^{20} [m] and 1.7×10^{21} [m] as the effective radius, the estimated mass of the Milky Way from equation (15) would be between 2.22×10^{12} $M_\odot$and 7.48×10^{12} $M_\odot$. The dimensions and masses of other galaxies and stars may be estimated in the same way.

The gravitational force between two bodies, the generalised law of Universal Gravitation, the Tully-Fisher law and the Modified Newtonian Dynamics

The total momentum rate carried by the Super photon particles from background space to the body of a matter particle corresponds to a limited force from equations (4), (5), (8), and (16) as follows:

$$F_L(m_p) = -p_s \frac{dN}{dt} = -\frac{h}{\lambda_s} \beta_1 R_0 \rho_n m_p c = -cH\beta_1 m_p \quad (26)$$

Specifically, for the Sun (with $\beta_1 \approx 0.5$ at dynamic equilibrium state) there is:

$$F_L(M_{Sun}) = -cH\beta_1 M_{Sun} \approx -6.83 \times 10^{20} N \quad (27)$$

The value obtained with formula (27) can be compared with the following gravitational force on the Earth from the Sun according to Newton's Law:

$$F = -\frac{G\ M_{Sun} M_E}{r^2} \approx -3.54 \times 10^{22} N \quad (28)$$

This would imply that the Earth-Sun system receives a larger total momentum per second than the limited momentum flow rate towards the Sun from the Sun's back-ground space. How can this and the Newtonian gravitational force be explained? The solution is hidden in the difference between the flows of the Super photon particles absorbed by the matter particles in each of the two participating bodies and the number of interactions that takes place between the Super photons and the two participating bodies. Each matter particle absorbs the Super photon particles corresponding to the following rate of:

$$\frac{dN}{dt} = \beta_1 R_0 m_p c \rho_n = \frac{\beta_1 H m_p}{m_s} \quad (29)$$

where m_s is the mass of the Super photon particle, m_p is the mass of the matter particle.

Specifically, the m_p would be the mass of the Earth if we aim to calculate the gravitational force between the Earth and the Sun. Let us imagine a Super photon in the Sun-Earth two-body system while it interacts with the Earth. The Earth absorbs $\beta_1 H \frac{m_p}{m_s} \Delta t$ Super photon particles from its surrounding space during the time interval of Δt, meanwhile the Earth interacts with a total of $R_0 \rho_n(r) m_p\ c\ \Delta t$ Super photons directed towards the Sun. From equation (18), for the Sun-Earth system

$\rho_n(r) = \frac{\beta_1 R_0 M_{Sun}\, \rho_n}{4\pi r^2}$. There must be a small percentage β_2 $(0 < \beta_2 < 1)$ of the Super photon particles absorbed by the Earth but not of the Super photon particles flowing towards the Sun. Hence, the probability for absorption by the Earth is P_{abs} defined by

$$P_{abs} = \frac{\beta_1 H\, \Delta t m_p/m_s}{\beta_1\beta_2 H\, \Delta t\; m_p/m_s \;+\; R_0\rho_n(r) m_p\, c\, \Delta t} \tag{30}$$

The item containing the percentage β_2 in the denominator of equation (30) is for avoiding double counting. As a result, equation (30) can be simplified to:

$$P_{abs} = \frac{1}{\beta_2 + \frac{R_0\rho_{n(r)} c\, m_s}{H\beta_1}} = \frac{1}{\beta_2 + \frac{R_0 M_{Sun}}{4\pi r^2}} \tag{31}$$

The probability for interaction without absorption is $P_I = 1 - P_{abs}$. Inserting the numerical values of M_{Sun} (the mass of the Sun) and r (the distance between the Sun and the Earth), it can be calculated that $\frac{R_0 M_{Sun}}{4\pi r^2} \approx 1.7 \times 10^7$. As we know $0 < \beta_2 < 1$, the small percentage β_2 can be neglected in comparison with 1.7×10^7, for the Sun-Earth system, $P_{abs} \approx 1/(1.7 \times 10^7) \approx 5.9 \times 10^{-8}$ and $P_I \approx 1$. Therefore, as an average, the Super photon particles in the flow towards the Sun would interact with the Earth-Sun system approximately 1.7×10^7 times, and each interaction would supply the momentum of $p_s = m_s c$ to the Earth-Sun system directed towards the Sun from the Earth. It may be noted here that the wavelength of the Super photon is comparable with the one in the observable Universe. Therefore, the discussed interactions may take place simultaneously over long distances. Our Universe is entangled together with a gigantic number of the Super photons with super long wavelengths. For wider applications, M represents the centre mass inside the system, like the M_{Sun} for the Solar System. So, equation (31) can be generalised as follows:

$$P_{abs} = \frac{1}{\beta_2 + \frac{R_0 M}{4\pi r^2}} \tag{32}$$

In accordance with equations (22), (26), (29), and (31) written above, the total force acting in between the Earth and the Sun can be derived as follows:

$$F = -\frac{1}{P_{abs}}\, cH\beta_1 M_E \tag{33}$$

$$= -cH\beta_1\beta_2 M_E - \frac{G\, M_{Sun} M_E}{r^2} \approx -\frac{G\, M_{Sun} M_E}{r^2}$$

where M_E is the mass of the Earth. Therefore, for a two-body system interacting via the gravitation, the equation of Newton's law of gravitation is an ideal approximation while $cH\beta_1\beta_2 M_E \ll \frac{G\, M_{Sun} M_E}{r^2}$, which is the case in the Solar System. For wider applications, M represents the mass of the centre body, m represents the mass of the obiter, and r represents the distance between them. So, equation (33) becomes

$$F = -cH\beta_1\beta_2 m - \frac{GMm}{r^2} \tag{34}$$

Equation (34) may be called the generalised law of Universal Gravitation of a two-body system. The generalised acceleration a of the two-body system can be derived from equation (34) by dividing the mass of the obiter, i.e.

$$a = -cH\beta_1\beta_2 - \frac{GM}{r^2} = a_0 + a_N = \eta a_N \tag{35}$$

The Newtonian acceleration a_N is

$$a_N = -\frac{GM}{r^2} \tag{36}$$

The Universal acceleration $a_0$is

$$a_0 = -cH\beta_1\beta_2 \tag{37}$$

and

$$\eta = 1 + \frac{a_0}{a_N} = 1 + \frac{cH\beta_1\beta_2 r^2}{GM} \tag{38}$$

The minus sign in equations (33)-(37) simply means that the direction of the force is towards the centre. Because $0 \le \beta_1 \le 1$ and $0 < \beta_2 < 1$, from equation (37), the absolute value of the Universal acceleration $|a_0| < c\,H \approx 6.86 \times 10^{-10}$ [m/s^2]. Inserting $\beta_1 \approx 0.5$, and $\beta_2 \approx 0.167$ (approximately $\frac{1}{6}$ of the Super photons absorbed by the orbiter is not from the Super photons flowing towards the centre of the system, which is a reasonable assumption, considering one of six faces in a cubic), the calculated $|a_0|$ is approximately 0.57×10^{-10} [m/s^2]. For stars rotating with the velocity v around its rotational axis located in the galaxy centre, the centripetal acceleration $(-\frac{v^2}{r})$ must be equal to the acceleration from equation (35), hence,

$$v^2 = cH\beta_1\beta_2 r + \frac{GM}{r} = -a_0 r + \frac{GM}{r} \tag{39}$$

Therefore,

$$v^4 = a_0^2 r^2 - 2GMa_0 + (\frac{GM}{r})^2 \tag{40}$$

If $\frac{G\,M}{r} \gg |a_0 r|$, which is the case of the Solar System, it can be derived from equation (39) that $v^2 \approx \frac{G\,M}{r}$ (the Virial relation, which has been proved in the Solar system), then we are in the Newtonian regime. For galaxies with much larger and distributed masses, when r becomes distant enough, $(\frac{GM}{r})^2$ becomes negligible, a regime is entered with approximately constant density of the Super photons, $\frac{\rho_n(r)}{\rho_n} = \frac{G\,M}{c\,H\,r^2} \approx \beta_1$, which leads to:

$$r^2 \approx \frac{G\,M}{c\,H\,\beta_1} \tag{41}$$

Combining equations (37), (40), and (41), we have

$$v^4 \approx a_0^2 r^2 - 2GMa_0 = GM|a_0|(2+\beta_2) \tag{42}$$

$$= GMa_M$$

Equation (42) reveals the Tully-Fisher law (Binney *et al.*, 2008) and the modified Newtonian dynamics (MoND) proposed in 1983 (Milgrom, 1983a, 1983b). a_M is the acceleration of the MoND, $a_M \approx 1.24 \times 10^{-10}\ [\mathrm{m/s^2}]$ according to Milgrom if taking the Hubble constant as approximately 70.8 $[\mathrm{km\ s^{-1}Mpc^{-1}}]$, which is in good agreement with the theoretical calculation from the Super photon theory with equations (37) and (42).

Astronomical observations show that for disk galaxies, the fourth power of the orbital speed (v_f^4) of stars moving around the core of the galaxy at the flat end of the rotation curve is proportional to the total luminosity $L_u$of the galaxy. Since $L_u$is proportional to the observable inertial mass M of the galaxy, it is obtained that $v_f^4 \propto M$. This is well-known as the Tully-Fisher law, which is a widely applicable relation and it is originated from the empirical fitting of astronomical observations and calculations. This type of rotation curve differs drastically from that of the planets rotating around the Sun, whose orbital speed, according to the Newtonian mechanics and the General Relativity in the weak field and small velocity approximations, is $v^2 \cong \frac{G\,M}{r}$ (the Virial relation). The physical basis of the Tully-Fisher law is the relation between a galaxy's total observable inertial mass M and the velocity at the flat end of the rotation curve v_f.

In 1983, Milgrom interpreted the Tully-Fisher law as an indication of a deviation from the Newtonian gravitation, claiming the MoND (Milgrom, 1983a, 1983b; Binney *et al*., 2008). Milgrom hypothesized that this relation should hold exactly, thus interpreting it as an inductive law of nature instead of an empirical relation. According to Milgrom, the deeper significance of this relation between this special galactic acceleration and the Hubble constant should be revealed by future cosmological insights. Now the Super photon theory has revealed the cosmological insights into the physical origin of both the MoND and the Tully-Fisher relations, which have been sought after for over thirty years as stated by McGaugh (2011) and (Hass, EPJ de. 2018. The 'constant Lagrangian' fit of galaxy rotation curves as caused by cosmic space expansion under energy conservation conditions. Pre-print. https://vixra.org/pdf/1805.0342v1.pdf). Taking into account the distribution of the observable inertial masses, the rotation curve of Galaxies will be able to be fully determined accurately without the assumption of dark matter. If the universe is neither expanding continuously nor expanding in accelerating, the adoption of the assumption of dark energy becomes unnecessary as well.

Further supporting evidences of the Super photon theory, the origin of the CMBR and the theoretic determination of the temperature and the spectrum of the CMBR

There may be a doubt that how a photon particle can travel at a constant speed c inside the free space with a viscous friction force. The explanation is that the photon particle behaves like a tiny spin rocket that releases an extremely tiny fragment of mass and energy every cycle to combat the viscous friction force and maintain the constant speed of propagation. Let us do a simple calculation, first assuming that v is the speed of the photon particle with an inertial mass of m travelling through the free space with a viscous friction force F_{vis}. According to equations (1) and (2), for keeping a constant speed of v, the average energy dissipation $< E_{DIS} >$ of the photon particle within one second of time to combat the friction force must be equal to

$$< E_{DIS} > = \frac{1}{2}\,|F_{vis} \cdot v| = \frac{1}{2} R_m v^2 = \frac{R_m}{2m} m v^2 \tag{43}$$

$$= Hmv^2$$

Within the short period of one second, the frequency of the photon (f) can be viewed as a constant value. Hence, the photon totally spins as many as f-cycles within the period of one second. According to the Super photon theory, the photon releases a Super photon every cycle with the energy of hH. Employing the Planck-Einstein equation $hf = mc^2$, it can be derived that the energy releasing of the photon particle within the period of one second of time must be

$$< E_{DIS} > = Hhf = Hmc^2 \tag{44}$$

The energy releasing of the photon particle within the period of one second must be the average energy dissipation $< E_{DIS} >$ of the photon within one second, hence equalling equations (43) and (44), we can derive

$v = \pm c$: the photon particle in the free space can indeed propagate at a constant speed c. From an electromagnetic point of view, the speed of photons in the free space is a constant $\sqrt{\frac{1}{\varepsilon_0 \mu_0}}$ because ε_0 is the electric constant of the free space, and μ_0 is the magnetic constant of the free space. These two constants imply that there is substance inside the free space. The speed of light is determined by the intrinsic properties of the substance inside the free space. Interestingly, Maxwell derived the expressions for the dielectric constant and the magnetic permeability of the free space in terms of transverse elasticity and density of a subtle substance inside the free space, i.e. the aether (Maxwell, 1865; Rubik and Jabs, 2018). It is not well-known that Einstein called for a relativistic aether in his 1920 speech given at the University of Leiden (Rubik and Jabs, 2018), namely he proclaimed in German that "According to the General Theory of Relativity, space without aether is unthinkable."

Now it is theoretically derived that the subtle substance in the free space is an interactive thermal bath of the vast Super photon ocean spreading all over the observable Universe. The subtle substance in the vast space of a vacuum such as the interactive thermal bath of the vast Super photon ocean is worth for further research. As far as we already know, the subtle substance inside the vast Super photon ocean has an elastic modulus, a stress tensor, a shear tensor, a dielectric constant, a magnetic permeability coefficient, a gravitic constant, a cogravitic (torsionic) constant, a gravitoelectric constant, a cogravitoelectric (torsionoelectric) constant, a gravitomagnetic constant, a cogravitomagnetic (torsionomagnetic) constant (Zakharenko, 2020), a magnetic susceptibility and a characteristic electromagnetic wave impedance of 376.73 Ohms.

From an electromagnetic perspective, electromagnetic waves propagate through a medium containing the substance with an impedance must experience energy dissipation. From a mechanical perspective, for the photon particles roaming at light speed together with cosmic rays and neutrinos through the interactive thermal bath of the vast Super photon ocean there must be frictions and, as a result, energy dissipations. Therefore, there must be energy fluctuations according to the Fluctuation-dissipation theorem (Kubo, 1966; Kardar and Golestanian, 1999). While cosmic rays, neutrinos, and high-energy photons are travelling through the thermal bath of the vast Super photon ocean locally, the weak interactions will lead to a linear increase of the energy of the thermal bath of the vast Super photon ocean locally above its dynamic equilibrium of energy level transiently. Consequently, a tendency of relaxing to its original energy level builds up. While the process of relaxing to the dynamic equilibrium of energy level happens, the CMBR is emitted (Zhang, 2021b). The energy fluctuations of the thermal bath of the vast Super photon ocean caused by cosmic rays, neutrinos, and high-energy photons locally travelling through must be the origin of the spectrum of the CMBR. Hence, the origin of the CMBR must be local and nonredshifted, thus it can preserve its black-body radiation spectrum.

There is an excellent large-scale homogeneity because of the dynamic equilibrium between the immersed travelling particles and the vast thermal bath of the giant Super photon ocean across the observable Universe. A piece of supporting evidence is as follows: the Pierre Auger Collaboration discovered that the anisotropy signal of cosmic rays appears to be consistent with the sources of cosmic rays in a cosmic-ray frame coincident with the reference frame of the CMBR (Aab *et al*., 2017). The author believes that the CMBR is the manifestation of the energy fluctuations of the thermal bath of the vast Super photon ocean, the weak afterglow of the free space where cosmic rays, neutrinos, and high-energy photons are locally travelling through. The weak anisotropy of the CMBR must be linked with the anisotropy local distribution of cosmic rays, neutrinos, and high-energy photons, which must be a promising direction for further research to validate.

Now let us determine the temperature and the spectrum of the CMBR theoretically. The amplitude of the energy fluctuation $(\Delta E_V / E_V)$ of a unit volume of the free space can be estimated based on information from (Assis and Neves, 1995; Pap *et al*., 2001; Bradt, 2008; Huang *et al*., 2012; Leff, 2015; Cai *et al*., 2017; Hill *et al*., 2018; Batista *et al*., 2019), which must be approximately 0.015%. The average mass density of Super photons in the free space is known from equation (23) as $\rho_0 \approx 3.13 \times 10^{-27}$ [kg/m^3]. Employing the Stephan-Boltzmann law for the cavity black-body radiation (Bradt, 2008) and the Mass-Energy equation, it infers that

$$\frac{4\sigma}{c} T^4 \approx \frac{\Delta E_V}{E_V} \rho_0 c^2 \tag{45}$$

where σ is the Stephan-Boltzmann constant, c is the speed of light in the free space.

Substituting all these values into equation (45), the temperature of the CMBR can be determined as $T \approx 2.73$ [K] theoretically, which is a nice match to the measured value by COBE's instruments (Bradt, 2008). The theoretic modelling of the fluctuation-dissipation theorem may be traced back to the Rayleigh-Jeans law, Wien radiation formula, and Planck radiation formula for the interpretation of the blackbody radiation spectrum (Boya, 2003). The thermal bath of the vast Super photon ocean is a perfect cavity blackbody because it fulfils two conditions: (*) The bath is in a thermodynamic

equilibrium at a relatively stable temperature, (**) The external perturbation from the week interactions between the thermal bath of the vast Super photon ocean and the cosmic rays, neutrinos, and high-energy photons travelling through locally is in the linear response regime because the viscosity coefficient of the free space is extremely low. Hence, it can be asserted from the fluctuation-dissipation theorem that the spectrum of the CMBR obeys the Planck radiation formula and have an excellent match with the radiation spectrum of an ideal blackbody at the CMBR temperature of approximately 2.73 [K]. The normal photons of starlight can be treated approximately as an ideal gas, the amplitude of the energy fluctuation of the free space because of the normal photons can be theoretically calculated (Leff, 2015) as follows:

$$\frac{\Delta E_V}{E_V} \approx \frac{\delta N}{N} \approx \sqrt{\frac{1.369}{2.029 \times 10^7 T^3}} \approx 0.00557\% \tag{46}$$

According to the work by Assis and Neves (1995), the energy density of the flux of cosmic rays is comparable with the energy density of the starlight (the normal photons). So, the amplitude of the fluctuation of the free space must be doubled to 0.011% approximately by including the influence of the cosmic rays. If adding further the estimated small amount of energy fluctuation caused by high energy neutrinos (Cai *et al.*, 2017; Batista *et al.*, 2019), the total amplitude of the fluctuation of the free space must be approximately 0.015%. The fluctuation-dissipation theorem is a powerful tool in interrelating the interactions between the thermal bath of the vast Super photon ocean and the immersed travellers such as cosmic rays, neutrinos, fundamental particles, elements, molecules, planets, stars, and galaxies.

An experiment is proposed which may distinguish the Super photon theory from the theories of expanding Universe and Big-Bang cosmology. First, suppose that we have a well-shielded vacuum chamber, inner surface coated with graphite, with two well-aligned and transparent windows at two opposite sides, locating in a laboratory at a constant low temperature. If we shine different electromagnetic waves through the chamber with well-controlled vacuum environment and measure the temperature fluctuations, and associate secondary radiations inside the chamber, what can we expect to get? If we shine intense X-rays or γ-rays through it, there will be a detectable temperature fluctuation and associate secondary radiations, according to the Super photon theory because the energy dissipation must be able to reach a measurable level. If we shine intense radio waves with wavelength of tens of centimetres through it, there must have no detectable temperature change because the energy dissipation is at a negligible low level. However, according to the theories based on massless photons travelling through frictionless vacuum with no energy dissipation, like the theory of General Relativity, Expanding Universe, and Big-Bang cosmology, there will be no measurable difference no matter what kind of photons shinning though it. The author is confident that the proposed experiment will be able to demonstrate clearly the limitations of General Relativity, Expanding Universe, and Big-Bang cosmology that are based on massless photons travelling through frictionless vacuum with no energy dissipation.

Concerning many assumptions dependent on the cosmological models, such assumptions employed during the analyses of astronomical observational data create confusions. For instance, the cosmology models based on the General Relativity take into account the effect of time dilation (Melia and Maier, 2013). However, the time dilation effect is not generally applicable, no time dilation effect was observed in the light curves of quasars and in duration measures of gamma-ray bursts (Hawkins, 2010; Kocevski and Petrosian, 2013; Littlejohns and Butler, 2014). The time dilation effect of Supernova Ia light curves can be explained as clock retardation because of the local increase of viscosity, or being the signature of some special evolutionary process (Drell *et al.*, 2000), or cosmology-dependent assumptions made during the analyses of the light curves (Crawford, 2017). Big-Bang cosmological model claims that the CMBR is composed by photons that is a remnant from an early stage of the Universe, known as relic radiation dating back to the epoch of recombination (photon decoupling) with a redshift value of approximately 1100. It is a questionable hypothesis that those photons can travel in space containing a variety of matter particles for such a long time through such a long distance without being absorbed and without being scattered.

It is well-known that matter particles of a variety of size and temperature spread all over the Universe from the very distant past, up to current; they absorb and scatter photons, and re-emit photons in a spectrum of their own characters. Hence, photons must have mean and maximum free travel path lengths, also mean and maximum free travel times. The free path length and the free travel time of a certain spectrum of photons must fall in a statistic distribution around a mean value. This is the reason why the most distant astronomical object observed in the Universe such as the galaxy GN-z11 has a redshift value of just below 11.1, which is the largest confirmed observable redshift value of any astronomical object (Oesch *et al.*, 2016). There is the redshift value of no larger than 12 that was reported for any observable astronomical object. The Universe becomes opaque to observers beyond a distance with a maximum value of redshift below 12. If the photons that existed at the time of photon decoupling and afterwards have been propagating unimpeded ever since and stretched by the

space expanding as assumed in the Big-Bang model, we must be able to observe a range of redshift values much higher than 12 but less than 1100. It is a seriously flawed argument to disprove the Tired-Light models based on the wrong assumption of an infinitely large redshift value for a nonexpanding Universe. The nonexpanding Universe Tired-Light model making a superior fit on observational data of eight cosmology tests was reported by LaViolette (2021).

CONCLUSION

The Super photon is treated as a fundamental unit of mass and energy in dynamic circulation. Through the analysing of the interactions among the Super photons, normal photons, immersed concrete matter particles, and the thermal bath of the vast Super photon ocean, the Super photon theory is developed quantitatively. Gravitational waves are proposed as periodic density and pressure oscillations of the Super photon particles propagating through the vast Super photon ocean. The equation of a mass and its effective interacting radius is derived from the Super photon theory and it is employed to calculate the effective radius of the Solar System and the Milky Way Galaxy based on their known masses, or vice visa. The calculated results are in good agreement with the estimated values based on the astronomical observations and calculations. The Universal Gravitational Constant is derived from the Super photon theory and it is interpreted as the interacting and coupling constant of an immersed matter particle with the rest of the Universe through the thermal bath of the vast Super photon ocean. The correlation between the Universal Gravitational constant and the Hubble constant is deduced theoretically.

The mysteries behind the dynamic circulation and equilibrium of energy and mass of the Universe are discussed, supporting evidences, demonstrating signs and validation methods are presented. Flavour oscillation observed in neutrinos is taken as an evidence of immersed matter particles that undergo two-way energy exchange with the thermal bath of the Super photon ocean with local fluctuations. Immersed matter particles can absorb the roaming Super photons, normal photons, neutrinos, and cosmic rays thus mass and energy from the thermal bath of the vast Super photon ocean because they locate at places with low potential energies. They convert the absorbed energy to kinetic energy and higher-grade thermal energy through internal interactions to sustain their characteristic movements and temperatures. Immersed matter particles emit mass and energy to their surrounding spaces to achieve dynamic circulation and equilibrium. Immersed matter particles with different size and mass absorb and emit photons of different ranges of frequencies, demonstrating relatively stable characteristic masses, temperatures, colours, brightness, and movements, which manifests the state of dynamic equilibrium achieved.

The generalised law of Universal Gravitation is derived while applying the Super photon theory to the two-body system interacting via gravity. Thereafter, the Virial relation within the Solar System, the Tully-Fisher law, and the Modified Newtonian Dynamics relation and acceleration within galaxies are derived theoretically. The cosmological insights into the origins of both the Modified Newtonian Dynamics and the Tully-Fisher laws, which have been sought after for over thirty years, are revealed quantitatively. The temperature and the spectrum of the CMBR are explained theoretically and determined accurately using the Super photon theory together with the fluctuation-dissipation theorem. The capability of a photon particle with an inertial mass travelling at a constant speed c inside the free space with a viscous friction force is theoretically verified. The speed of light is determined by the intrinsic properties of the substance inside the free space. An experiment is proposed, which may further distinguish the Super photon theory from the theories of Expanding Universe and Big-Bang cosmology in a simple way. Time dilation effect is not generally applicable, it may be alternatively explained as clock retardation because of the local increase of viscosity.

The Super photon theory is still in its stage of infancy. However, the author believes that the theory has a huge potential to be further developed to explain phenomena that have plagued the physical world for many years. Wider research directions and frontiers may be further developed. For instance, it is necessary to better understand the interacting and recirculating of photons, neutrinos, cosmic rays, and all sorts of immersed matter particles in the thermal bath of the vast Super photon ocean quantitatively. It may help in the understanding of the mechanisms of the production and the stability of fundamental particles and elements, predicting the relative abundance of the elements in the Universe. Further development of the Super photon theory together with the fluctuation-dissipation theorem may help to develop a unified theory of physics, which would be applicable in both the microcosm and the macrocosm.

ACKNOWLEDGEMENT

The author gratefully acknowledges the encouragements and supports from my family, friends, and colleagues to these theoretical investigations.

REFERENCES

Aab, A., Abreu, P., Aglietta, M., Al Samarai, I., Albuquerque, IFM., Allekotte, I., Almela, A., Alvarez Castillo, J., Alvarez-Muñiz, J., Anastasi, GA., Anchordoqui, L., Andrada B. *et al*. 2017. Observation of a large-scale anisotropy in the arrival directions of cosmic rays above 8×1018 eV. Science. 357(6357):1266-1270. DOI: https://doi.org/10.1126/science.aan4338.

Ahn, J., Xu, ZJ., Bang, J., Deng, YH, Hoang, TM., Han, QK., Ma, RM. and Li, TC. 2018. Optically levitated nanodumbbell torsion balance and GHz nanomechanical rotor. Physical Review Letters. 121(3):033603. DOI: https://doi.org/10.1103/PhysRevLett.121.033603.

Assis, AKT. 1992. On Hubble's law of redshift, Olbers' paradox and the cosmic background radiation. Apeiron. 12:10-16.

Assis, AKT. and Neves, MCD. 1995. History of the 2.7 K temperature prior to Penzias and Wilson. Apeiron. 2:79-84.

Batista, RA., de Almeida, RM., Lago, B. and Kotera, K. 2019. Cosmogenic photon and neutrino fluxes in the Auger era. Journal of Cosmology and Astroparticle Physics. 2019:JCAP01(2019)002. DOI: https://doi.org/10.1088/1475-7516/2019/01/002.

Binney, J. and Tremaine, S. 2008. Galactic Dynamics. (2nd edi.). Princeton University Press, Princeton, USA. pp 733.

Boya, L. 2003. The thermal radiation formula of Planck (1900). Rev. Real Academia de Ciencias. Zaragoza (Spain). 58:91-114. Pre-print arxiv.org/pdf/physics/0402064.pdf.

Bradt, H. 2008. Astrophysics Processes: The Physics of Astronomical Phenomena. Cambridge University Press, Cambridge, UK. pp 534.

Broberg, H. 1993. Quantized vacuum energy and the hierarchy of matter. In: Progress in New Cosmologies: Beyond the Big-Bang. Arp, HC., Keys, CR. and Rudnicki, K. (eds.). Springer, Boston, MA, USA. pp 333-351. DOI: https://doi.org/10.1007/978-1-4899-1225-1_22.

Crawford, DF. 2017. A problem with the analysis of type Ia supernovae. Open Astronomy. 26(1):111-119. DOI: https://doi.org/10.1515/astro-2017-0013.

Cai, Y., García, JH., Schmidt, MA., Vicente, A. and Volkas, RR. 2017. From the trees to the forest: A review of radiative neutrino mass models. Frontiers in Physics. 5:1-56. DOI: https://doi.org/10.3389/fphy.2017.00063.

Drell, PS., Loredo, TJ. and Wasserman, I. 2000. Type Ia supernovae, evolution, and the cosmological constant. The Astrophysical Journal. 530(2):593-617. DOI: https://doi.org/10.1086/308393.

Hawkins, MRS. 2010. On time dilation in quasar light curves. Monthly Notices of the Royal Astronomical Society. 405(3):1940-1946. DOI: https://doi.org/10.1111/j.1365-2966.2010.16581.x.

Hill, R., Masui, KW. and Scott, D. 2018. The spectrum of the Universe. Applied Spectroscopy. 72(5):663-688.

Huang, X., Loeb, NG. and Chuang, H. 2012. Assessing stability of CERES-FM3 daytime long wave unfiltered radiance with AIRS radiances. Journal of Atmosphere and Oceanic Technology. 29(3):375-381. DOI: https://doi.org/10.1175/JTECH-D-11-00066.1.

Hubble, EP. 1937. The Observational Approach to Cosmology. Oxford University Press, Oxford at the Clarendon Press, UK.

Kafle, PR., Sharma, S., Lewis, GF. and Bland-Hawthorn, J. 2014. On the shoulders of giants: Properties of the stellar halo and the Milky Way mass distribution. The Astrophysical Journal. 794(1):59-75. DOI: https://doi.org/10.1088/0004-637X/794/1/59.

Kardar, M. and Golestanian, R. 1999. The friction of vacuum and other fluctuation induced forces. Reviews of Modern Physics. 71:1233-1247. DOI: https://doi.org/10.1103/RevModPhys.71.1233.

Kocevski, D. and Petrosian, V. 2013. On the lack of time dilation signatures in gamma-ray burst light curves. The Astrophysical Journal. 765(2):116-23. DOI: https://doi.org/10.1088/0004-637X/765/2/116.

Kubo, R. 1966. The fluctuation-dissipation theorem. Reports on Progress in Physics. 29(1):255-284. DOI: https://doi.org/10.1088/0034-4885/29/1/306.

LaViolette, PA. 2021. Expanding or static Universe: Emergence of a new paradigm. International Journal of Astronomy and Astrophysics. 11(2):190-231. DOI: https://doi.org/10.4236/ijaa.2021.112011.

Leff, HS. 2015. Fluctuations in particle number for a photon gas. American Journal of Physics. 83(4):362-365. DOI: https://doi.org/10.1119/1.4904322.

Littlejohns, OM. and Butler, NR. 2014. Investigating signatures of cosmological time dilation in duration measures of prompt gamma ray burst light curves. Monthly Notices of the Royal Astronomical Society. 444(4):3948-3960. DOI: https://doi.org/10.1093/mnras/stu1767.

Littmann, M. 2004. Planets Beyond: Discovering the Outer Solar System. Courier Dover Publications. 162-163.

Manjavacas, A. and Garcíade Abajo, FJ. 2010. Thermal and vacuum friction acting on rotating particles. Physical Review A. 82(6):063827.

Maxwell, JC. 1865. A dynamical theory of the electromagnetic field. Philosophical Transactions of the Royal Society of London. 155:459-512.

McGaugh, SS. 2011. Novel test of modified Newtonian dynamics with gas rich galaxies. Physical Review Letters. 106(12):121303. DOI: https://doi.org/10.1103/PhysRevLett.106.121303.

Melia, F. and Maier, RS. 2013. Cosmic chronometers in the $R_h = ct$ Universe. Monthly Notices of the Royal Astronomical Society. 432(4):2669-2675. DOI: https://doi.org/10.1093/mnras/stt596.

Milgrom, M. 1983[a]. A modification of the Newtonian dynamics as a possible alternative to the hidden mass hypothesis. The Astrophysical Journal. 270:365-370. DOI: https://doi.org/10.1086/161130.

Milgrom, M. 1983[b]. A modification of the Newtonian dynamics – Implications for galaxies. The Astrophysical Journal. 270:371-383.DOI:https://doi.org/10.1086/161131.

Oesch, PA., Brammer, G., van Dokkum, PG., Illingworth, GD., Bouwens, RJ., Labbe, I., Franx, M., Momcheva, I., Ashby, MLN., Fazio, GG., Gonzalez, V., Holden, B., Magee, D., Skelton, RE., Smit, R., Spitler, LR., Trenti, M. and Willner, SP. 2016. A remarkably luminous galaxy at z = 11.1 measured with Hubble Space Telescope grism spectroscopy. The Astrophysical Journal. 819(2):129-139. DOI: https://doi.org/10.3847/0004-637X/819/2/129.

Pap, J., Rozelot, JP., Godier, S. and Varadi, F. 2001. On the relation between total irradiance and radius variations. Astronomy and Astrophysics. 372(3):1005-1018. DOI: https://doi.org/10.1051/0004-6361:20010280.

Phelps, S., Nusser, A. and Desjacques, V. 2013. The mass of the Milky Way and M31 using the method of least action. The Astrophysical Journal. 775(2):102-13. DOI: https://doi.org/10.1088/0004-637X/775/2/102.

Pound, RV. and Rebka, GA. (Jr.) 1960. Apparent weight of photons. Physical Review Letters. 4(7):337-341. DOI: https://doi.org/10.1103/PhysRevLett.4.337.

Rubik, B. and Jabs, H. 2018. Revisiting the aether in science. Cosmos and History. The Journal of Natural and Social Philosophy. 14(2):239-255.

Woolfson, M. 2000. The origin and evolution of the solar system. Astronomy and Geophysics. 41(1):1.12-1.19. DOI: https://doi.org/10.1046/j.1468-4004.2000.00012.x.

Xu, Y., Newberg, HJ., Carlin, JL., Liu, C., Deng, L., Li, J., Schönrich, R. and Yanny, B. 2015. Rings and radial waves in the disk of the Milky Way. The Astrophysical Journal. 801(2):105-129. DOI: https://doi.org/10.1088/0004-637X/801/2/105.

Zakharenko, AA. 2020. Relative material parameters αE, αH, ϑG, ϑF, ξE, ξF, βH, βG, ζE, ζG, λH, and λF for magnetoelectroelastics incorporating gravitational phenomena. Hadronic Journal. 43(2):171-186. DOI: https://doi.org/10.5281/zenodo.3987732.

Zhang, WD. 2021[a]. The Foundation of an Emerged Superphoton Theory. Canadian Journal of Pure and Applied Sciences. 15(2):5221-5229.

Zhang, WD. 2021[b]. The Bose-Einstein Condensation and the Dynamic Circulation of Photons.Canadian Journal of Pure and Applied Sciences. 15(2):5247-5252.

Received: Final Revised: June 30, 2021;
Accepted: August 27, 2021

Canadian Journal of Pure and Applied Sciences
Vol. 15, No. 3, pp. 5297-5305, Oct 2021
Online ISSN: 1920-3853; Print ISSN: 1715-9997
Available online at www.cjpas.net

Canadian Journal of pure&applied sciences

LOGIC GATE ARITHMETIC AND QUATERNIONS

Christopher C. O'Neill
Cataphysics Group, Recess, Old Connaught Ave. Shankill, Co. Dublin, Ireland

ABSTRACT

A new method for Logic Gate Arithmetic is proposed allowing sets to be added, subtracted, multiplied, and divided in an novel way leading to an alternate and expanded appreciation of the Set Theory. An additional eleven Logic Operators are derived from the known operators: AND, OR, NOR, XOR, and XNOR, and their relationships described. Utilizing the principles of Dimensional Gate Operators (DGO), the new operators are shown to be directly related to dimensionality, both higher and lower, and the relationship to the Quaternions is given preliminary treatment.

Keywords: Logic Gate Arithmetic, set theory, dimensional gate operators, boolean algebra, quaternions.

INTRODUCTION, BACKGROUND, AND TERMINOLOGY

Logic Operators are an important part of modern Computer Systems and Set Theory. There are six primary Logic Gate Operators; AND, OR, NOR, XOR, XNOR, and NOT, as they are traditionally perceived. More accurately, it can be said that there are only 3 (AND, OR, and XOR) with the NOT operator being more of a decorator acting on these to create the other 2 (anti-operators) for a total of 5.

O'Neill (2021) explored the possibility that these Logic Operators were incomplete and added 11 more, for a total of 16. Approximately seven months after writing this, the author became aware of a video by N.J. Wildberger called "Implication and 16 logical operations" and realized that Wildberger had arrived at the same conception in 2018 (https://www.youtube.com/watch?v=XkqmuUg_yFs). Wildberger claims to have derived his new set of logic operations in a formal algebraic sense using the Boolean Algebra (Boole, 1847) and proceeds to name a selection of them in relation to the Stoic Logic of Modus Ponens and others in relation to their own internal properties.

For instance, the Logic or Truth table that corresponds to the binary number '0000' (read right to left), he denotes as '0' or 'zero'. It's counterpart '1111' is therefore '1'. 'IMP' stands for implication and OT1 stands for 'Original Term'.

Once a naming convention is in place, it matters little how it got there. However, these new logic operators lack Boolean Algebra symbols, like '^', 'V', 'Δ', and '!Δ' (Bocheński, 1948; Roegel, 2002). To counteract this, a new naming convention will be outlined in this theoretical work. The author developed this method, before realizing that Wildberger had already given names to all the logic operations.

0	NOR	$NIMP_1$	NOT_2	$NIMP_2$	NOT_1	XOR	NAND
0000	0001	0010	0011	0100	0101	0110	0111

AND	XNOR	OT_1	IMP1	OT_2	IMP_1	OR	1
1000	1001	1010	1011	1100	1101	1110	1111

Fig. 1. Wildberger's 16 Logic Operations, which are almost identical to the Logical Connective operators which have been in use and development for over a hundred years.

In any case, such naming conventions are not too concerning, especially in early stage research such as this. After all, the XOR and XNOR logic gates are sometimes called EOR and ENOR, without much complication, and there are numerous variations used for symbols throughout the literature, including '!' and '¬' for NOT, etc. (Roegel, 2002).

More confusingly, however, is applying the binary numbers to the Truth Tables. Binary numbers are usually written horizontally, whereas Truth Tables are nearly always vertical (see in Appendix 1). When compiling Wildberger's operations into the tables shown in Figure 1, it seemed necessary to list the operators, as though their binary numbers are being read from 'right to left'. To avoid headaches, it will be necessary to continue with this convention. In this paper, all 16 Logic Operators will be derived from the original six.

Corresponding author e-mail: chris.ozneill@gmail.com

Wildberger does not reveal how it was that he developed his version of the 16 Logic Operators. But given their similarities to the Logical Connectives (Bocheński, 1948), as well as Wildberger's extensive knowledge on the subject, it would appear likely he was aware of them in advance. Even so, the author is not aware if this would be classed as an act of plagiarism, given that the information in the form of an online video presentation, as opposed to a scientific paper.

More on logic

The binary numbers '0000' to '1111' can be used to represent all 16 of the Dimensional Gate Operators (DGO). However, some of these operations don't appear all that logical. To alleviate this concern, the author decided to attempt to derive the other eleven operators from the original five.

?	NOR	?	?	?	?	XOR	NAND
0000	0001	0010	0011	0100	0101	0110	0111

AND	XNOR	?	?	?	?	OR	?
1000	1001	1010	1011	1100	1101	1110	1111

Fig. 2. The other two tables: "A rose by any other name?"

The first step is to combine the known logic gates; AND, OR, XOR, NAND, XNOR, and NOR to see if they can generate any knew terms. XOR can be obtained via the OR operator acting on AND and OR:

$$((\wedge) \vee (\vee)) = \Delta$$

However, this is obvious and doesn't lead us out of the recursive loop and into the unknown parts of the DGO. Similarly, $((\wedge) \wedge (\vee)) = \wedge$. It is easy to see how this method will lead us in circles.

Taking a step back and reexamining the Truth Tables for these operations, there are clearly two more 'binary' numbers present in each of the tables. Which are: '1010' and '1100'. These numbers are equivalent to Wildberger's OT1 and OT2. In terms of Binary Connectives, these are known as Proposition P and Q. However, this author identified them as RIGHT (or 'R') and LEFT (L), as in Right and Left Multiplication. Applying the NOR operator, !R (NOT RIGHT) and !L (NOT LEFT) are easily obtained. From here, we can get to a new Logic Operator; '0100', which is made from the combination of Δ and !L:

$$((\Delta) \wedge (!L)) = 0100$$

It was called 0100 or '^U' (meaning AND UP), because it is similar to '^' (1000) shifted 'up' one space. The NOT version of this gate is 1011 giving us; '!^U' (NOT AND UP). Similarly, !V shifted down one space gives us 0010, so this is '!VD' (NOR DOWN).

Therefore, '!VD' is equal to 1101. Once again, the Unary Connectives denotes 0010 and 0100, as the NIMP1 and NIMP2, which is identical to Wildberger's notation and more indication that his work is at least derivative. Together with the NOT versions of these two new Logic Operations, we are able to fill 14 of the 16 arrangements in the tables shown in Figure 3.

N	!V	!VD	!R	^U	!L	Δ	!^
0000	0001	0010	0011	0100	0101	0110	0111

^	!Δ	L	!^U	R	VD	V	!N
1000	1001	1010	1011	1100	1101	1110	1111

Fig. 3. All 16 operations with their names and symbols.

In the process, '0000' and '1111' were named: i.e. "N" and "!N" respectively (standing for "NONE" and "NOT NONE"). These can equally be written as "NOT ALL" (NA) and "ALL" (A). Both 'None' and 'A' are already symbols in the Boolean Algebra, so "NONE" (N) and "NOT NONE" (!N) are used instead. Getting to 'N' and '!N' from any of these gates is a simple matter. We only need apply one gate together with its NOT version:

$$((\vee) \Delta (!\vee)) = N$$

The reverse is given by:

$$((!\vee) \Delta (!\vee)) = !N$$

Now all 16 Dimensional Gate Operators and their Boolean Algebra symbols are in place, their relationships can be further explored and they can be written in terms of one another. For example, all these statements are TRUE:

$$((R) \Delta (L)) = \Delta((!N) !\Delta (L)) = !L(!VD) !\Delta (L) = !\wedge$$
$$((\Delta) \wedge (!L)) = \wedge U$$

This means that the last equation in this list can equally be written as follows:

$$((R) \Delta (L)) (!(!VD) !\Delta !(L)) ((!N) !\Delta (L)) = \wedge U$$

To make these relations more easily digestible, the author took the liberty to organize all this information in the following tables shown in Figures 4 to 19 below (the Python code to generate these tables is in Appendix 2).

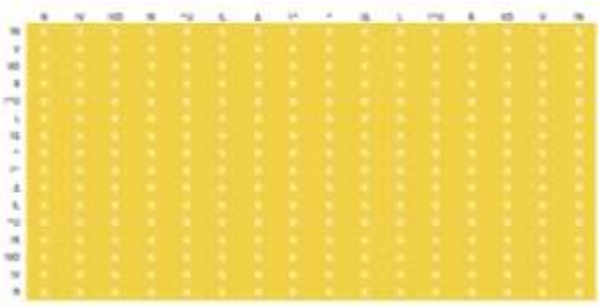

Fig. 4. N : [0000].

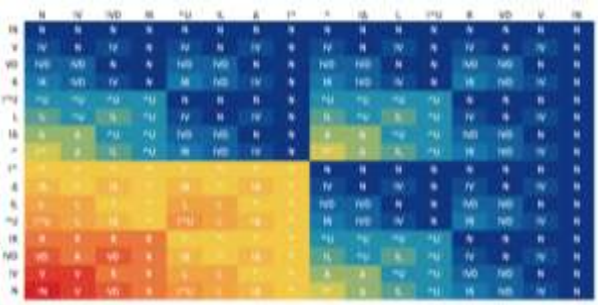

Fig. 5. !V : [0001].

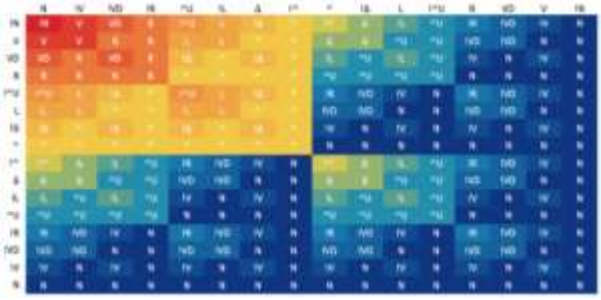

Fig. 6. !VD : [0010].

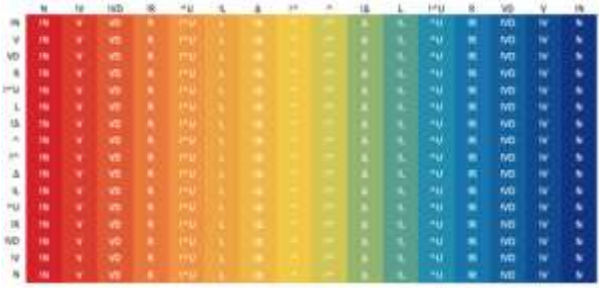

Fig. 7. !R : [0011].

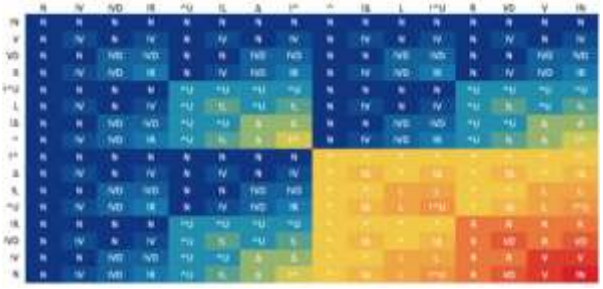

Fig. 8. ^U : [0100].

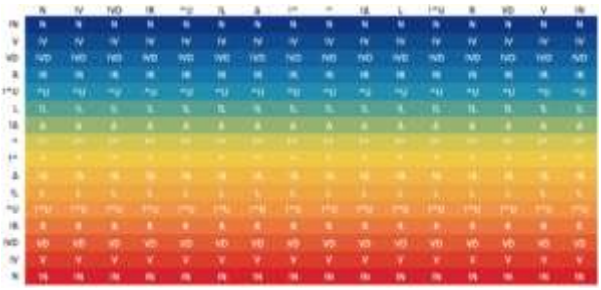

Fig. 9. !L : [0101].

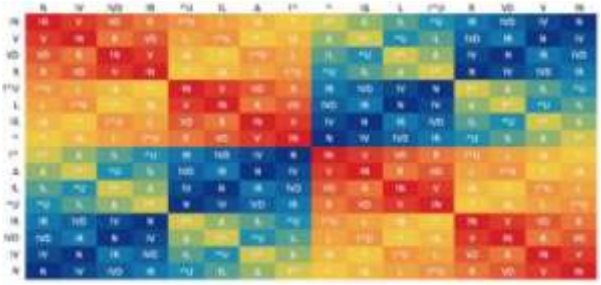

Fig. 10. Δ : [0110].

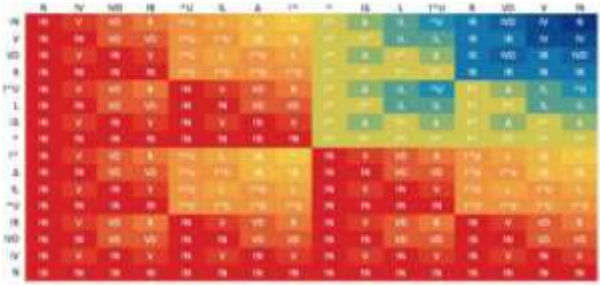

Fig. 11. !^ : [0111].

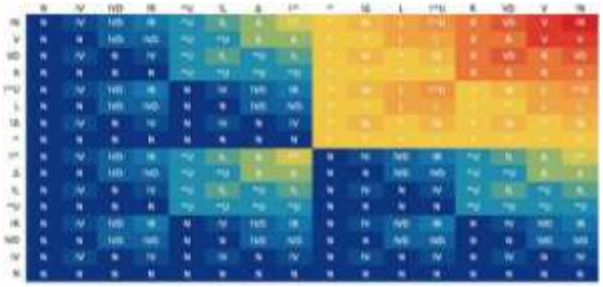

Fig. 12. ^ : [1000].

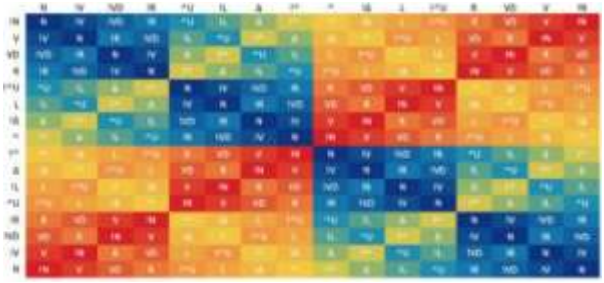

Fig. 13. !Δ : [1001].

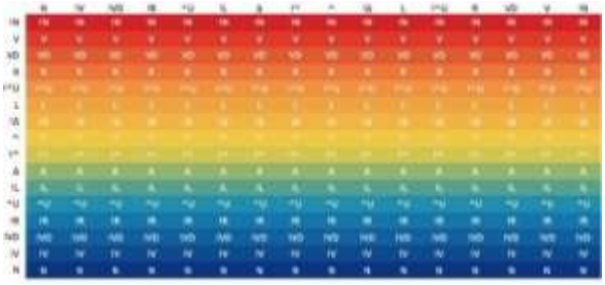

Fig. 14. L : [1010].

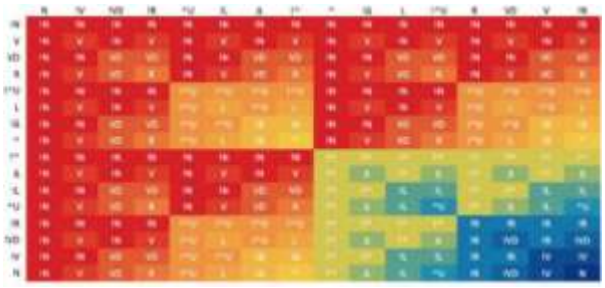

Fig. 15. !^U : [1011].

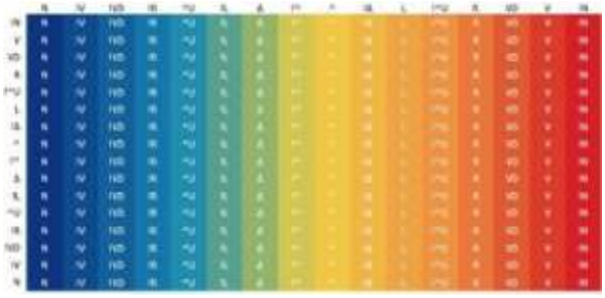

Fig. 16. R : [1100].

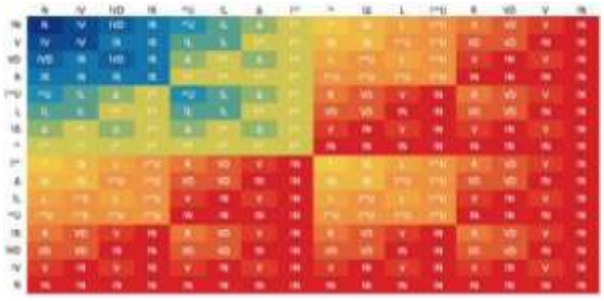

Fig. 17. VD : [1101].

Fig. 18. V : [1110].

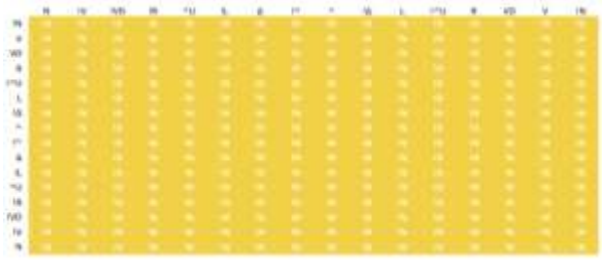

Fig. 19. !N :[1111].

The basic rules of arithmetic; like addition, subtraction and/or multiplication and division can easily be applied to these gates. For instance, R Δ L can be rewritten to produce (!^)) as follows:

$$R \Delta L = \Delta$$
$$(R) \Delta (\Delta) = ((VD) \Delta (!^))$$
$$(R) \Delta (\Delta) / ((VD) \Delta) = (!^)$$

Another more convoluted example, this time rewriting ((Δ) ^ (!L)) for (VD) is:

$$(\Delta) \wedge (!L) = \wedge U$$
$$((\Delta) \wedge (\wedge U)) \vee ((\Delta) \vee (\wedge U)) = \wedge U$$
$$!(((\Delta) \wedge (\wedge U)) \vee ((\Delta) \vee (\wedge U))) = !\wedge U$$
$$(!\Delta)\wedge(!\wedge U) \vee (!\Delta)\vee(!\wedge U)/(!\Delta) \wedge = VD$$

Later, these methods will be applied to the Set Theory, as a whole.

Some notable gates

In the previous research paper, operators like Δ (XOR) and !Δ (XNOR) were both encountered (O'Neill, 2021). Each of these represents the rules of Real Number Arithmetic and Complex Arithmetic, according to the DGO. This shift in how to do arithmetic transports us from the ostensibly 1-2 dimensional lines of the Real Numbers and into the 2-3 dimensional realm of the 'Complex Plane'.

Unlike the numbers of the Complex Plane, however, there are no algebraic numbers here. This is because (–1)1/2 (the imaginary unit, i) is equal to ±1 in !Δ. Therefore, they are simply the ordinary numbers with a different arithmetic rule set. The reader might be tempted to think that Δ also governs the rules of the Quaternions and Octonions (Hamilton, 2000). However, this is not the case.

One important feature of the Quaternions is that they are non-commutative; that is A(B) =/= B(A). This attribute is seen in the DGO in places like !VD, !R, !^U, and VD, where A(-B) =/= B(-A). Quaternions are governed by a mix of !VD and ^U logic, because they are non-commutative for different signed quaternions, whilst retaining the !Δ rule set of the imaginary numbers, when the signed values for i, j, k are the same:

$$i2 = j2 = k2 = -1$$
$$ij = k, ji = -k$$
$$jk = i, kj = -i$$
$$ki = j, ik = -j$$

The Quaternions are made from two groups of !VD and one of ^U. This asymmetry allows for the loop to be closed and further explains why these higher-dimensional algebras can only be order 2^n. Below there are three tables

that correspond to the following (left to right): Δ, ^U, and !VD.

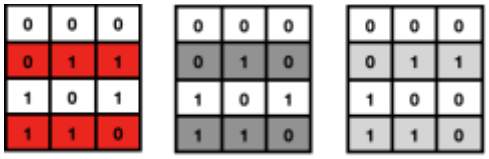

Dimensional spaces

Returning to Figures 4 to 19 (i.e. sets 0 to 15), it is apparent all of them can fit together like jigsaw pieces. For instance, it is clear that Figures 5, 6, 8, and 12 (i.e. sets 1, 2, 4, and 8) form a set that can be called 'Set B'. Similarly, we can make 'Set C' from Figures 11, 15, 17, and 18 (i.e. sets 7, 11, 13, and 14). The horizontal and vertical lines appear to make another set, 'Set D' (Figures 7, 9, 14, and 16). That just leaves the final four graphs: Figures 4, 10, 13, and 19, namely set {0, 6, 9, 15} or 'Set A'. All the sets are shown schematically in Figure 20. There is a distinct pattern emerging in how these sets are dispersed across the entire binary number line, here represented in their decimal form.

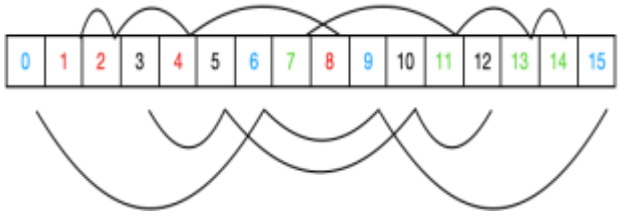

Fig. 20. All four sets: A (blue numbers), B (red), C (green), and D (black). This pattern explains the frequency of the NOT values, as they are represented in the DGO.

The first composite graph (Figure 21) shows the domains of N (in the bottom left-hand corner), Δ immediately above that, !Δ in the lower righthand corner, and !N in the top right. What matters here is not the order, so much, as the grouping and what it reveals about the connectivity of the Logical Connective space. Set A can be rewritten as {N, Δ, !Δ, !N}, which stands for the paths between Dimensions 0, 2, 3, and 1, respectively. To understand this, look at our Quaternion logic gates: ^U and !VD. Figure 22 shows Set B.

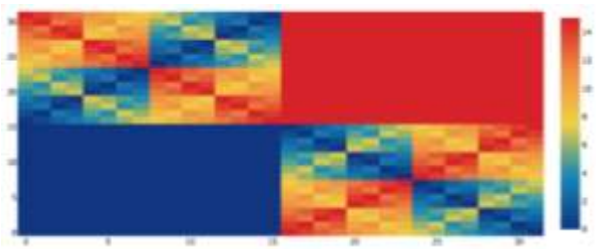

Fig. 21. Set A = {0, 6, 9, 15} or A = {N, Δ, !Δ, !N}.

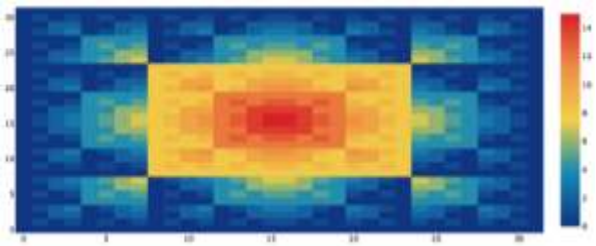

Fig. 22. Set B = {1, 2, 4, 8} or B = {!^, !^U, !VD, !V}.

If we multiply these terms by ¬Δ (the Imaginary rule set) we obtain (!VD) ¬Δ (!^U) = Δ (our Real number logic). This shows the path by which Quaternions collapse down into the rule set of both the Imaginary and Real numbered spaces of dimensions 2-3. We can then continue this process, in the usual manner, multiplying (Δ) !Δ (!Δ) and (Δ) Δ (!Δ) to obtain the dimensions beneath them as follows:

(Δ) !Δ (!Δ) = N
(Δ) Δ (!Δ) = !N

One possible conclusion is that N and !N refer to dimensions 0 and 1, respectively. In this sense, the Real Numbers and Imaginary Numbers live in Set A, along with dimensions 1 and 0. Whereas the Quaternions live jointly in Sets B and C, along with some other more traditional logic gates. The Octonions, Sedenions, and (potentially) other higher dimensional spaces exist scattered among the other sets, although this is something that must be investigated further.

While this way of thinking about logic gates can provide a method for travelling from one rule set (i.e. dimensional space) to the other, it should not be taken too literally. In one sense, applying the Δ or !Δ rule set to the Quaternions does not lead to Δ or !Δ but rather to hybrid spaces; the Real Quaternions and the Imaginary Quaternions, and neither of these two systems cancel out to Dimension 0 when summed in Δ. More on this in up-coming research.

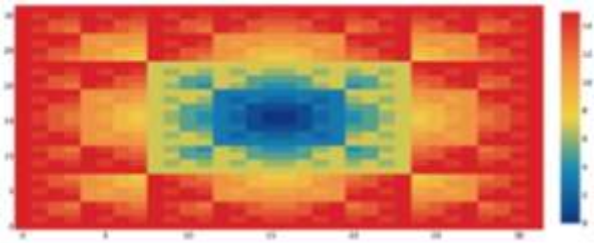

Fig. 23. Set C = {7, 11, 13, 14} or C = {V, VD, ^U, ^}.

Based on the arrangements of the graphs in Figure 21, it is possible to see the placement beginning in the lower left-hand corner and proceeding in a zigzag fashion to the upper-right. The graphs in Figure 22 go in the reverse direction and the pattern is repeated in the next two graphs in Figures 23 and 24.

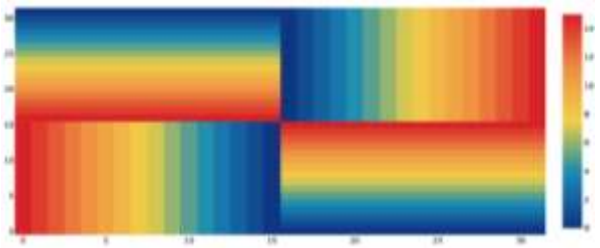

Fig. 24. Set D = {3, 5, 10, 12} or D = {!R, !L, L, R}.

Using the pattern of Figure 21 as the 'base arrangement', Figures 21, 22, 23, and 24 can be arranged into a single graph (Figs. 25, 26, and 27). But note there are 16! possible arrangements, so care must be taken when choosing an arrangement.

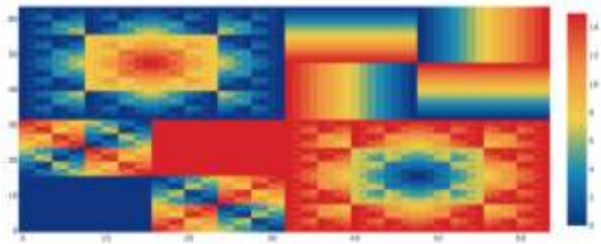

Fig. 25. The preliminary grouping of the sets.

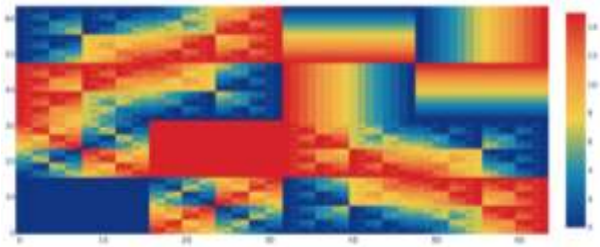

Fig. 26. The final grouping.

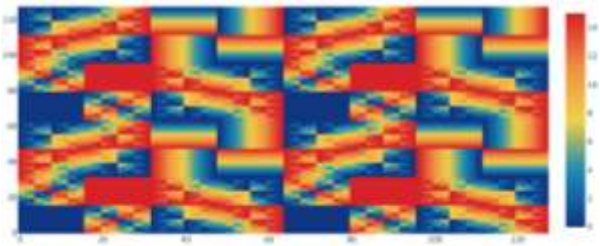

Fig. 27. A more tiled version of Figure 26.

It can be deduced from the lack of connectivity between the different regions that a more accurate arrangement is possible. We shouldn't expect to see such harsh delineating lines from the interrelated sets. Earlier it was stated that the Quaternions and the Imaginary Quaternions follow the rules laid out in Set B, while the Real Quaternions are sitting in Set C, which obviously cannot be right. If the Real Quaternions are moved into Set B with the other Quaternions, this forces all the commonly known logic gates: ^, !^, V, and !V together, which is a much neater result.

Moreover, there is a much greater connectivity between the different regions. Given that this has served as a useful vehicle to explain some of the relationships between the Reals, Imaginary, Quaternions, and Logic Gates, it may be worthwhile exploring this line of inquiry further.

Set Theory Arithmetic

It is possible (at least in principle) to divide and multiply set operators together. And it is also possible to apply these kinds of operations to the actual sets of Set Theory. Unlike traditional methods of arithmetic with sets, where (for instance) the elements of one set are divided into another, here the operators acting on the sets will be divided.

Using the DGO methods on Set Theory will advance new ways to get from one partition of a group of sets to another and will lead to operations, which were not previously possible under the former laws of the Boolean Algebra.

To begin with, it is not clear why this should this be so. After all, the current operators already cover all aspects and combinations of Set Theory. But when it is recalled that the !VD operator governs the arithmetic of the quaternions, this portends the possibility of doing Set Theory in higher order dimensions.

Quaternions are known to be indispensable for describing some aspects of Quantum Mechanics, and these extra Logic Gates simply extend the number of dimensions available to work with. This also forms the basis of the Dimensional Gate Operator Standard Model, which is further developed in (C. O'Neill, "Dimensional Gate Quaternion Multiplication, Quarks & Polyhedra" DOI: 10.13140/RG.2.2.22968.57601/1; "Construction of the 2nd and 3rd Generation Quark Particles in the Standard Model" DOI: 10.13140/RG.2.2.20228.35202, as well as the overview: "Making Sense of the Standard Model" DOI: 10.13140/RG.2.2.34132.12163/1). Essentially, these operators can be used to describe sets of these particles via the rules of the 4-dimensional space (4D space) in which they live. Alternatively, 4D Set Theory might find application in the perplexing world of Quantum Computing, where a bit can be a '1' and '0' at the same time.

To begin with, a simple example with sets A and B is as follows:

$$(A \Delta B) \wedge (A \,!L\, B) = (A \,\wedge U\, B)$$

This operation would correspond with the following Venn Diagrams:

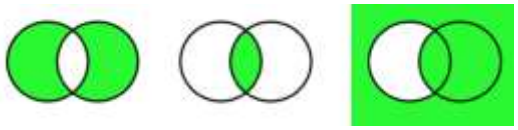

and equals to:

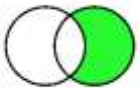

A slightly more complex operation would be the following:

$$(A \; R \; B) \; \Delta \; (A \; !\Delta \; B) \; / \; (!VD)!\Delta = (A \; !V \; B)$$

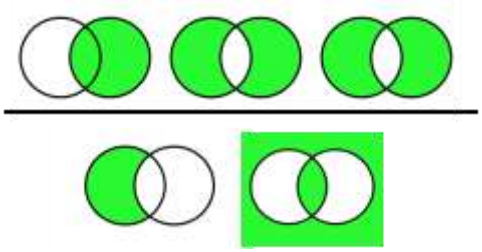

This equals to

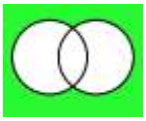

An important aspect of the above two equations is they both feature noncommutative logic gates, specifically: !L, R, and !VD. This means that different outcomes for the equation would be expected depending on which set we choose to be on the right and which appears on the left.

Since sets have no orientation in space and since either one can be on the 'left' or on the 'right', this poses something of a problem, especially as the set arithmetic moves into higher dimensions. Or at least it would be a problem, if it were expected to form a closed space algebra, but as we shall see in the follow-up preprints and research papers, creating closed field algebras might not always be the best approach.

CONCLUSION

The Dimensional Logic Gate Operators have the potential for some very unusual and unexpected applications. They can find application in computer circuitry, set theory, and Boolean algebra, as well as Quantum Computing, 4-dimensional (and higher) Set Theory, and Set Theory Arithmetic.

REFERENCES

Bocheński, JM. 1948. Précis de logique mathématique. F.G. Kroonder, Bussum, North Holland.

Boole, G. 1847. The Mathematical Analysis of Logic, Being an Essay Towards a Calculus of Deductive Reasoning. Cambridge: MacMillan, Barclay, and MacMillan; London: George Bell, UK. pp 82.

Hamilton, WR. 2000. On Quaternions, or on a new system of imaginaries in algebra. The London, Edinburgh and Dublin Philosophical Magazine and Journal of Science. XXV-XXXVI (3rd Series). pp 92. (Hamilton, WR. 1847. XXXVI. On Quaternions, or on a new system of imaginaries in algebra. Proceedings of the Royal Irish Academy. Philosophical Magazine Series 3. 31(207):214) DOI: https://doi.org/10.1080/14786444708645826.

O'Neill, CC. 2021. Reimagining complex numbers. Canadian Journal of Pure and Applied Sciences. 15(2):5261-5268. DOI: https://doi.org/10.13140/RG.2.2.26666.44480/1.

Roegel, D. 2002. A brief survey of 20th century logical notations. [Research Report] LORIA – Université de Lorraine, France. ffhal-02340520 (HAL Id: hal-02340520) https://hal.inria.fr/hal-02340520.

Received: June 28, 2021; Revised: August 18, 2021;
Accepted: Sept 30, 2021

Appendix 1.

The 16 tables.

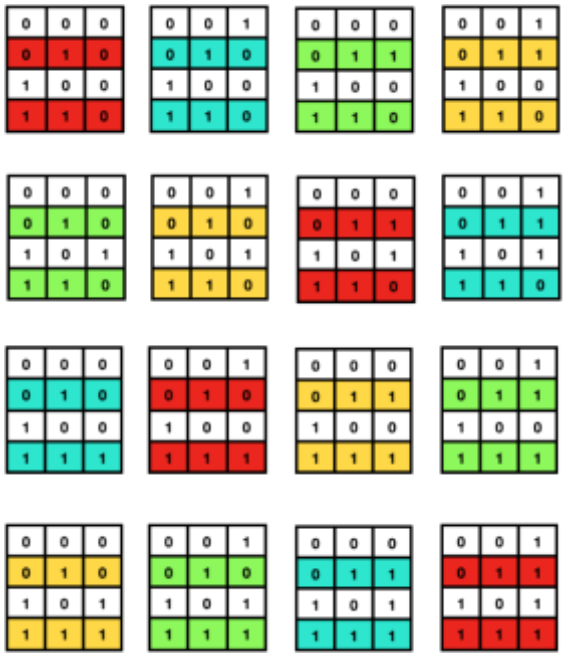

Fig. A1.1. From top left: N, !V, !VD, !R, ^U, !L, Δ, !^, ^, !Δ, L, !^U, R, VD, V, !N. The colour-coding here pertains to the different sets: A = Red, B = Green, C = Blue, and D = Yellow. The Quaternions are created from !VD and ^U and the Real Quaternions are created from !^U and VD.

Appendix 2.
The Python codes for the generation of Figures 4 to 19.

```
import plotly
import  plotly.graph_objs as go
import plotly.figure_factory as ff
import numpy as np
import copy

gates = {'0000':'N', '0001':'!V', '0010':'!VD', '0011':'!R',
'0100':'^U', '0101':'!L',
'0110':'Δ', '0111':'!^', '1000':'^', '1001':'!Δ', '1010':'L',
'1011':'!^U',
'1100':'R', '1101':'VD', '1110':'V', '1111':'!N'}

logic = []
for i in range(16):
    t = str(bin(i)[2:])
    c = len(t)
    j = 4
    while j<= 4:
        g = 4 - c
        k = t.rjust(j, '0')
        logic.append(k)
        j += 1

test1 = []
for i in logic:
    gg = []
    f = list(i)
    gg.append(f)
    test1.append(f)

colourscales = ['Greys', 'YlGnBu', 'Greens', 'YlOrRd',
'Bluered', 'RdBu','Reds', 'Blues', 'Picnic', 'Rainbow',
'Portland', 'Jet','Hot', 'Blackbody', 'Earth', 'Electric',
'Viridis', 'Cividis']

lg = ['N', '!V', '!VD', '!R', '^U', '!L', 'Δ', '!^', '^', '!Δ', 'L',
'!^U', 'R', 'VD', 'V', '!N']

check = []
balance = []

for f in logic:

    m = list(f)

    blogic = []
    for i in logic:
        for c in logic:
            u = 0
            r = copy.copy(i)
            r0 = list(r)
            while u <= 3:
                if i[u] == '1' and c[u] == '1':
                    r0[u] = m[0]
                elif i[u] == '0' and c[u] == '1':
                    r0[u] = m[1]
                if i[u] == '1' and c[u] == '0':
                    r0[u] = m[2]
                elif i[u] == '0' and c[u] == '0':
                    r0[u] = m[3]
                u+=1
            r = ''.join(r0)
            blogic.append(r)

    state = []
    for i in blogic:
        state.append(gates[i])

    states= np.array(state).reshape(16, 16)


    po4=[]
    for i in blogic:
        kk = int(i, 2)
        po4.append(kk)

    po3 = np.array(po4).reshape(16, 16)

    po5 = states.tolist()
    check.append(po5)
```

```
    po6 = po3.tolist()
    balance.append(po6)

    fig = ff.create_annotated_heatmap(z = po3, x=lg, y=lg,
annotation_text=states,colorscale=colourscales[10])
    fig.update_layout(title_text=gates[f] + " " + ":" + " " +
"[" + f + "]", title_x=0.5,
                titlefont= {"size": 14},
                  font={'color':'black'},
                  paper_bgcolor= 'white',
                  plot_bgcolor= "white",
                  hovermode='closest',)
    fig.show()
```

Canadian Journal of Pure and Applied Sciences
Vol. 15, No. 3, pp. 5307-5316, Oct 2021
Online ISSN: 1920-3853; Print ISSN: 1715-9997
Available online at www.cjpas.net

Canadian Journal of pure & applied sciences

EXACT CRITICAL VALUES OF THE WILCOXON RANK SUM TEST

*Friday Ewere and Sunday Martins Ogbonmwan
Department of Statistics, Faculty of Physical Sciences, University of Benin, Benin City, Edo State, Nigeria

ABSTRACT

Generating the entire permutation sample space especially when sample sizes are not small have been a major problem in constructing an exact test of significance of a rank statistic. Recently, the use of softwares for computing statistical tests has become common. However, procedures on this software for calculating the significance levels for many nonparametric tests are based on asymptotic results. These asymptotic results are only reliable when sample sizes are large enough. Unfortunately, the definition of what constitute a large sample size for most statistics is quite vague. The aim of this paper is to formulate a method for obtaining the exact distribution of a rank statistic. The proposed method is based on combinatorics in the representation of the probability generating function of the test statistic. The proposed method bypasses the problem of actually carrying out a complete enumeration in a permutation test. Essentially, the exact critical values for the Wilcoxon Rank Sum (WRS) test statistic are produced. The asymptotic property of the WRS is carefully studied and the minimum sample size required for the application of the large sample approximation is provided.

Keywords: Wilcoxon Rank Sum Test, exact test, rank test, permutation test, combinatorics.

INTRODUCTION

The risk in decision making cannot be totally eliminated but it can be controlled if correct statistical procedures are employed. The unconditional permutation approach is a statistical procedure that ensures that the probability of a type I error is exactly α, thus ensuring that the resulting distribution of the test statistic is exact, see Agresti (1992), Good (2000), Pesarin (2001), Odiase and Ogbonmwan (2005) and Ogbonmwan *et al*. (2007). The unconditional exact permutation approach where row and column totals are allowed to vary with each permutation is very much unlike the conditional exact permutation approach of fixing the row and column totals (Headrick, 2003; Bagui and Bagui, 2004; Odiase and Ogbonmwan, 2005). Exact tests constructed by restricting attention to a conditional reference set of contingency tables with margins fixed at the values actually observed is not always true in nature. The unconditional permutation approach is computationally very demanding and more complex than the conditional approach (Agresti, 1992; Good, 2000; Opdyke, 2003). Earlier study Agresti (1992) observed that the results obtained from the conditional and unconditional permutation approaches can be quite discrepant.

Another study Scheffe (1943) showed that the permutation approach is the only possible technique of constructing exact tests of significance for a general class of problems. Hoeffding (1952) remarked that this permutation test is asymptotically as powerful as the best parametric test. There are several Monte Carlo methods that can be used in generating exact p-values. The most widely used is the bootstrap re-sampling technique developed by Efron (1979).

The Bayesian and the Likelihood approaches can be found in Bayarri and Berger (2004), Spiegelhalter (2004). All these alternative approaches to the unconditional permutation approach only give approximate results. Exact procedures are the best and should always be applied whenever it is practically possible, Lehmann (1986) and Good (2000). Permutation tests provide exact results especially when complete enumeration is possible, Pesarin (2001). A big challenge in using nonparametric test is the availability of computational formulas and tables of exact critical values. This continues to be a problem as revealed by a survey of 20 in-print general college statistics texts, Fahoome (2002). Many nonparametric tests have large sample approximations that can be used as an alternative to tabulated exact critical values. These approximations are useful substitutes if the sample size is sufficiently large and hence obviate the need for locating tables of exact critical values. However, there is no generally agreed upon definition of what constitutes a large sample size for most statistics (Bergmann *et al*., 2000; Fahoome, 2002). A complete enumeration of the permutation sample space for the purpose of constructing an exact test of significance is only possible when sample sizes are small

*Corresponding author e-mail: friday.ewere@uniben.edu

(Odiase and Ogbonmwan, 2005; Ewere and Ogbonmwan, 2020). The consideration given in this article produces the exact distribution of the Wilcoxon Rank Sum test statistic (WRS) by precisely tracking the number of permutations without carrying out a complete enumeration. Thus, providing the possibility of finding the exact distribution of the WRS for larger sample sizes. When sample sizes are large, the exact distribution of the WRS can be approximated by the normal approximation. We study the convergence of the normal approximation to the exact distribution of the WRS and provide the minimum sample size required for the application of the asymptotic distribution. Computations are done using the computer algebra Mathematica 6.0.

MATERIALS AND METHODS

Methodology

Exact distribution of the Wilcoxon rank sum test

The Wilcoxon Rank Sum Test is a nonparametric alternative to the two-sample t-test. Suppose we have two independent samples $X_{1,}X_2...,X_{n_1}$ and $Y_1,Y_2,...,Y_{n_2}$ of sizes n_1 and n_2 drawn from two continuous populations whose distributions are F and G respectively. We wish to test the null hypothesis $H_0: F = G$. The alternatives could be $H_1: F > G,\ \ H_1: F < G,\ \ H_1: F \neq G,$. The Wilcoxon Rank Sum Test statistic WRS[n_1, n_2] is the sum of the ranks from one of the samples. That is

$$\text{WRS}[\, n_1, n_2\,] = \sum_{i=1}^{n_1} r_{1i}, \qquad [1]$$

Where $r_{1i,}, i = 1(1)n_1$ represents the ranks of the first sample.

It rejects the null hypothesis H_0 if the sum of the ranks of the X_i`s in the combined ordered arrangement of the two samples is either too large or too small. Here, too large or two small implies WRS[n_1, n_2] $\geq W_{1-\alpha}$ or WRS[n_1, n_2] $\leq W_{\alpha}$ respectively. $W_{1-\alpha}$ and W_{α} are the upper-tail and lower-tail exact critical values respectively of the distribution of WRS[n_1, n_2] and α is the level of significance of the test. The values for $W_{1-\alpha}$ and W_{α} are provided in Table 1 The null distribution of WRS[n_1, n_2] is found by assuming that X_i and Y_j are identically distributed. This is true only when H_0 is true in the two-tailed test. If the X_i and the Y_j are independent and identically distributed, then every arrangement of the X's and Y's in the ordered combined sample is equally likely. This is the basic principle behind many rank tests.

The probability distribution of WRS[n_1, n_2] may be obtained by considering the probability distribution of the sum of n_1 integers selected at random, without replacement, from among the integer from 1 to $n_1 + n_2$. The number of ways of selecting n_1 integers from a total number of $n_1 + n_2$ integers is

$$\Phi = \binom{n_1 + n_2}{n_1} = \frac{(n_1 + n_2)!}{n_1! n_2!} \qquad [2]$$

and each has probability Φ^{-1} of occurring. Hence the probability that WRS[n_1, n_2]= K_1 may be found by counting the number of different sets of n_1 integers from 1 to $n_1 + n_2$ that add up to the value K_1 and then dividing by Φ. However, as the sample sizes increase, it becomes difficult to obtain the distribution of WRS[n_1, n_2] because of the very large cardinality of the permutation sample spaces. As an example, if $n_1 = n_2$ =15, there are 155,117,520 associated permutation sample spaces. In such instances, the large sample approximation is usually used. But, there is no clear definition of what constitute a large sample for WRS[n_1, n_2], (Fahoome, 2002; Ogbonmwan *et al.*, 2007).

To calculate the probability that a statistic *X* based on ranks will take a value *x* which we denote as $\Pr ob(\{X = x\})$, it is therefore only necessary to obtain the number of cases satisfying the condition $X = x$. Following the idea of Baglivo *et al*. (1996), we formulate a combinatorial problem and develop generating functions to solve the problem formulated. This provides useful insight into the exact null distribution of the WRS statistic.

Combinatorial Problem

Suppose we have n observations which are ranked 1, 2, 3…, n. In how many different ways is it possible to divide these n observations among k samples such that the i^{th} sample T_i contains n_i observations and the sum of the ranks of these n_i observations in sample T_i is r_i with $n = \sum_{i=1}^{k} n_i$ and $r = \sum_{i=1}^{k} r_i = \frac{1}{2} n(n+1)$? Let the number be:

$$P[nlist, rlist] := P[\{n_{1,} n_{2,}..., n_k\}, \{r_{1,} r_2..., r_k\}] \qquad [3]$$

We can calculate this number $P[nlist, rlist]$ by counting the relevant partitions. There are $\frac{(n_1 + n_2 + ... + n_k)!}{n_1! n_2! ..., n_k!}$ possible permutations of the n variates of the k samples of sizes $n_i, i = 1,2,..., k$ which are equally likely with probability $\left(\frac{n!}{n_1! n_2! ..., n_k!} \right)^{-1}$. The number $P[nlist, rlist]$ can easily be obtained for small n and k by counting the relevant partitions, for example, $P[\{3,2\},\{8,7\}] = 2$ which requires only 10 distinct arrangements (partitions). However, when n and k are not as small as in the above example, this method of obtaining $P[nlist, rlist]$ fails because of the large associated permutation sample spaces. For instance, when $n_1 = 10, n_2 = 7, n_3 = 3$, there are 22,170,720 distinct arrangements of the ranks. Admittedly, it is very difficult to carry out this enumeration manually in order to compute $P[nlist, rlist]$.

To overcome this problem of enumeration, we find the generating function for the number $P[nlist, rlist]$. To do this, Let $x[i]$ be a variable governing the number of observations in the i^{th} sample and $y[i]$ be a variable governing the sum of the ranks of the observations in the i^{th} sample. Then, the generating function for the number $P[nlist, rlist]$ is given as

$$p[n,k] = \prod_{j=1}^{n} \left(\sum_{i=1}^{k} x[i] y[i]^j \right) \qquad [4]$$

See Ewere and Ogbonmwan (2010a)

Obviously, the numbers $P[nlist, rlist]$ are the coefficients of $\prod_{i=1}^{k} x[i]^{n_i} y[i]^{r_i}$ of the polynomial $p[n,k]$. Hence, $P[nlist, rlist]$ is obtained by selecting the coefficients of $\prod_{i=1}^{k} x[i]^{n_i} y[i]^{r_i}$. However, this method of enumeration is not as fast as one would expect due to the fact that the number of terms of the generating function in eqn [4] are of order k^n which is not too small even if n and k are not very large.

To improve on the computational efficiency of eqn [4], we let $nlist = \{n_1, n_2, ..., n_k\}$. In this case, the generating function $p[nlist]$ for the number $P[nlist, rlist]$ have number of terms whose order is only $Multinomial[n_1, n_2, ..., n_k]$ which is smaller than k^n. Clearly, this new generating function $p[nlist]$ are the coefficients of $\prod_{i=1}^{k} x[i]^{n_i}$ of the generating function $p[n,k]$. To speed up computations, the generating function $p[nlist]$ is defined recursively as:

$$p[nlist] = p[\{n_1, n_2, ..., n_k\}] = \sum_{i=1}^{k} y[i]^n \, p[\{n_1, n_2, ..., n_i - 1, ..., n_k\}] \qquad [5],$$

See Ewere and Ogbonmwan (2010b).

In eqn [5], the number of ranked observations in the i^{th} sample is reduced by one during the exchangeability (rearrangement) process by allowing the n^{th} rank to be a member of the i^{th} sample. By being systematic and proceeding in this orderly fashion from one rearrangement to the next, we have substantially reduced the time required to examine a series of rearrangements. This idea has been suggested by Good (2000).

The exact null distribution of WRS[n_1, n_2] is obtained by finding the generating function of the test statistic. The generating function for WRS[n_1, n_2] can be written as:

$$G[WRS[n_1, n_2]] = \sum Prob(\{WRS[n_1, n_2] = K_1\}) t^{K_1} \qquad [6]$$

$$0 \le K_1 \le \frac{n(n+1)}{2} \text{ and } K_2 = \frac{n(n+1)}{2} - K_1 \qquad [7]$$

Then

$$Prob(\{WRS[n_1, n_2] = K_1\}) = \frac{P[\{n_1, n_2\}, \{K_1, K_2\}]}{Binomial[n, n_1]} \qquad [8]$$

where $n = n_1 + n_2$ and $Binomial[n, n_1] = \frac{(n_1 + n_2)!}{n_1! n_2!}$

Eqn [6] can be used to calculate the distributional characteristics of WRS [n_1, n_2].

The large sample approximation

When sample sizes are large, the time required to compute a permutation distribution can be prohibitive even if we are taking advantage of one of the optimal computing algorithm (Good, 2000). Fortunately, when sample sizes are large, we can make use of an asymptotic approximation in place of the exact distribution. However, asymptotic approximations are to be avoided except with very large samples (Good, 2000). This is because they can be grossly in error (Micceri, 1989; Mudholkar and Hutson, 1997).

Table 1. Exact Critical Values for the Wilcoxon Rank Sum test.

n_1	n_2	$W_{0.9000}$	$W_{0.9500}$	$W_{0.9750}$	$W_{0.9900}$	$W_{0.9950}$	$W_{0.9975}$	$W_{0.9990}$
2	2	-	-	-	-	-	-	-
	3	8 (3)	-	-	-	-	-	-
	4	10 (4)	-	-	-	-	-	-
	5	11 (5)	12 (4)	-	-	-	-	-
3	3	13 (7)	14 (6)	-	-	-	-	-
	4	16 (8)	17 (7)	-	-	-	-	-
	5	18 (9)	19 (8)	20 (7)	-	-	-	-
	6	20 (10)	21 (9)	22 (8)	-	-	-	-
4	4	22 (13)	24 (12)	25 (11)	-	-	-	-
	5	25 (15)	27 (13)	28 (12)	29 (11)	-	-	-
	6	28 (16)	30 (14)	31 (13)	32 (12)	33 (11)	-	-
	7	31 (17)	33 (15)	34 (14)	36 (12)	37 (11)	-	-
5	5	34 (21)	35 (20)	37 (18)	38 (17)	39 (16)	-	-
	6	37 (23)	39 (21)	41 (19)	42 (18)	43 (17)	44 (16)	-
	7	41 (24)	43 (22)	44 (21)	46 (19)	48 (17)	49 (16)	-
	8	44 (26)	46 (24)	48 (22)	50 (20)	52 (18)	53 (17)	54 (16)
6	6	47 (31)	49 (29)	51 (27)	53 (25)	54 (24)	55 (23)	-
	7	51 (33)	54 (30)	56 (28)	58 (26)	59 (25)	60 (24)	62 (22)
	8	55 (35)	58 (32)	60 (30)	62 (28)	64 (26)	65 (25)	67 (23)
	9	59 (37)	62 (34)	64 (32)	67 (29)	69 (27)	70 (26)	72 (24)
7	7	63 (42)	65 (40)	68 (37)	70 (35)	72 (33)	73 (32)	75 (30)
	8	67 (45)	70 (42)	73 (39)	76 (36)	77 (35)	79 (33)	81 (31)
	9	72 (47)	75 (44)	78 (41)	81 (38)	83 (36)	85 (34)	87 (32)
	10	76 (50)	80 (46)	83 (43)	86 (40)	88 (38)	90 (36)	92 (34)
8	8	80 (56)	84 (52)	86 (50)	90 (46)	92 (44)	93(43)	95(41)
	9	85 (59)	89 (55)	92 (52)	96 (48)	98 (46)	100(44)	102(42)
	10	91 (61)	95 (57)	98 (54)	102 (50)	104 (48)	106(46)	109(43)
	11	96 (64)	100 (60)	104 (56)	108 (52)	110 (50)	112(48)	115(45)
9	9	100(71)	104(67)	108(63)	111(60)	114(57)	116(55)	118(53)
	10	106(74)	110(70)	114(66)	118(62)	121(59)	123(57)	126(54)
	11	112(77)	116(73)	120(69)	125(64)	127(62)	130(59)	133(56)
	12	117(81)	122(76)	126(72)	131(67)	134(64)	137(61)	140(58)
10	10	122(88)	127(83)	131(79)	135(75)	138(72)	141(69)	144(66)
	11	128(92)	133(87)	138(82)	142(78)	146(74)	148(72)	152(68)
	12	135(95)	140(90)	145(85)	150(80)	153(77)	156(74)	160(70)
	13	141(99)	147(93)	151(89)	157(83)	160(80)	164(76)	167(73)
11	11	146(107)	152(101)	156(97)	161(92)	165(88)	168(85)	171(82)
	12	153(111)	159(105)	164(100)	169(95)	173(91)	176(88)	180(84)
	13	160(115)	166(109)	171(104)	177(98)	181(94)	184(91)	188(87)
	14	167(119)	173(113)	179(107)	185(101)	189(97)	193(93)	197(89)
12	12	172(128)	179(121)	184(116)	190(110)	194(106)	197(103)	201(99)
	13	180(132)	186(126)	192(120)	198(114)	202(110)	206(106)	210(102)
	14	187(137)	194(130)	200(124)	207(117)	211(113)	215(109)	220(104)
	15	194(142)	202(134)	208(128)	215(121)	220(116)	224(112)	229(107)
13	13	201(150)	208(143)	214(137)	220(131)	225(126)	229(122)	233(118)
	14	209(155)	216(148)	222(142)	229(135)	234(130)	238(126)	243(121)
	15	217(160)	224(153)	231(146)	238(139)	243(134)	248(129)	253(124)
14	14	231(175)	239(167)	245(161)	253(153)	258(148)	262(144)	268(138)
	15	240(180)	248(172)	255(165)	263(157)	268(152)	273(147)	278(142)
15	15	264(201)	272(193)	280(185)	288(177)	293(172)	298(167)	304(161)
20	20	458(362)	471(349)	482(338)	495(325)	504(316)	512(308)	521(299)
30	30	1002(898)	1026(868)	1047(846)	1071(822)	1088(807)	1102(793)	1120(776)
40	40	1754(1486)	1791(1449)	1823(1417)	1861(1379)	1886(1354)	1909(1331)	1937(1303)
50	50	2711(2339)	2764(2286)	2809(2241)	2861(2189)	2897(2153)	2929(2121)	2969(2081)
60	60	3875(3405)	3944(3345)	4003(3295)	4072(3241)	4118(3206)	4161(3175)	4214(3138)

Several researchers have described the use of classic parametric statistics in the face of assumption violations as invalid (Keselman *et al.*, 1998; Leech and Onwuegbuzie, 2002; Wilcox, 2001; Grissom and Kim, 2005; Erceg-Hurn and Mirosevich, 2008). To better understand this, Royeen (1986) identified five published studies that used parametric statistics. For each study, the data were checked whether they met the assumptions for the parametric statistics used. In three of the five studies, the assumptions were not met. Next, the appropriate nonparametric statistic was computed on the data. For each of the three studies that did not meet the assumptions, there were large differences in the results yielded by the nonparametric statistic when compared with the published results from the parametric statistic. Thus, this examination demonstrates that if the assumptions are not met, the results can be very misleading.

The fundamental asymptotic result for the permutation distribution of the two-sample test statistic for a location parameter was first stated by Madow (1948) and formalized by Hoeffding (1951, 1952) who demonstrated convergence of the distribution of the studentized test statistic under the alternative as well as under the null hypothesis.

Let $T_n = T\left(X_{(1)},..., X_{(n)}\right)$ be the test statistic and let μ_n and σ_n be its first and second moments respectively. Then the permutation distribution F_n of Z_n is $\frac{T_n - \mu_n}{\sigma_n}$ [9]

Eqn [9] is obtained by randomly rearranging the subscripts of the arguments of T_n and this converges to ϕ, the Gaussian (normal) distribution function.

To enable researchers who do not have access to the necessary tables of critical values to employ these tests, it is important to determine the minimum sample size in order to apply the large sample approximation for various statistics. Besides, the statistical assumption tests built into software such as SPSS often do a poor job of detecting violations from normality and homoscedasticity (Jaccard and Guilamo-Ramos, 2002).

In order to determine the minimum sample size required for the application of asymptotic results of the WRS test, we use the Bradley's (1978) conservative estimates of 0.045 < Type I error rate < 0.055 and 0.009 < Type I error rate < 0.011 as measures of robustness when nominal α was set at 0.05 and 0.01, respectively. Generally, the stringent criterion $0.9\alpha \le \alpha_0 \le 1.1\alpha$ where α_0 is the true probability of a type I error when one or more of a test's assumptions are violated and the null hypothesis is true seems more appropriate to illustrations of 'convergence' than the liberal criterion given by Cochran (1952), who considered actual significance levels less than 20% above the nominal level to be acceptable, Sullivan and D'Agostino (1992). The sample sizes were increased until the Type I error rates converged within these acceptable regions.

RESULTS AND DISCUSSION

The values in each cell of Table 1 represent the upper and lower critical values of the Wilcoxon Rank Sum test statistic with the lower critical values in brackets. We study the convergence of the asymptotic distribution (the normal distribution) to the exact distribution of the WRS test both numerically and graphically in Tables 1 through 7 and Figures 1 through 10. We determine the minimum sample size in order to apply the asymptotic distribution using the Bradley's conservative estimate.

Table 2. Exact and Asymptotic Type I error rates for WRS $\alpha = 0.01$

n_1	n_2	**Exact**	**Asymptotic**
5	5	0.00793651	0.0141401
6	6	0.00757576	0.0124873
7	7	0.00874126	0.0126737
8	8	0.00738151	0.0104313
9	9	0.00937886	0.0121705
10	10	0.00927169	0.0116711
11	11	0.00961538	0.0117428
12	12	0.0086356	0.0104607
13	13	0.00954935	0.0112432
14*	14*	0.00927701	0.0107985
15	15	0.00927686	0.0106667
16	16	0.00946554	0.0107518
17	17	0.00979409	0.0109963
18	18	0.00935297	0.0104547
19	19	0.00991213	0.0109589
20	20	0.00976838	0.0107452

Table 3. Exact and Asymptotic Type I error rates for WRS $\alpha = 0.025$

n_1	n_2	**Exact**	**Asymptotic**
4	4	0.014286	0.021654
5	5	0.015873	0.023601
6	6	0.0205628	0.027332
7	7	0.0189394	0.0238227
8	8	0.0249417	0.0293536
9*	9*	0.0199918	0.0234728
10	10	0.0216285	0.0246835
11	11	0.0236536	0.0263654

12	12	0.022451	0.0248236
13	13	0.0220583	0.0241705
14	14	0.0248678	0.0268157
15	15	0.0226669	0.0244071
16	16	0.0234075	0.0250082
17	17	0.0243428	0.0258237
18	18	0.0235424	0.0249051
19	19	0.0248279	0.0261017
20	20	0.0245452	0.0257312

Table 4. Exact and Asymptotic Type I error rates for WRS $\alpha = 0.05$

n_1	n_2	**Exact**	**Asymptotic**
4	4	0.0285714	0.0416323
5	5	0.047619	0.0585927
6	6	0.0465368	0.0546573
7	7	0.0486597	0.0551116
8*	8*	0.0414918	0.046446
9	9	0.046956	0.0511725
10	10	0.0446048	0.0481518
11	11	0.0439731	0.0470205
12	12	0.0443669	0.0470343
13	13	0.0454236	0.0477904
14	14	0.0469341	0.049052
15	15	0.0487629	0.0506708
16	16	0.0469062	0.0486272
17	17	0.0493437	0.0509127
18	18	0.0485296	0.0499635
19	19	0.0482046	0.0495223
20	20	0.0482498	0.049466

Table 5. Exact and Asymptotic Type I error rates for WRS $\alpha = 0.10$

n_1	n_2	**Exact**	**Asymptotic**
3	3	0.10000	0.137617
4	4	0.10000	0.124106
5	5	0.075397	0.0872629
6	6	0.089827	0.100092
7	7	0.082459	0.0898563
8*	8*	0.097436	0.103789
9	9	0.095125	0.100206
10	10	0.095158	0.099383
11	11	0.096593	0.10019
12	12	0.098904	0.102012
13	13	0.092844	0.0954888
14	14	0.096789	0.0991284
15	15	0.093634	0.095681
16	16	0.098187	0.100023
17	17	0.096608	0.098242
18	18	0.095819	0.0972845
19	19	0.095621	0.0969432
20	20	0.095876	0.0970745

Table 6. Exact and Asymptotic Type I error rates for WRS $\alpha = 0.005$

n_1	n_2	**Exact**	**Asymptotic**
5	5	0.00396825	0.00814685
6	6	0.004329	0.0081546
7	7	0.0034965	0.00635814
8	8	0.0034965	0.00585932
9	9	0.00388729	0.00592465
10	10	0.00446535	0.00630572
11	11	0.00416482	0.00573401
12	12	0.00414658	0.0055372
13	13	0.00430052	0.00556705
14	14	0.00457314	0.0057501
15	15	0.00493741	0.00604638
16	16	0.00477527	0.00578232
17	17	0.00474725	0.00567714
18	18	0.00481544	0.00568552
19	19	0.00495689	0.00577918
20	20	0.0047418	0.0054999
21	21	0.00462845	0.0053353
22	22	0.00493681	0.00562165
23	23	0.00493478	0.00558331
24	24	0.0049846	0.00560284
25*	25*	0.00478432	0.00536339
26	26	0.00492306	0.0054817
27	27	0.00482933	0.00535919
28	28	0.00478341	0.00528889
29	29	0.00477642	0.00526094
30	30	0.00480184	0.00526824
31	31	0.00485479	0.0053054
32	32	0.00493154	0.00536824
33	33	0.00483841	0.00525655
34	34	0.00495948	0.00536708
35	35	0.00491999	0.00531282

Table 7. Exact and Asymptotic Type I error rates for WRS $\alpha = 0.0025$

n_1	n_2	**Exact**	**Asymptotic**
6	6	0.0021645	0.00520282
7	7	0.00203963	0.00440432
8	8	0.002331	0.00432575
9	9	0.00199506	0.00353844
10	10	0.0019431	0.00325094
11	11	0.00205123	0.0032141
12	12	0.00225653	0.00332835
n_1	n_2	**Exact**	**Asymptotic**
13	13	0.00210757	0.00303857
14	14	0.00245278	0.00335493
15	15	0.00246981	0.00329566
16	16	0.00224209	0.00296805
17	17	0.00239608	0.00308823
18	18	0.00232243	0.00295661
19	19	0.00230915	0.00289976
20	20	0.0023406	0.00289799

21	21	0.00240712	0.00293864
22	22	0.00231233	0.00280479
23	23	0.00243746	0.00291553
24	24	0.00241165	0.00286333
25	25	0.00241661	0.00284695
26	26	0.00244654	0.00285945
27	27	0.00249737	0.00289584
28	28	0.00243136	0.0028082
29	29	0.00239359	0.0027524
30	30	0.0024972	0.00284885
31	31	0.00249536	0.0028336
32	32	0.00240266	0.00272278
33	33	0.00243653	0.00274742
34	34	0.00248261	0.00278551
35*	35*	0.00244438	0.00273515
36	36	0.00242278	0.00270304
37	37	0.0024153	0.00268644
38	38	0.00242002	0.0026832
39	39	0.00243542	0.00269159
40	40	0.0024603	0.00271038
41	41	0.0024937	0.00273834
42	42	0.00246273	0.00269937
43	43	0.0024433	0.00267283
44	44	0.00243394	0.00265723
45	45	0.00249759	0.00271778

Plots of the exact and asymptotic cumulative distribution functions of the WRS test statistic for different sample sizes.

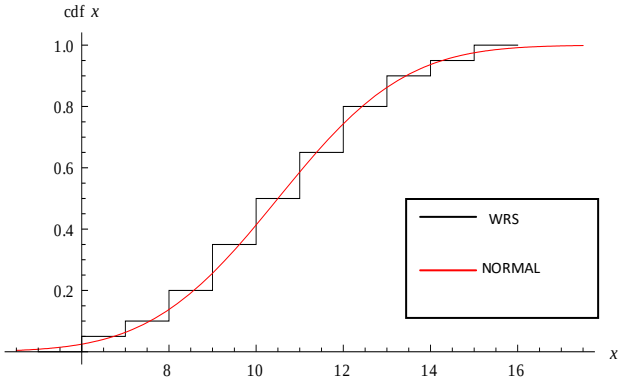

Fig. 1. $n_1 = n_2 = 3$

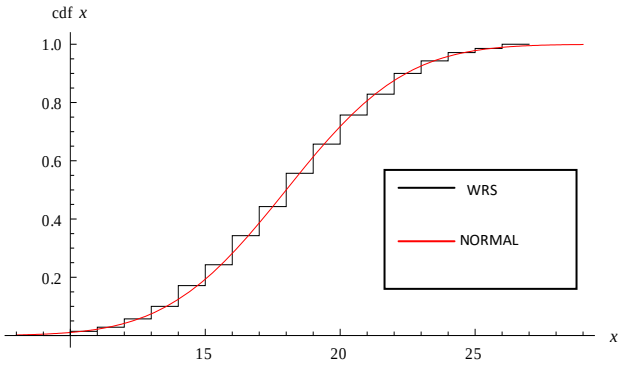

Fig. 2. $n_1 = n_2 = 4$

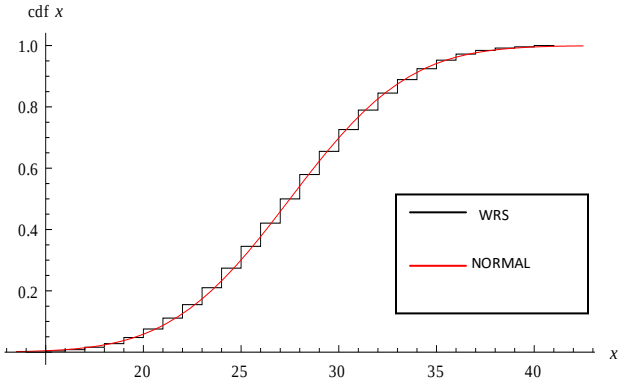

Fig. 3. $n_1 = n_2 = 5$

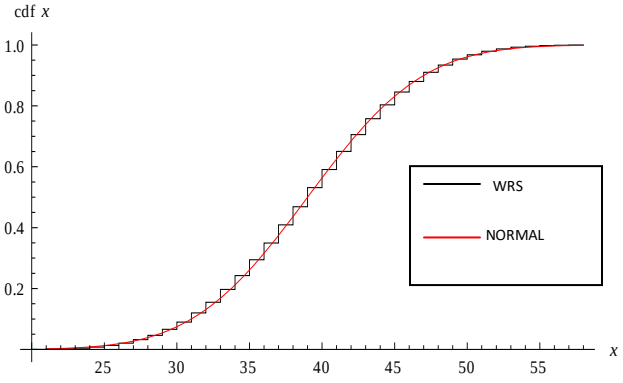

Fig. 4. $n_1 = n_2 = 6$

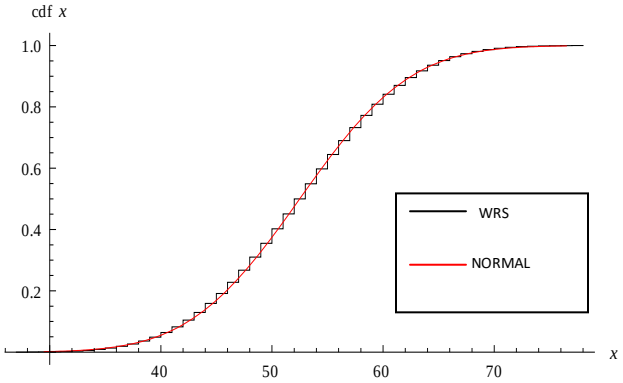

Fig. 5. $n_1 = n_2 = 7$

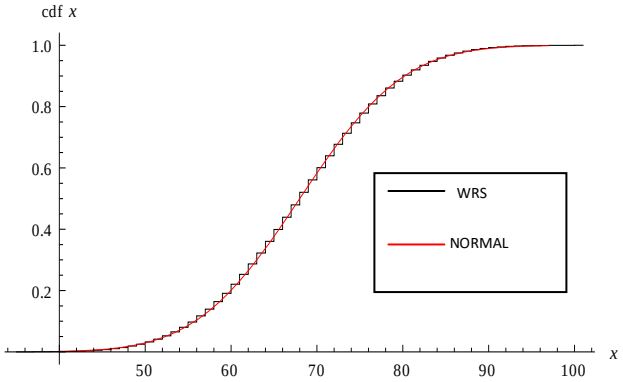

Fig. 6. $n_1 = n_2 = 8$

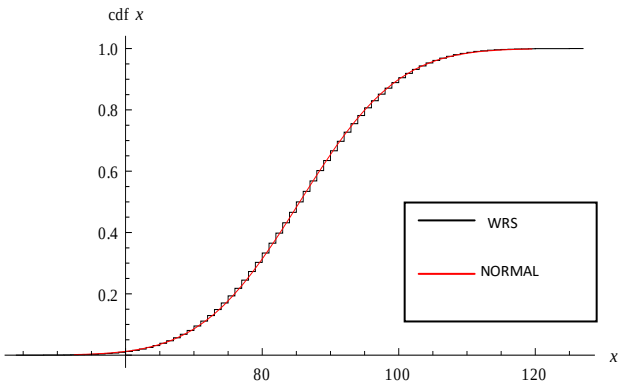

Fig. 7. $n_1 = n_2 = 9$

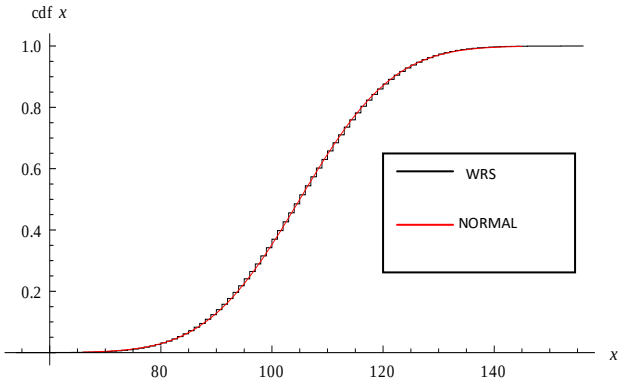

Fig. 8. $n_1 = n_2 = 10$

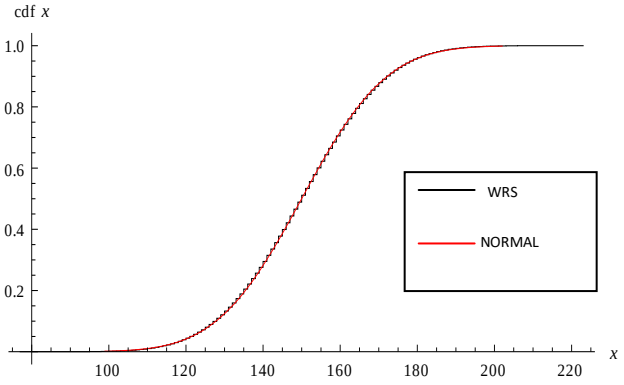

Fig. 9. $n_1 = n_2 = 12$

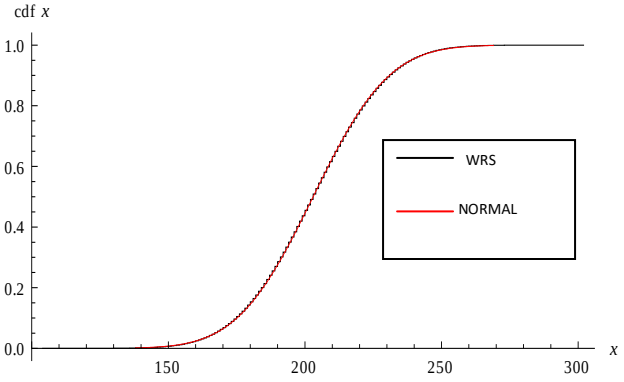

Fig. 10. $n_1 = n_2 = 14$

Table 1 provides exact critical values for the WRS test statistic. The exact critical values for the test statistic has been provided for some combination of sample sizes as it is not practical to present the entire distribution here, but these are easily obtained from the computer program available on request from the authors.

When sample sizes are large, it is reasonable to use the large sample approximation. But the question has always been "How large is large? Providing exact critical values for the WRS test statistic for small and larger samples do not only negate the need for approximations in many additional settings, but they also allow us to study the approximation and make more reasonable inference about the usefulness of the approximation. What we are more concerned about is what the performance of the approximation in the smaller-sample conditions might imply about conditions for which there are still no exact tables.

Tables 2 through 7 shows the exact and asymptotic Type I error rates for the WRS test statistic for nominal level of significance $\alpha = 0.01,\ 0.025,\ 0.05, 0.10, 0.005$ and 0.0025 respectively. We use these results to determine the minimum sample sizes necessary to use the large sample approximation of the critical value of the WRS statistic. We superimpose the curve of the normal distribution to that of the WRS in Figures 1 through Figures 10. The exact distribution of the WRS test becomes more stable and closer to the normal distribution as the group sample size increases as depicted in Figures 1 through 10. The normal approximation of the exact critical values of the WRS test is adequate when $n_1 = n_2 = 14$ (14 per sample) for $\alpha = 0.01$, $n_1 = n_2 = 9$ for $\alpha = 0.025$, $n_1 = n_2 = 8$ for $\alpha = 0.05$ and 0.10. A minimum of 25 and 35 per sample is adequate to apply the normal approximation for $\alpha = 0.005$ and $\alpha = 0.0025$ respectively. The minimum sizes per sample required to apply the asymptotic distribution have been reported and are asterisked in Tables 2 through 7. These recommendations in this paper are based on the results that converged using the Bradley's (1978) conservative estimates.

It is instructive here to point out the contributions of other authors as regards the minimum sample size for the application of the large sample approximation for the WRS statistic. Mann and Whitney (1947) considered the case of unpaired data with samples of equal sizes and reported tables only up to sample sizes of 8, that is, $n_1 = n_2 = 8$ and concluded that "*at this point the distribution is almost normal*". They probably failed to recognize the influence upon robustness of α, Bradley (1978). And very early, it was thus acknowledged that the

normal approximation was acceptable for rather small sample sizes. Conover (1971) recommended that one or both sample must exceed 20. Gibbons (1971) placed the lower limit at 12 per sample. Another study Sprent (1989) also suggested that one or both samples must exceed 20. While, Deshpande *et al*. (1995) stated that the combined sample size should be at least 20 to use a large sample approximation of the critical value of the WRS statistic. Fahoome (2002) recommended a minimum of 15 and 29 per sample for $\alpha = 0.05$ and $\alpha = 0.01$ respectively. Ogbonmwan *et al*. (2007) suggested a minimum of 7 per sample to apply the asymptotic results for $\alpha = 0.05$. The definition of what constitute a large sample for the WRS test is quite vague. We have attempted to address this vagueness in this article. The results in Table 2 clearly demonstrate that the large sample approximation of the critical value prevents the statistic from converging with nominal $\alpha = 0.01$ if Bergmann et. al (2000) are correct with their perception of common practices using as few as 11 per sample.

CONCLUSION

In this study, a straight forward but logical approach has been adopted in developing a procedure for constructing an exact test of significance. With this approach, the exact critical values of the Wilcoxon Rank Sum test have been accurately generated, thereby ensuring that the probability of making a type I error is exactly α. Numerical evaluations and graphical illustrations of the asymptotic property of the WRS test have been presented. We feel, however, that such representations (numerical and graphical) could be valuable tools when introducing these statistics. This claim is well exemplified by the following quotation from Bellera *et al*. (2010):

We examined a convenience sample of 12 introductory statistics textbooks and three nonparametric statistics textbooks available to students at the McGill University Science Library. None of these books included graphical display of the distributions of the Wilcoxon Statistics. Only one book (Lehmann, 1998) included recursive formulas.

REFERENCES

Agresti, A. 1992. A survey of exact inference for contingency tables. Statistical Science. 7: 131-177.

Baglivo, J., Pagano, M. and Spino, C. 1996. Permutation distributions via generating function with applications to sensitivity analysis of discrete data. Journal of the American Statistical Association. 91:1037-1046.

Bagui, S. and Bagui, S. 2004. An algorithm and code for computing exact critical values for the Kruskal-Wallis nonparametric one-way ANOVA. Journal of Modern Applied Statistical Methods. 3:498-503.

Bayarri, MJ. and Berger, JO. 2004. The interplay of Bayesian and frequentist analysis. Statistical Science. 19:58-80.

Bellera, CA., Julien, M. and Hanley, JA. 2010. Normal approximations to the Distributions of the Wilcoxon Statistics: Accurate to What N? Graphical Insights. Journal of Statistics Education. 18(2):1-17.

Bergmann, R., Ludrook, J. and Spooren, WPJM. 2000. Different outcomes of the Wilcoxon-Mann-Whitney test from different statistics packages. American Statistician. 54:72-77.

Bradley, JV. 1978. Robustness? British Journal of Mathematical and Statistical Psychology. 31:144-152.

Cochran, WG. 1952. The χ^2 test of goodness of fit. Ann Math Stat. 23:315-345.

Conover, WJ. 1971. Practical Nonparametric statistics. Wiley and Sons Inc., New York, USA.

Deshpande, JV, Gore, AP. and Shanubhogue, A. 1995. Statistical analysis of non-normal data. John Wiley and Sons, Inc., New York, USA.

Efron, B. 1979. Bootstrap methods: another look at the Jackknife. The Annals of Statistics. 7:1-26.

Erceg-Hurn, DM. and Mirosevich, VM. 2008. Modern robust statistical methods: An easy way to maximize the accuracy and power of your research. American Psychologist. 63(7):591- 601.

Ewere, F. and Ogbonmwan, SM. 2010[a]. A method for generating the permutation distribution of ranks in a k-sample experiment. Journal of the Nigerian Association of Mathematical Physics. 16:579-584.

Ewere, F. and Ogbonmwan, SM. 2010[b]. A fast algorithm for generating the permutation distribution of ranks in a k-sample experiment. Journal of the Nigerian Association of Mathematical Physics. 16:585-590.

Ewere, F. and Ogbonmwan, SM. 2020. Exact Critical Values of the Kruskal Wallis Test. Canadian Journal of Pure and Applied Sciences. 14(3):5105-5115.

Fahoome, G. 2002. Twenty Nonparametric Statistics and their large sample Approximations. Journal of Modern Applied Statistical Methods. 1:248-268.

Gibbons, JD. 1971. Nonparametric statistical inference. McGraw-Hill book Company. New York, USA.

Good, P. 2000. Permutation Tests: A practical Guide to Re-sampling methods for Testing Hypothesis (2nd edi.). Springer-Verlag, New York, USA.

Grissom, RJ. and Kim, JJ. 2005. Effect sizes for research: A broad practical approach. Mahwah, NJ: Erlbaum.

Headrick, TC. 2003. An algorithm for generating exact critical values for the Kruskal-Wallis One-Way ANOVA. Journal of Modern Applied Statistical Methods. 2:268-271.

Hoeffding, W. 1951. Combinatorial central limit theorem. Ann. Math. Statist. 22:556-558.

Hoeffding, W. 1952. Large sample power of tests based on permutations of observations. The Annals of Mathematical Statistics. 23:169-192.

Jaccard, J. and Guilamo-Ramos, V. 2002. Analysis of variance frameworks in clinical child and adolescent psychology: Advanced issues and recommendations. Journal of Clinical Child Psychology. 31:278-294.

Keselman, HJ., Huberty, CJ., Lix, LM., Olejnik, S., Cribbie, RA. and Donahue, B. 1998. Statistical practices of educational researchers: An analysis of their ANOVA, MANOVA, and ANCOVA analyses. Review of Educational Research. 68:350-386.

Leech, NL. and Onwuegbuzie, AJ. 2002. A call for greater use of nonparametric statistics. Paper presented at the Annual Meeting of the Mid South Educational Research Association. Retrievedfromhttp://www.eric.ed.gov/ERICWebPortal/contentdelivery/servlet/ERICServlet?accno=ED471346.

Lehmann, E. 1998. Nonparametrics-Statistical Methods Based on Ranks (Revised 1st edi.). San Francisco: Holden-Day Inc.

Lehmann, EL. 1986. Testing Statistical Hypothesis. (2 nd edi.). Wiley, New York, USA.

Madow, WG. 1948. On the limiting distribution of estimates based on samples from finite universes. Ann. Math. Stat. 19:534-545.

Mann, HB. and Whitney, DR. 1947. On a test of whether one of two random variables is stochastically larger than the other. Annals of Mathematical Statistics. 18:50-60.

Miccceri, T. 1989. The unicorn, the normal curve, and other improbable creatures. Psychological Bulletin. 105:156-166.

Mudholkar, GS. and Hutson, AD. 1997. Continuity corrected approximations for and "exact" inference with Pearson's chi-square. J. Statist. Plan. Infer. 23:61-78.

Odiase, JI. and Ogbonmwan, SM. 2005. An algorithm for generating unconditional exact permutation distribution for a two-sample experiment. Journal of Modern Applied Statistical Methods. 4:319-332.

Ogbonmwan, SM, Odiase, JI. and Aitusi, DN. 2007: Exact permutation critical values for the Wilcoxon Rank Sum Test. International Journal of Natural and Applied Sciences. 3(1):90- 95.

Opdyke, JD. 2003. Fast permutation tests that maximize power under conventional Monte Carlo sampling for pairwise and multiple comparisons. Journal of Modern Applied Statistical Methods. 2:27-49.

Pesarin, F. 2001. Multivariate Permutation Tests. John Wiley and Sons. New York, USA.

Royeen, CB. 1986. A comparison of parametric versus nonparametric statistics. Paper presented at the Annual Meeting of the American Educational Research Association, San Francisco, CA., USA.

Scheffe, H. 1943. Statistical Inference in the nonparametric case. The Annals of Mathematical Statistics. 14:305-332.

Spiegelhalter, DJ. 2004. Incorporating Bayesian ideas into health-care evaluation. Statistical Science. 19:156-174.

Sprent, P. 1989. Applied nonparametric statistical methods. Chapman and Hall. London.

Sullivan, LM. and D'Agostino, RB. 1992. Robustness of the t Test applied to data distorted from normality by floor effects. Journal of Dental Research. 71(12):1938-1943.

Wilcox, RR. 2001. Fundamentals of modern statistical methods. Springer. New York, USA.

Received: August 29, 2021; Revised: Sept 1, 2021;
Accepted: Sept 24, 2021

Canadian Journal of Pure and Applied Sciences
Vol. 15, No. 3, pp. 5317-5322, Oct 2021
Online ISSN: 1920-3853; Print ISSN: 1715-9997
Available online at www.cjpas.net

MAGNETIC SCALAR FIELD GENERATOR

*Vitaliy Zamsha[1] and Vladimir Shevtsov[2]
[1]International Institute for Experimental Physics, Perth, Australia
[2]International Institute for Experimental Physics, Novopolotsk, Belarus

ABSTRACT

In this work, the authors represent an innovative construction of the scalar field generator called the “scalar field gun”. The scalar field gun proposed in this article can be used as a magnetic scalar field generator for some researches in physics, biology, medicine or as a part of communication systems, etc. For educational purposes, some relevant information from free Internet sources is reviewed in this article to educate undergraduate, graduate, and postgraduate students as well as engineers and researches whose interests lie in the field of new communication technologies.

Keywords: Scalar field, magnetic generator, communication system.

INTRODUCTION

The authors of this work will talk about the scalar field and how it can be generated that was promised earlier in the book by Shkatov and Zamsha (2015). The scalar field was discovered more than 100 years ago, and the first who dealt with it was Nikola Tesla. He built different scalar field devices mainly to transfer an electrical energy. After that appeared many replicas of Tesla’s scalar field devices but all of them emit mixture of electromagnetic waves and scalar waves. Therefore, they are not good as "pure" scalar generators because they all have an "open" construction. Figure 1 shows the well-known picture of the Tesla’s scalar field tower and some “modern” replicas that are already compact devices and they occupy only a small spot on a worktable.

It is necessary to state that all of the mentioned scalar field devices can create a lot of electromagnetic interference. Thus, in order to avoid electromagnetic emissions, the authors of this article attempted to develop a "pure" scalar generator based on the magnetic scalar field theory developed by the Russian outstanding researcher Nikolaev (1997). He assumed that one deals here with a ”Second Magnetic Field”. According to the theory developed by Nikolaev, the scalar field is generated by any charge in motion. The scalar field can be also generated by an electrical current in a wire or by any charge that moves in a vacuum.

Also, the scalar field can be static or dynamic. The static scalar field is generated by a DC current or by permanent magnets. The dynamic scalar field can be generated, for instance, by a pulsed current. As mentioned above, the scalar field can be easily generated but it is difficult to register it. The scalar field has a good penetrating ability, so it is difficult to shield it. The simplest way to get a magnetic scalar field source is to take an ordinary permanent magnet from any speaker, cut it in two halves, and rotate one half on 180 degrees, and stick it back to other half. This is shown schematically in Figure 2.

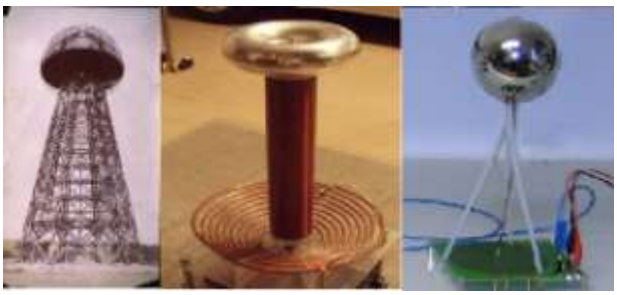

Fig. 1. The scalar field devices (from left to right): The Tesla’s tower and two of many modern “replicas” of different shapes.

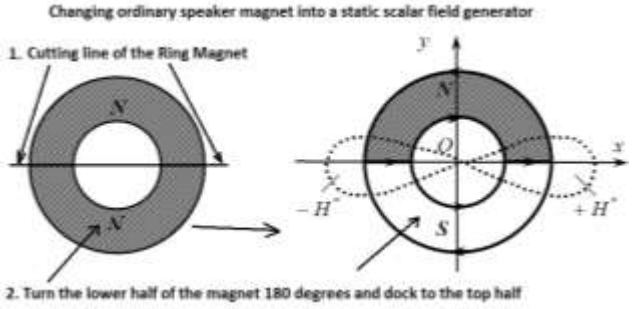

Fig. 2. The schematic representation of the simplest scalar field device, where +H* and –H* are magnetic scalar field zones.

*Corresponding author e-mail: spincom2@yandex.com

However, there exists the other way how to change any speaker magnet into a scalar field source. Place the speaker magnet into a very hot stove with +400 degrees and warm it up. When magnet warms up, it will lose its factory-made axial magnetism. Then, after magnet gets cold, wind a thick wire on its ring (~ 10 turns). Next, it is possible to connect this assembly to the car battery through the fuse of by about 25 A. So, this will be a short high current pulse and the fuse will explode and the prepared scalar field magnet will be ready to use. This method of preparing the scalar field magnet shown in Figure 3 was popularized by Sergey Deyna from Russia (https://www.youtube.com/watch?v=axe2F3xia-M). After magnetisation done, the zones of the scalar field will be oriented axially perpendicular to the plane of the toroid as shown in Figure 4.

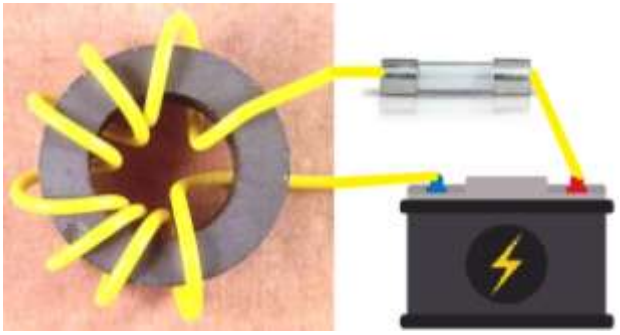

Fig. 3. The prepared scalar field magnet connected to the car battery.

Fig. 4. The toroid and the scalar field zones.

Therefore, the vector of the magnetic field is completely enclosed inside the toroid, namely in its plane. However, the scalar field is formed orthogonally to the toroid's plane, namely along the axis of the toroid (the zones + H^* and – H^* shown in Fig. 4). It is also necessary to state here that a static magnetic scalar field is not so powerful as dynamic. So, the scalar field can be generated by the use of the electrical current. Figure 5 shows how the positive and negative zones of the scalar field can be created by an electrical charge when it moves.

However, it is not efficient to create the scalar field just by one wire with the electric current in it because it is better to use two wire loops to generate the scalar field. Consider a system of two identical rectangular wire loops with the electrical current in them. It is necessary to state that the vector diagrams shown here are for illustrating the use of DC current. Figure 6 shows how the positive ($+H^*$) and negative ($-H^*$) zones of the scalar field can be created when it is utilized two wire loops fed with the DC current.

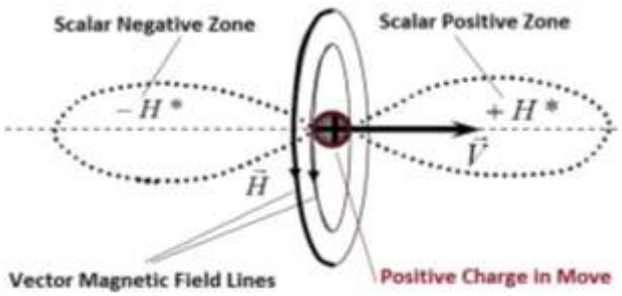

Fig. 5. The schematic representation of the creation of the positive and negative zones of the scalar field (Tomilin, 2009).

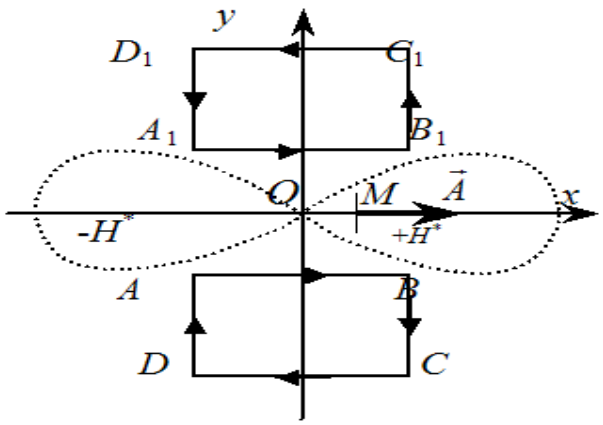

Fig. 6. The two wire loops (ABCD and $A_1B_1C_1D_1$) fed with the DC current. The arrows in the rectangular wire loops show the directions of the electrical current (Tomilin, 2009).

Further development in the scalar field theory was made by Tomilin (2009). He proposed to exploit a set of many pairs of rectangular loops around the common axis to gain more scalar field power. However, even this is not a final solution. Zamsha has proposed to "approximate" (or in other words, convert) those wire loops into the assembly of two solid hollow cylindrical tubes and two "washers": one in the front to connect the inner cylinder with the outer one and the other washer placed on the rear side of this construction to make an electrical connection between the external cylinder and the coaxial cable braiding.

The author's construction of the scalar gun

After taking into consideration all information about the scalar field, the authors of this article discussed possible design and proposed the final assembly of the magnetic scalar field gun prototype shown in Figures 7 and 8.

The prototype of the scalar gun assembled by Vladimir Shevtsov has the following sizes: the external diameter is ~ 35 mm, the internal hole diameter is ~ 12 mm, and the length is 275 mm. To increase the efficiency of the scalar field gun, it was proposed to fill the inner space between the two cylinders with ferrite rings in order to concentrate the magnetic field, and thus increase the scalar field power. So, it was prepared the sketch of the scalar field gun and Vladimir Shevtsov assembled it in Belarus.

It is assembled using two long aluminum cylinders (outer and inner) and two aluminum washers: one is placed at front and the other is rear. The internal space between these two cylinders is filled with toroidal ferrite cores. So, the scalar field can be generated by electrons (electric current) moving along the internal and outer cylinders of the scalar field gun. The magnetic field almost concentrated between the mentioned above cylinders (aluminum or copper pipes). The used ferrite cores improve the performance of the scalar field gun. The permeability of toroids is ~ 2000mu. The sketch of the scalar field gun (head) is shown in Figure 9.

Fig. 7. The assembled prototype of the magnetic scalar field gun.

Fig. 8. The other photograph of the assembled prototype of the magnetic scalar field gun.

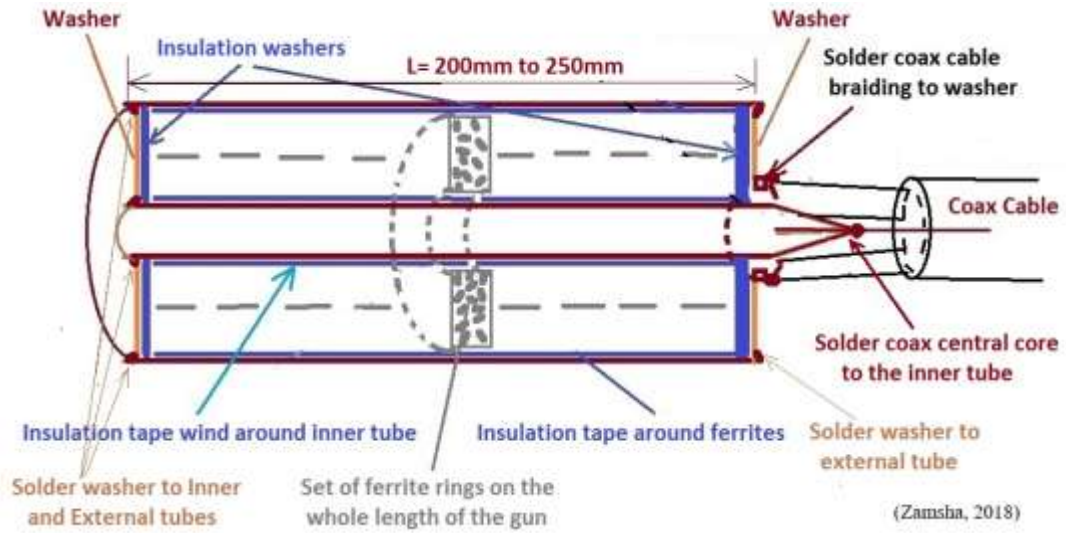

Fig. 9. The scalar gun construction.

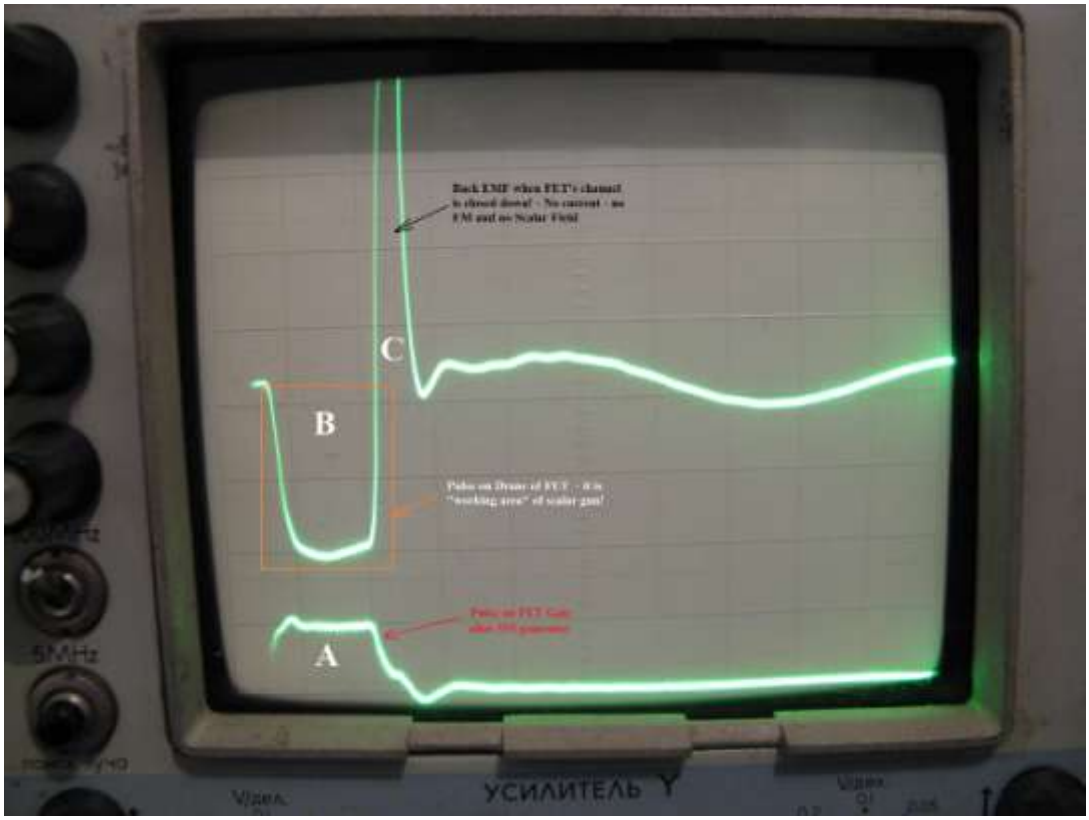

Fig. 10. The pulse transition.

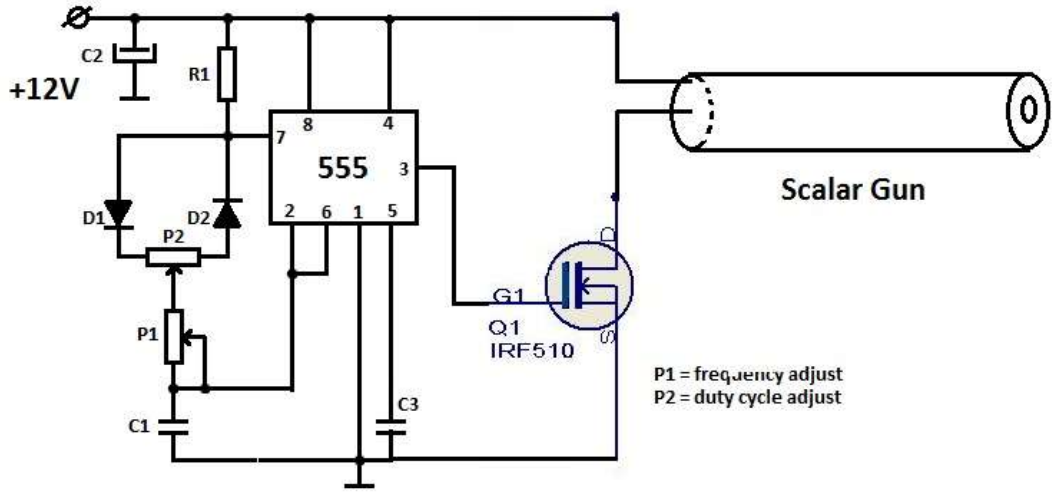

Fig. 11. The simple scheme of the scalar gun including the pulse generator.

Also, it was assembled another small prototype of the scalar field gun in Australia for testing purposes. This small prototype shown in Figure 12 works on much higher frequencies. The micro scalar gun features are as follows: the external diameter is 13 mm, the hole diameter is 4 mm, and the length (head) is by about 30 mm. The micro scalar gun is connected to a simple pulse generator as shown in Figure 13. The micro scalar gun consumes ~ 80 mA DC current, amplitude of pulses on inputs of scalar gun was ~ 33 V. Figure 14 shows the observed phasing of W1 and W2 winds to get correct pulsing. Note that the schematics represented here just give an idea how the scalar gun can be assembled. The pulses of the micro scalar gun have ~ 25 ns width, and the period is ~ 1.5 μs. The full schematic diagram of the scalar gun is shown in Figure 15.

Fig. 12. The small prototype assembled in Australia.

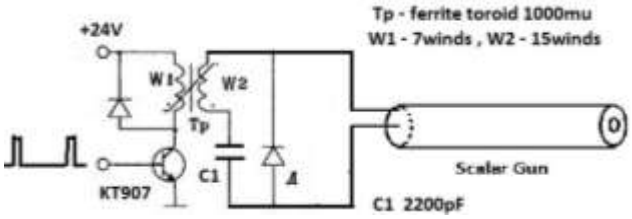

Fig. 13. The micro scalar field gun with the simple pulse generator.

Fig. 14. The observed pulses.

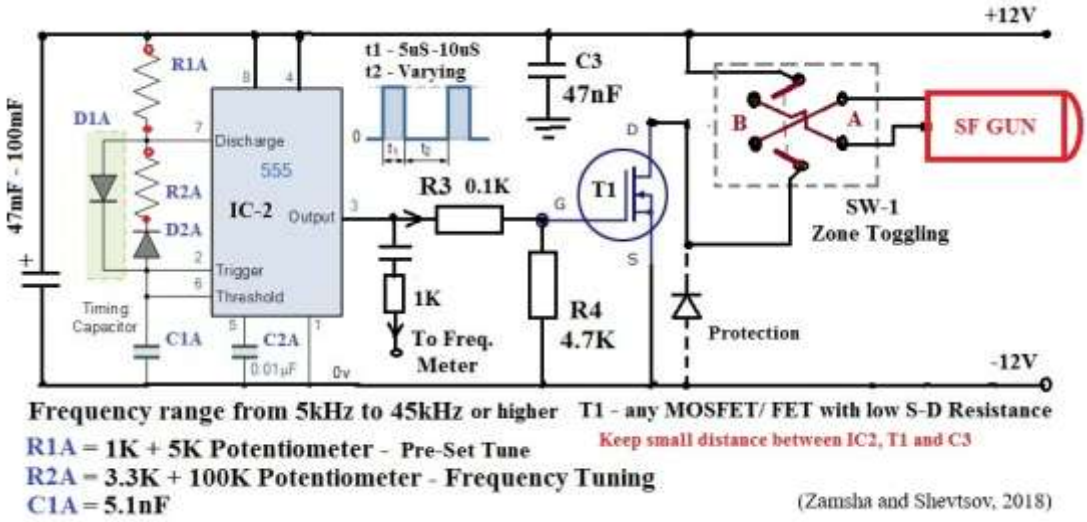

Fig. 15. The full schematic diagram of the magnetic scalar field gun.

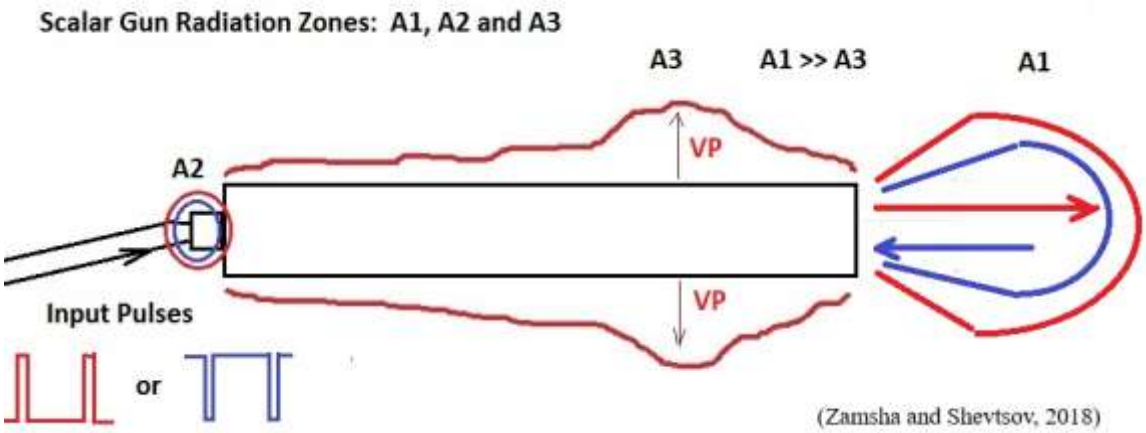

Fig. 16. The diagram of the emissions' distribution around the scalar field gun.

Some observations how the scalar field gun works

When the palm of the hand approaches to the front of the working scalar gun, the operator can feel some "warmth" in the center of the palm or "chill" if the polarity of the pulses fed into the scalar gun is reversed. So, we can feel a negative or positive zone of the scalar field generator. Also, it was noted some “warmth” on the side of the cylinder at distance about 1/3 back from the gun's front. However, it not changed to “cold” state if the polarity of the pulses changed! So, from the scalar gun’s side we maybe have different emissions and it looks like a Poynting vector works in this situation. Figure 16 shows how the emissions spread around the scalar field gun.

Some electromagnetic emissions around the scalar field gun were also observed at a distance of by about 1 cm from its surface. However, the electromagnetic interference was below 0.1 Volt. So, this is the background level of the electromagnetic emission! Note that the surface of the scalar gun must not contact any conductive objects, except the rear connection port. Also, do not hold the cylinder of the working scalar gun with your hand!

Warning!

Please take precaution when use a big power scalar gun because its operation can harm your health!

CONCLUSION

The authors of this article developed a relatively “pure” magnetic scalar field generator (scalar gun) based on the scalar field theory developed by Nikolaev and Tomilin. Of course, the developed device needs further optimization for different uses. However, the authors advise to start with a big device such as the scalar gun because it works on relatively low frequencies. So, it is easy to tune it and operate. The shape of the outer cylinder can be different, for instance, it can be as sphere. The proposed devise can be employed as a magnetic scalar field generator for some researches in biology, medicine, physics, or as a part of new communication systems, including the ones discussed in (Shkatov and Zamsha, 2015; Zakharenko, 2018, 2020).

REFERENCES

Nikolaev, GV. 1997. Trouble-Free Electrodynamics. Theory, Experiments, Paradoxes. Book 1. Scientific-Technical Literature Publishers, Tomsk Polytechnical University, Tomsk, Russia, pp.144. (In Russian) ISBN: 5-89503-014-9.

Shkatov, V. and Zamsha, V. 2015. Torsion Field and Interstellar Communication. Easy Print, China. pp. 30. http://www.iga1.ru/pribor/TorsionField.pdf

Tomilin, AK. 2009. The Fundamentals of Generalized Electrodynamics. East-Kazakhstan State Technical University, Ust-Kamenogorsk, Kazakhstan. pp. 129. (In Russian but a part is in English here https://arxiv.org/pdf/0807.2172v1.pdf).

Zakharenko, AA. 2018. On necessity of development of instant interplanetary telecommunication based on some gravitational phenomena for remote medical diagnostics and treatment. Canadian Journal of Pure and Applied Sciences. 12(2):4481-4487. DOI: https://doi.org/10.5281/zenodo.1301289.

Zakharenko, AA. 2020. On evaluations of fast speeds of propagation of gravitational phenomena: A review. Canadian Journal of Pure and Applied Sciences. 14(1):4947-4963. DOI: http://doi.org/10.5281/ zenodo. 3688779.

Received: Final Revised: June 30, 2021;
Accepted: August 26, 2021

Canadian Journal of Pure and Applied Sciences
Vol. 15, No. 3, pp. 5323-5332, Oct 2021
Online ISSN: 1920-3853; Print ISSN: 1715-9997
Available online at www.cjpas.net

UNDERSTANDING THE PLANCK CONSTANT AND THE BEHAVIOUR OF PHOTON PARTICLES FROM A MECHANICAL PERSPECTIVE

Wenzhong David Zhang
Hembury Avenue, Manchester, M19 1FH, UK

ABSTRACT

The Planck constant is derived from the analysing of the energy and frequency relationship of a simple harmonic oscillator model for photon particles from a mechanical perspective. The correlation between the Planck constant, the inertial mass, the angular frequency, and the corresponding radius of the harmonic oscillation of the photon particle is derived. The photon particles have equal mechanical angular momentum. This insight is applied to the propagation of photon particles in the free space and other transparent media based on the model of the cycloid motion of harmonic oscillators. The interdependence of the properties of photon particles and their entanglements with their surrounding spaces are elicited. Kepler's second and third laws of motion are deduced for the specified photon particle in the free space and other transparent media. For any particle in periodic motion with the rotational symmetry, its inertial mass, its time period, and its space displacement are entangled together by its conserved mechanical angular momentum. The centre of the periodic motion with the rotational symmetry is proposed as a universally applicable reference frame to simplify and unify the laws of physics. The generalized Planck constant, generalized Planck-Einstein relation, and generalized de Broglie relation are proposed for applications in both microcosms and macrocosms.

Keywords: Planck constant, mechanical angular momentum, cycloid motion, generalized Planck constant, generalized Planck-Einstein relation, generalized de Broglie relation.

INTRODUCTION

The Planck constant is the pillar of modern quantum physics. The Planck constant has profound ramifications in three important areas: our technology, our understanding of reality, and our understanding of life (Stein, 2011. Planck's constant: The number that rules technology, reality, and life. http://www.pbs.org/wgbh/nova/blogs/physics/2011/10/plancks-constant). The Planck constant h entered physics in the beginning of the 20th century as the result of Max Planck's attempts to provide a theoretical explanation for the empirically discovered laws of thermal blackbody radiation (Planck, 1901; Planck, 1900). He found that the experimental observations of thermal blackbody radiation spectrum can be speculated in perfect agreement, if one adopted the concept that matter was a collection of discrete harmonic oscillators (Oldershaw, 2013) emitting electromagnetic radiation in packages (energy quanta) that obeyed an energy (E) / frequency (f) law of the following form:

$$E = hf \tag{1}$$

One of the earliest applications of the Planck constant was by Einstein to explain some aspects of Wien's law for blackbody radiation and to account for the photoelectric effect (Einstein, 1905). Einstein introduced the idea of a photon particle with energy related to its frequency as $E = hf$ called the Planck-Einstein relation. The establishment of the Planck-Einstein relation is generally regarded as the starting point of quantum physics. The Planck constanthas become one of the most essential universal constants. However, the physical origin and nature of the Planck constant have not been fully understood. Investigating the physical origin and nature of the Planck constant is not only important for advancing our understanding on the foundation of modern quantum physics for microcosms, it is also relevant to the current study of cosmology (Chang, 2017). Stellar Planck constant has been proposed to describe the characteristic quantities of angular momentum and action inherent in the objects of the stellar level of matter (Fedosin, 2015; Fedosin, 2014). Basically, every aspect of nature is associated with quantum phenomena involving the Planck constant. Understanding the physical origin and nature of the Planck constant may open the door to unify the physical laws of the microcosm and the macrocosm, the classical and the quantum.

The Planck constant is linked with periodic motion with rotational symmetry. In order to get a better insight into the physical origin and the nature of the Planck constant, an approach is discovered to derive the Planck constant through the analysing of the energy and frequency

Corresponding author e-mail: WenzhongZhang2008@gmail.com

relationship of a simple harmonic oscillator model for a photon particle from a mechanical perspective. The gained insight into the physical origin and the nature of the Planck constant is both applicable and powerful in elucidating the property of photon particles in the free space (vacuum) and other transparent media. All photon particles have an equal mechanical angular momentum $\hbar$. The interdependence of the properties of photon particles and their entanglements with their surrounding spaces are elicited. The inertial mass of any particle in periodic motion with rotational symmetry should not be equal to zero. Any particle in periodic motion with rotational symmetry, its inertial mass, its time period, and its space displacement are entangled together with its conserved mechanical angular momentum.

The exploration of the physical origin and the nature of the Planck constant from a mechanical perspective

The exploration begins from analysing the energy and frequency relationship of a simple harmonic oscillator with rotational symmetry as shown schematically in Figure 1. For harmonic oscillation to occur, the system must possess the following two quantities: elasticity and inertia. The simplest example of a harmonic oscillating system is a mass connected to a rigid foundation by way of a spring. At this stage, we assume that the spring is undamped and massless under ideal approximation. However, a nonzero spring mass or damped spring can be easily accommodated under some simplifying assumptions and can be developed further for the more accurate understanding of reality (Garret, 2017; Zhang, 2021a; Zhang, 2021b). The elasticity of the spring k (spring constant) provides the elastic restoring force that enables the system to return to its equilibrium when the system is displaced from its equilibrium position. The inertia of the mass m (inertial mass) provides the overshoot that warrants the system to pass the equilibrium position. The natural angular frequency of the oscillation ω is related to the elastic and inertia properties of the system.

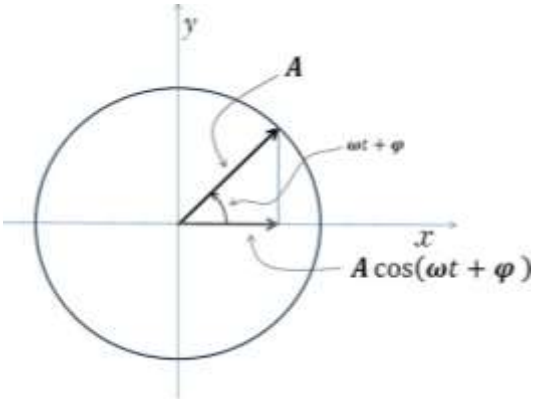

Fig. 1. The corresponding harmonic circular motion of the simple harmonic oscillator.

By applying Newton's second law $F = ma$ and Hooke's law $F = -kx$, the equation of motion for the simple mass-spring harmonic oscillating system is obtained as follows:

$$ma = -kx \rightarrow m\frac{d^2x}{dt^2} + kx = 0 \rightarrow$$

$$\frac{d^2x}{dt^2} + \frac{k}{m}x = 0 \rightarrow \frac{d^2x}{dt^2} + \omega^2 x = 0$$

where ω is the natural angular frequency of the oscillation, i.e.

$$\omega = \sqrt{elasticity/inertia} = \sqrt{k/m} \quad (2)$$

The solution to the equation of motion takes the following form:

$$x(t) = A\cos(\omega t + \varphi)$$

where A is the amplitude of the oscillationor the corresponding radius of the harmonic circular motion and φ is the phase constant. Both the constants A and φ are determined by the initial condition at a chosen time of $t = 0$ under the ideal approximation that the spring is undamped and massless. Figure 1 shows schematically the corresponding harmonic circular motion of the simple harmonic oscillator. The period T (the time to complete one corresponding circle), the frequency f, and the angular frequency ω of the oscillating are defined as follows:

$$T = 1/f \text{ and } \omega = 2\pi f = \frac{2\pi}{T} \quad (3)$$

As the system oscillates, the total energy E of the system remains constant and time-independent, and depends only on the elasticity parameter k and the maximum displacement A (or the mass m and the maximum magnitude of velocity $V_m = \omega A$), i.e.

$$E = \frac{1}{2}kx^2 + \frac{1}{2}mV^2 = \quad (4)$$

$$\frac{1}{2}kA^2cos^2(\omega t + \varphi) + \frac{1}{2}m\omega^2A^2sin^2(\omega t + \varphi)$$

$$= \frac{1}{2}kA^2 = \frac{1}{2}mV_m^2 = \frac{1}{2}m\omega^2A^2$$

where V is the magnitude of velocity (speed) of the point of the mass m. For the corresponding harmonic circular motion as shown schematically in Figure 1, one can write down that

$$V = A\omega \quad (5)$$

Differentiation of the total energy $E = \frac{1}{2}m\omega^2A^2$ in equation (4) with respect to the angular frequency ω generates the following expression:

$$\frac{dE}{d\omega} = mA^2\omega = A^2\sqrt{km} \quad (6)$$

Hence,

$$\Delta E = A^2\sqrt{km}\,\Delta\omega = 2\pi A^2\sqrt{km}\,\Delta f \quad (7)$$

Comparing equation (7) with equation (1), the Planck constant *h* for the photon particle at the reference frame of constant linear light velocity can be derived as follows:

$$h = 2\pi A^2\sqrt{km} (\text{or } \hbar = A^2\sqrt{km}) \quad (8)$$

where A is the radius of the harmonic circular motion, k is the elasticity parameter of the space, m is the equivalent inertial mass of the photon particle and $\hbar$ is the reduced Planck constant or Dirac's constant, $\hbar = h/2\pi$. Incorporating equation (2), (5), and (8), especially for the harmonic circular motion of the photon particle at the reference frame of constant linear light velocity, it is derived that

$$\hbar = A^2\sqrt{km} = m\omega A^2 = mVA \quad (9)$$

where *V* is the average of the magnitude of velocity (speed) of the photon that represents the constant speed *c* in the free space (vacuum) and the constant *V* in other transparent homogeneous media. While mVA is the mechanical angular momentum of the harmonic circular motion of photon particles. Hence, the reduced Planck constant $\hbar$ is the mechanical angular momentum of the harmonic circular motion of photon particles.

It is worth to point out that the mechanical angular momentum of photon particles from a mechanical perspective is different to the optical angular momentum of the corresponding photon waves from an electromagnetic perspective (Bliokh and Nori, 2015), although they have interdependence. The conservation of mechanical angular momentum is fundamentally associated with periodic motions of the rotational symmetry and can be calculated using Noether's theorem (Bliokh and Nori, 2015). For the photon particles, equations (1), (8), and (9) disclose the correlation and interdependence of $E, f, m, k, V, \omega, A,$and $\hbar$. Physical science is all about the correlation of physical quantities. If we take h ($\hbar$) and the velocity of photon $V = c$ in the free space (vacuum) as some universal constants, then the *m* (equivalent inertial mass), the ω (time period) and the *A* (space displacement) of the photon particles are entangled together with the constant mechanical angular momentum $\hbar$.

From equation (9), it also can be seen that the reduced Planck constant $\hbar$ is a constant determined by the interacting of the photon particle and its surrounding space. If a simple dissipative element as a viscous damper was added to the simple harmonic oscillator model to take into account the weak friction force of the free space, it is derived theoretically that the energy and the inertial mass of the photon particle can decrease slowly, its corresponding radius of harmonic circular motion increases slowly (red-shift), its mechanical angular momentum is kept as a constant according to equation (9) (Zhang, 2021a; Zhang, 2021b). The harmonic oscillator model of photon particles also paves the way for a possible explanation that the energies and the inertial mass of photon oscillators can be increased under driving forces and works, meanwhile, their corresponding radii are decreased (blue shift) according to equation (9). A driving and dampening harmonic oscillator model may be further developed to explain the production of high energy photons, electron-positron pairs, and other elementary particles.

Conservation of mechanical angular momentum in macrocosms is well-known as Kepler's second law or Kepler's equal area law. In microcosms, it is well-known as the quantization of angular momentum, which was initially proposed as one of Bohr's key hypotheses in the Bohr model of hydrogen. The mechanical angular momentum is a conservative quantity in both microcosms and macrocosms for periodic motions with rotational symmetry, although the real trajectories of particles in microcosms are quite different with the trajectories of particles in macrocosms. The trajectories of particles in microcosms are blurred to clouds in approximately round shapes by transient energy fluctuations. It is unveiled that the quantization of mechanical angular momentum in quantum mechanics and Kepler's second law in astronomy arise from the same fundamental law of the conservation of mechanical angular momentum for periodic motions with rotational symmetry. For a particle in periodic motion with rotational symmetry, its mechanical angular momentum is a constant and can never be equal to zero. Therefore, its energy forms into quantum (discrete energy) in the frequency domain according to equation (7). The Planck-Einstein relation can be generalized for any particle in the periodic motion with rotational symmetry as follows:

$$E = H_A\,\omega \quad (10)$$

$$H_A = A^2\sqrt{km} = m\omega A^2 = mVA \quad (11)$$

where *E* is the energy of the particle in periodic motion with the rotational symmetry, ω is the angular frequency of the particle, H_A is the conserved mechanical angular momentum. H_A may be named as the generalized Planck constant. The particle can be a photon particle, an elementary particle, an atom, a planet, a star, or a galaxy. It shall be emphasized that from equation (7) to equations (1) and (10), a zero-energy point is assigned while the

frequency of the periodic motion is equal to zero. If the frequency is equal to zero, the motion shall be a motion along an absolute straight line without spinning or oscillation. This kind of motion may not exist in the Universe. The typical motions at elementary particle scale, atomic scale, stellar scale, and galactic scale are periodic motions with the rotational symmetry. Hence, the conservation of mechanical angular momentum is fundamental in both microcosms and macrocosms. All particles in periodic motion with the rotational symmetry in both microcosms and macrocosms, their inertial masses, their time periods, and their space displacements are entangled together through their conserved mechanical angular momentums. Einstein's general relativity is a kind of beautiful and abstractive mathematical description of the physical world famously depicted as: Matter tells space-time how to curve; space-time tells matter how to move (Wheeler and Ford, 1998, 2000) that indicates the entanglement of matter, space, and time. However, it does not reveal the fundamental nature of the physical world, why and how? Now it is uncovered that the fundamental nature of the physical world is the entanglement of the inertial mass, the time period, and the space displacement of the particle in periodic motion with the rotational symmetry, which arises from the fundamental law of the conservation of mechanical angular momentum for motions with rotational symmetry. Within the three parameters of inertial mass, time period, and space displacement of a particle in periodic motion with rotational symmetry, only two parameters are independent.

Although the Planck constant is derived from analysing the energy and frequency relationship of the simple harmonic oscillator, it is applicable and powerful in elucidating the property and propagation of photon particles in both the free space (vacuum) and other transparent media, which will be illustrated in the following sections. It will be shown that Kepler's third law (the Period law) can be derived for a specified photon particle based on the new insight into the physical nature and the physical origin of the Planck constant.

The property and propagation of photon particles in the free space (vacuum)

It is proved experimentally that the velocity of photons in the free space is the constant speed *c* over a wide range of frequencies, the relation between energy E and momentum p of a propagating single frequency photon particle is $E = pc$ (Nelson and Kinder, 2017). The propagation of the single frequency photon particle in the free space can be treated as the cycloid motion of a harmonic oscillator from a mechanical perspective shown schematically in Figure 2. This model of the cycloid motion of the harmonic oscillator for the single frequency photon particle illustrates vividly the Wave Particle Durability of a photon and it can greatly assist in the derivation of correlations between the properties of photons. In the period T (one cycle, $\theta = 2\pi$), the single frequency photon particle rolls the wavelength λ, which equals to one circumference $2\pi R = 2\pi A$ as shown in Figures 1 and 2, where

$$\lambda = 2\pi A \tag{12}$$

In the free space, it is experimentally approved that

$$\lambda/T = c \tag{13}$$

From equations (2), (3), (8), (12), and (13), it can be derived that

$$m = h/c\lambda = \hbar\omega/c^2 \tag{14}$$

$$k = 4\pi^2 hc/\lambda^3 \tag{15}$$

Incorporating equations (1), (2), (3), and (14), it is obtained that

$$E = hf = \hbar\omega = hc/\lambda = mc^2 \tag{16}$$

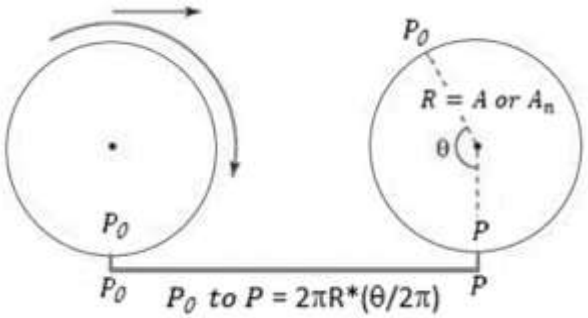

Fig. 2. The schematic diagram showing the cycloid motion model for a photon particle.

The derived equality $E = mc^2$ is the Einstein mass-energy equation. However, the mass of the single frequency photon particle in equation (16) shall be the inertial mass of the single frequency photon particle from a mechanical perspective. In this article, for the mass of the single frequency photon particle, it is called either equivalent mass or inertial mass to distinguish it with the rest mass in Einstein's special relativity. The single frequency photon particle will be simply called the photon particle below.

Based on equation (16), the momentum of the photon particle can be deduced as follows:

$$p = E/c = mc = h/\lambda \tag{17}$$

where $p = h/\lambda$ is the de Broglie relation. From equations (3), (16), and (17), for the photon particle within one period of T or one wavelength of λ, it can be derived that

$$ET = h \tag{18}$$

$$p\lambda = mc\lambda = h \tag{19}$$

Fascinatingly, for the specified photon particle with the fixed frequency or wavelength, Kepler's third law (the Period law) can be derived from equations (2), (3), and (15) as follows:

$$T^2 = 4\pi^2 m\, A^3/\hbar c = K_{kep}\, A^3 \tag{20}$$

where K_{kep} is Kepler's constant for the specified photon particle in periodic motion in the free space. It is defined by

$$K_{kep} = 4\pi^2 m/\hbar c \tag{21}$$

Equations (20) and (21) disclose the correlation of $T, A, c, m, \hbar,$ and K_{kep} for the photon particles in periodic motions in the free space. Kepler's laws of motion are applicable in both microcosms and macrocosms. If we substitute equation (14) into equation (20), it can be derived that

$$T^2 = 4\pi^2 A^2/c^2 \tag{22}$$

How could equations (20) and (22) be both true? The answer lies in the conserved mechanical angular momentum of the cycloid motion of photon particles in the free space, $m/\hbar = 1/(cA)$ for the specified photon particle. It may be easier to be understood from another point of view, equation (22) is true for any photon particle in any inertial reference frame at some constant speed in the free space. Equation (20) is only true for an imagined observer at the centre of the harmonic motion of the photon particle. This is an imagined inertial reference frame at constant linear light velocity moving together with the rotation centre of the photon particle. Because of the cycloid motion of photon particles, if we accept $\lambda = 2\pi A$, the measured parameters T, c, λ and the calculated parameter A in any inertial reference frame agree with each other. Similar to K_{kep}, the inertial mass m of the photon particle shall be the inertial mass in the imagined reference frame at constant linear light velocity moving together with the rotation centre of the specified photon particle. According to equation (14), the photon particle has the mass equivalent to the inertial mass of the photon particle in the imaged reference frame at constant linear light velocity from a mechanical perspective, which can be calculated as $m = h/(c\lambda) = 2.21021906 \times 10^{-42}\ (1/\lambda)$. From the imagined reference frame at constant linear light velocity moving together with a stream of photon particles to a laboratory reference frame on earth or in a satellite, the inertial masses of photon particles cannot be transferred to a zero inertial mass because the zero inertial mass cannot be transferred back to a range of inertial masses. Hence, the inertial masses of photon particles in a laboratory reference frame on the Earth or inside a satellite cannot be equal to zero. From a theoretical perspective, a finite inertial mass for the photon particle will lead to Proca's Lagrangian and Yukawa potential (Proca, 1936; Tu *et al*., 2005; Caccavano and Leung, 2013; Nyambuya, 2014), which is perfectly compatible with the general principles of elementary particle physics, which may lead to unified physics laws. Maxwell's Equations and Coulomb's Law with great successes in science and engineering are based on the ideal assumptions of massless photon and the frictionless free space, i.e. a vacuum. They are ideal approximations of physical realities, which are brilliant enough for the scale of size of the Earth-Moon system.

However, on a cosmic scale such as the Milky Way Galaxy and above, modifications are needed (Zhang, 2021a; Zhang, 2021b). Einstein's theories of relativity sprang out of Maxwell's equations. Hence, the ideal approximations of the massless photon and the frictionless free space were inherited. Modern cosmology theories originated from Einstein's relativities have met difficulties and challenges (Zhang, 2021a; Zhang, 2021b; Potter, 2009; Traunmüller, 2017). It is well-known that it is extremely difficult to reconcile Einstein's relativities with quantum mechanics. The quantitative understanding of the inertial masses and the entanglement of inertial masses, time periods, and space displacements of particles in periodic motion with rotational symmetry from a universally applicable reference frame may help to resolve the difficulties and challenges. The reference frame of the centre of the periodic motion with rotational symmetry can be a universally applicable reference frame, which may simplify and unify the laws of physics.

Let us now focus back on the photon particles travelling in the transparent media with refractive indices. Interestingly, the inertial mass of the photon particle in a transparent medium can have a sizable increase in comparison with the one in the free space (vacuum) that will be elucidated in the following section.

The property and propagation of photon particles in transparent media with refractive indices

In the early 20th century, two possible candidates for the momentum of a photon propagating through a transparent medium emerged. One was proposed by Hermann Minkowski (1908) that the photon's momentum was given by $p_n = n\hbar\omega/c$. A year later, Max Abraham (1909) came up with a different expression for the photon's momentum: $p_n = \hbar\omega/nc$. This controversy is known as the Abraham-Minkowski dilemma(Partanen *et al*., 2017).

These rivalling momenta differ by n^2, which is a sizeable factor in most media: in water, *n* is approximately 1.33 and in glass *n* is ~ 1.46 (Leonhardt, 2006). Over the years, physicists have found supporting evidences, from both first-principles arguments and experiments, for each expression in different contexts, some of them have even proposed ways that the apparent paradox might be resolved (Partanen *et al.*, 2017; Leonhardt, 2006; Cho, 2010; Barnett, 2010; Sheppard and Kemp, 2016; Kemp, 2011; Brevik, 1979; Brevik, 2017; Testa, 2013; Crenshaw, 2013). Through computer simulations, Partanen *et al.* (2017) claimed that they proved the transfer of mass with the light pulse representing the photon mass drag effect. The photon mass drag effect gives an essential contribution to the total momentum of the light pulse, which becomes equal to Minkowski's momentum. It is claimed that the Minkowski momentum is the total momentum of the system, the Abraham momentum is the portion of the momentum carried by the light field, and the difference between the two is carried by the atomic mass density wave. The claimed experiments have only been taken in computer simulations so far. Due to the coupling of the field and matter, Abraham's momentum is unable to be measured directly, only the total momentum of the light pulse (Minkowski's momentum) can be directly measured.

The behaviour of photon particles in the transparent media with refractive indices can be elucidated in a simple and clear way based on the new insight into the physical origin and nature of the Planck constant. Subtly, some materials are transparent at least to some kinds of light. For example, water and glass are transparent to visible light, air is transparent to a wide range of frequencies of light. When a stream of photon particles travels from the free space (vacuum) to a transparent medium and travels through it with negligible energy absorption, their energies and frequenciescan be viewed as no change. However, the elastic interactions with electrons inside the medium do have the net effect of slowing the photons down (Nelson and Kinder, 2017). The velocity of the photon in the transparent medium is c/n, where c is the velocity of photons in the free space, n is the medium's refractive index, a dimensionless number larger than 1. More precisely, the index depends on the frequency f, so the relation can be better written as c/n_f (Nelson and Kinder, 2017). As now we focus theoretically on monochromatic light with single frequency photon particles, n instead of n_f will be used for simplicity.

Let's recall the model of cycloid motion for photon particles, as schematically shown in Figure 2. In the period T, the photon particle rolls the wavelength λ_n in the medium with the refractive index n. The wavelength λ_n equals to one circumference $2\pi A_n$, where A_n is the amplitude of the harmonic motion in the transparent medium with the refractive index n, the radius of the corresponding harmonic circular motion $R = A_n$. Hence,

$$\lambda_n = 2\pi A_n \tag{23}$$

$$\lambda_n/T = \lambda_n f = V = c/n \tag{24}$$

$$\omega = 2\pi f = \sqrt{elasticity/inertia} = \sqrt{k_n/m_n} \tag{25}$$

where k_n is the elasticity of the medium, m_n is the inertial mass of the photon particle in the transparent medium. The Planck constant is still a constant from the free space to the transparent medium as the mechanical angular momentum of the photon is conservative based on Noether's theorem, i.e.

$$h = 2\pi A^2\sqrt{km} = 2\pi A_n^2\sqrt{k_n m_n} \tag{26}$$

$$\hbar = m\omega A^2 = mcA = m_n\omega A_n^2 = m_n V A_n \tag{27}$$

From equations (23)-(26), it can be derived that

$$m_n = h/V\,\lambda_n \tag{28}$$

$$k_n = 4\pi^2 hV/\lambda_n^3 \tag{29}$$

Incorporating equations (1), (24) and (28), it is obtained that

$$E = \hbar\omega = hf = hV/\lambda_n = m_n V^2 \tag{30}$$

Based on equation (30), the momentum of the photon particle can be deduced as follows:

$$p_n = m_n V = h/\lambda_n = nE/c = n\hbar\omega/c \tag{31}$$

where $p_n = h/\lambda_n$ is the de Broglie relation. From equations (30) and (31) for the photon particle within one period of T or one wavelength of λ_n of its periodic motion, it is derived as follows:

$$ET = h \tag{32}$$

$$p_n\lambda_n = m_n V\,\lambda_n = h \tag{33}$$

Equations (32) and (33) may be generalized for all particles in periodic motion with the rotational symmetry, i.e.

$$ET = 2\pi H_A \tag{34}$$

$$p\lambda = mV\lambda = 2\pi H_A \tag{35}$$

where H_A is the mechanical angular momentum of the particle in periodic motion with rotational symmetry. $E, p, \lambda, m,$ and V are subsequently the energy, momentum, wavelength, inertial mass, and the velocity of the particle

in periodic motion with rotational symmetry. Equation (35) may be named generalized de Broglie relation. Equation (34) is essentially another form of equation (10).

It is interesting to notice that the inertial mass of the single frequency photon particle in the medium (m_n) increased in comparison with the one in the free space (m):

$$m_n = h/V\,\lambda_n = n^2(h/c\lambda) = n^2\frac{\hbar\omega}{C^2} = n^2 m \tag{36}$$

where λ is the wavelength of the photon in the free space (vacuum). Partanen *et al*. (2017) showed that with the light pulse in a medium, the mass transfer equals to $(n^2-1)\frac{\hbar\omega}{c^2}$ with an assumption that the inertial mass of the photon particle in the free space equals to zero. Our calculations show that the inertial mass of the photon particle in the free space is $\frac{\hbar\omega}{c^2}$ and the inertial mass of the photon particle in the transparent medium equals to $n^2\frac{\hbar\omega}{c^2}$. The increase of inertial mass from the free space to the transparent medium is $(n^2-1)\frac{\hbar\omega}{c^2}$. The results from equations (23) to (36) imply that there are interdependences of the property of photon particles, and the property of photon particles is also entangled with their surrounding spaces in the transparent media. Their surrounding spaces can be different in the processes of emitting, propagation, and the measurement of the photon particles.

It is fascinating to notice from equations (31) that the de Broglie relation is kept the same form in the transparent medium as in the free space. According to equations (24) and (36), the inertial mass of the photon particle in the transparent medium is $m_n = n^2 m$, the photon particle gains the inertial mass while it slows down. The square of the velocity of the photon particle in the transparent medium is $V^2 = \frac{c^2}{n^2}$, hence, $E = m_n V^2 = mc^2$, the energy is conservative. It can be seen also that from the free space (vacuum) to the other transparent medium, the frequency of the photon is kept the same and the Planck constant is no change, thus the laws of conservation of both energy and angular momentum are obeyed. The conservation of energy arises from the negligible energy dissipation (under the ideal approximation) in both the free space and the transparent medium. The conservation of optical angular momentum is associated with the rotational symmetry and can be calculated using Noether's theorem. Amazingly, Kepler's third law can be elicited from equations (23), (24), (25), and (29) as follows:

$$T^2 = 4\pi^2 m_n A_n^3/\hbar V = K_{kep}\,A_n^3 \tag{37}$$

where K_{kep} is Kepler's constant for the specified photon particle with the inertial mass m_n in the transparent medium, namely

$$K_{kep} = 4\pi^2 m_n/\hbar V = 4\pi^2 n\, m_n/\hbar c \tag{38}$$

Equations (37) and (38) disclose the correlation or entanglement of $T, A_n, V, m_n, \hbar$, and K_{kep} for the photon particles in the transparent medium. The entanglement of the photon particles with their surrounding spaces is elicited. According to the derived equation (31), the photon particle's momentum calculated from the cycloid motion model agrees with Minkowski's prediction $p_n = n\hbar\omega/c$. The Snell law of refraction may be re-analysed and clarified as a piece of supportive experimental evidence. The refraction of light in transparent media obeys Snell's law as shown schematically in Figure 3. The angles of incidence (θ) and refraction (ϕ) at an interface are inversely proportional to the respective indices of refraction n_1 and n_2, which are characteristics for each medium:

$$n_1\sin(\theta) = n_2\sin(\phi) \tag{39}$$

The bending of light rays is regarded as the evidence for the existence of a force acting at the interface between the two media. The resultant force acting on the light is managed in the direction normal to the interface (Buenker and Muiño, 2004). Because of Newton's second law, the component of the momentum of the photons, which is parallel to the interface, shall be constant (Fig. 3). Thus, one can write that

$$p_1\sin(\theta) = p_2\sin(\phi) \tag{40}$$

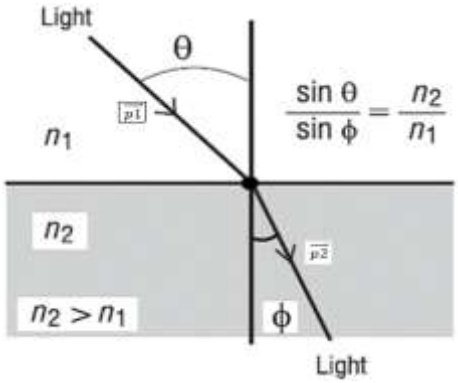

Fig. 3. The schematic diagram showing the refraction of light at an interface between two transparent media.

Comparing equation (40) with equation (39), it can be deduced that the total momentum of the photon particle is always proportional to the refractive index n of the given medium. Assume that medium 1 represents the free space, i.e. a vacuum. Hence, we have n_1 = 1. Since the light is bent toward the normal in transparent medium 2

$(n_2 > n_1 = 1)$, we are led to the conclusion that the momentum of the photon particle is greater in transparent medium 2 in comparison with the one in the free space (medium 1), i.e.

$$p_2 = (n_2/n_1)\, p_1 = n_2 p_1 = n_2\, \hbar\omega/c \qquad (41)$$

Hence, Snell's law of refraction supports the derived photon particle's momentum $p_n = n\hbar\omega/c$ that agrees with Minkowski's prediction. The Snell law of refraction can be viewed as a strong supportive experimental evidence of the cycloid motion model of photon particles (Padyala, 2019).

It is not by chance that the mechanical model of the cycloid motion of harmonic oscillator is able to illustrate vividly the wave-particle durability of photons and it is powerful in assisting the discovering of the interdependence and entanglement of the properties of photons in both the free space and other transparent media. The mechanical model must be linked with the physical reality of photon waves of the oscillating electric and magnetic fields from an electromagnetic perspective. Further research is needed to reveal the links in details.

CONCLUSION

The Planck constant is the pillar of modern physics. However, the physical origin and nature of the Planck constant have not been fully understood. In this article, the Planck constant was derived through analysing the energy and frequency relationship of the simple harmonic oscillator model for the photon particle from a mechanical perspective. It was derived that $h = 2\pi A^2\sqrt{km}$ and $\hbar = A^2\sqrt{km} = m\omega A^2 = mVA$. All single photon particles travelling in both the free space and other homogeneous transparent media have equal mechanical angular momentum $\hbar$ because they are in motion with identical rotational symmetry. These discoveries are applied to the propagation of photon particles in the free space by viewing the propagation of the photon particle as the cycloid motion of the harmonic oscillator. Amazingly, the Einstein mass-energy equation and the de Broglie relation are deduced subsequently. It is also elicited that the single frequency photon particle has an inertial mass in the free space such as $m = h/c\lambda = \hbar\omega/c^2$. It is further unveiled that the quantization of mechanical angular momentum in quantum mechanics and Kepler's second law (the equal area law in astronomy) arises from the same fundamental law of the conservation of mechanical angular momentum. Kepler's third law of motion (the Period law) is derived for the specified photon particle in both the free space and other homogeneous transparent media. From a widely applicable point of view, all particles in periodic motions with the rotational symmetry, their inertial masses, their time periods, and their space displacements are entangled together by their conserved mechanical angular momentums. These discoveries indicate the opening of the door to unify the physical laws of the microcosm and the macrocosm, the classical and the quantum. The reference frame of the centre of the periodic motion with the rotational symmetry is proposed as a universally applicable reference frame to simply and unify the laws of physics.

Applying the discoveries to the propagation of photon particles in the transparent medium with a refractive index, it is deduced that the de Broglie relation is kept the same form as in the free space. However, the equation for the energy of the single frequency photon particle transformed from $E = mc^2$ to $E = m_n V^2$, while its energy and mechanical angular momentum are both conservative. The Abraham-Minkowski dilemma was briefly reviewed. The derived momentum of the single frequency photon particle based on the new method agrees with Minkowski's prediction as most of experimental observations do. Snell's law of refraction was re-analysed and clarified as another piece of supportive experimental evidence to Minkowski's prediction. Snell's law of refraction is an important supportive evidence of the cycloid motion model of photon particles.

The new insight into the physical nature and origin of the generalized Planck constant, the generalized Planck-Einstein relation, and the generalized de Broglie relation can be equally applicable to atomic-scale systems, stellar scale systems, and galactic scale systems. Further research is needed to reveal the links between the cycloid motion of photon particles and the oscillating electric and magnetic fields of their corresponding electromagnetic waves.

ACKNOWLEDGEMENT

The author gratefully acknowledges the encouragements and supports from my family, friends, and colleagues-researchers to these theoretical investigations.

REFERENCES

Abraham, M. 1909. Zur Elektrodynamik bewegter Körper. Rendiconti del Circolo Matematico di Palermo. 28:1-28.

Abraham, M. 1910. Sull'elettrodinamica di Minkowski. Rendiconti del Circolo Matematico di Palermo. 30:33-46.

Barnett, SM. 2010. Resolution of the Abraham-Minkowski dilemma. Physical Review Letters. 104(7):07040. DOI: https://doi.org/10.1103/ PhysRevLett. 104.070401.

Bliokh, KY. and Nori, F. 2015. Transverse and longitudinal angular momenta of light. Physics Reports. 592:1-38. DOI: https://doi.org/10.1016/ j.physrep. 2015.06.003.

Brevik, I. 1979. Experiments in phenomenological electrodynamics and the electromagnetic energy-momentum tensor. Physics Reports. 52(3):133-201.

Brevik, I. 2017. Minkowski momentum resulting from a vacuum-medium mapping procedure and a brief review of Minkowski momentum experiments. Annals of Physics. 377:10-21.DOI: https://doi.org/10.1016/j.aop. 2017.01. 009.

Buenker, RJ. and Muiño, PL. 2004. Quantum mechanical relations for the energy, momentum and velocity of single photons in dispersive media. Khimicheskaya Fizika (Moscow, Russia). 23(2):110-115. Pre-print at https://arxiv.org/pdf/physics/0607094.

Caccavano, A. and Leung, PT. 2013. Atomic spectroscopy and the photon mass: Effects on the 21 cm radiation. Physics Letters A. 377(39):2777-2779.DOI: https://doi.org/10.1016/j.physleta.2013.08.011.

Chang, DC. 2017. Physical interpretation of Planck's constant based on the Maxwell theory. Chinese Physics B. 26(4):040301. DOI: https://doi.org/10.1088/1674-1056/ 26/4/040301.

Cho, A. 2010. Century-long debate over momentum of light resolved? Science. 327(5969):1067. DOI: https://doi.org/10.1126/science.327.5969.1067.

Crenshaw, ME. 2013. Decomposition of the total momentum in a linear dielectric into field and matter components. Annals of Physics. 338:97-106. DOI: https://doi.org/10.1016/j.aop.2013.07.005.

Einstein, A. 1905. Concerning a heuristic point of view toward the emission and transformation of light. Annalen der Physik. 17:132-148.

Fedosin, SG. 2014. The Physical Theories and Infinite Hierarchical Nesting of Matter. LAP LAMBERT Academic Publishing. Volume 1. pp 580. ISBN-13:978-3-659-57301-9.

Fedosin, SG. 2015. The Physical Theories and Infinite Hierarchical Nesting of Matter. LAP LAMBERT Academic Publishing. Volume 2. pp. 420. ISBN-13: 978-3-659-71511-2.

Garret, SL. 2017. Understanding Acoustics. An Experimentalist's View of Acoustics and Vibration. Springer Series in Graduate Texts in Physics, Springer International Publishing. pp. 896. DOI: https://doi.org/10.1007/978-3-319-49978-9.

Kemp, BA. 2011. Resolution of the Abraham-Minkowski debate: Implications for the electromagnetic wave theory of light in matter. Journal of Applied Physics. 109(11):111101. DOI: https://doi.org/10.1063/1.3582151.

Leonhardt, U. 2006. Momentum in an uncertain light. Nature. 444(7121):823-824. DOI: https://doi.org/ 10.1038/444823a.

Minkowski, H. 1908. Die Grundgleichungen für die elektromagnetischen Vorgänge in bewegten Körpern. Nachrichten von der Gesellschaft der Wissenschaften zu Göttingen, Mathematisch-Physikalische Klasse, Weidmannsche Buchhandlung, Berlin, Deutschland. 1:53-111.

Nelson, P. and Kinder, JM. 2017. From Photon to Neuron: Light, Imaging, Vision. Princeton University Press, Princeton, USA. pp. 512.

Nyambuya, GG. 2014. Gauge invariant massive long range and long-lived photons. Journal of Modern Physics. 5(17):1902-1909. DOI: http://dx.doi.org/10.4236/jmp. 2014.517185.

Oldershaw, RL. 2013. The hidden meaning of Planck's constant. Universal Journal of Physics and Application. 1(2):88-92. DOI: http://dx.doi.org/ 10.13189/ ujpa.2013.010206.

Padyala, R. 2019. Brachistochrone – the path of quickest descent. Resonance – Journal of Science Education. 24(2):201-216. DOI: https://doi.org/10.1007/s12045-019-0771-y.

Partanen, M., Häyrynen, T., Oksanen, J. and Tulkki, J. 2017. Photon mass drag and the momentum of light in a medium. Physical Review A. 95(6):063850. DOI: https://doi.org/10.1103/PhysRevA.95.063850.

Planck, M. 1900. On an improvement of Wien's equation for the spectrum. Annalen der Physik. 1:719-721.

Planck, M. 1901. On the law of the energy distribution in the normal spectrum. Annalen der Physik. 4:553-570.

Potter, F. (edi.) 2009. The Second Crisis in Cosmology Conference, CCC-2. Astronomical Society of the Pacific Conference Series. Volume 413. ISBN: 978-1-58381-706-3.

Proca, A. 1936. Comptes Rendus (The Parisian Academy). 202:1420.

Sheppard, CJ. and Kemp, BA. 2016. Kinetic-energy momentum tensor in electrodynamics. Physical Review A. 93(1):013855. DOI: https://doi.org/10.1103/ PhysRevA.93.013855.

Testa, M. 2013. The momentum of an electromagnetic wave inside a dielectric. Annals of Physics. 336:1-11.

Traunmüller, H. 2018. Towards a more well-founded cosmology. Zeitschrift fur Naturforschung A (de

Gruyter). 73(11):1005-1023. DOI: https://doi.org/10.1515/zna-2018-0217.

Tu, LC., Luo, J. and Gillies, GT. 2005. The mass of the photon. Reports on Progress in Physics. 68(1):77-130.DOI:https://doi.org/10.1088/0034-4885/68/1/R02.

Wheeler, JA. and Ford, KW. 1998. Geons, Black Holes, and Quantum Foam: A Life in Physics. Norton and Company. pp. 380.

Wheeler, JA. and Ford, KW. 2000. Geons, black holes, and quantum foam: A life in physics. American Journal of Physics. 68(6):584. DOI: https://doi.org/10.1119/1.19497.

Zhang, WD. 2021[a]. The foundation of an emerged superphoton theory. Canadian Journal of Pure and Applied Sciences. 15(2):5221-5229.

Zhang, WD. 2021[b]. The Bose-Einstein condensation and the dynamic circulation of photons. Canadian Journal of Pure and Applied Sciences. 15(2):5247-5252.

Received: June 7, 2021; Accepted: August 20, 2021

Canadian Journal of Pure and Applied Sciences
Vol. 15, No. 3, pp. 5333-5340, Oct 2021
Online ISSN: 1920-3853; Print ISSN: 1715-9997
Available online at www.cjpas.net

THE SHAPE OF A PHOTON

Christopher C. O'Neill
University College Dublin (UCD), Belfield, Dublin, Ireland

ABSTRACT

This paper deals with partial confirmation of the shape of a photon via a new kind of mathematics, where imaginary numbers are privileged over real numbers when an absolute value is given, by the way of the XNOR logic gate. The research begins with polynomials and then progresses from a planar wave form to a final and more accurate radial wave form. This research study reveals the mechanism behind the results of the Double Slit experiment.

Keywords: Photon shape, logic operators, complex numbers.

INTRODUCTION TO MULTI-DIMENSIONAL SPACE

Imaginary numbers are invaluable in many areas of mathematics, physics, and engineering. But in general, they are abstract entities with no real-world analog. This, however, is not true, in the strange world of Quantum Mechanics, where imaginary numbers take on a real and – in some sense – measurable significance. Recent developments in our understanding of imaginary numbers have led people to equate the Real number system with the XOR logic gate and the Imaginary number system with XNOR (Gode, 2014; Hayes, 2018; O'Neill, 2021).

In quantum mechanics, imaginary numbers are used to explain and represent the fact that a particle's momentum and position are two different and interlinked properties of the particle, for instance,

$$\Psi(r,t) = Ae^{i(kr-\omega t)}$$

In this most simple example of a plane wave, we see the variable '*i*' as an exponent value. Knowing the momentum of a particle exactly, in this equation, results in its position being everywhere at once, and vice versa. To avoid running into these infinities, these two properties can only ever be known approximately. This level of uncertainty is a consequence of the Schrödinger Equation and the Heisenberg Uncertainty Principle and is a direct consequence of the imaginary number or '*i*'.

To demonstrate this relationship between momentum and position, the imaginary part of the wave function must be raised to its power. This cancels out the imaginary part of the equation to give the absolute value. A similar result can be achieved with XNOR (!Δ) and XOR (Δ). This is because XOR and XNOR are noncommutative, !Δ.Δ + Δ.!Δ= 0, just like the Quaternions and Octonions. By privileging the XNOR value, we can obtain a Real value for Complex numbers. Note that this value is different to the absolute square mod and leads to different physical results. Therefore, it is important not to get them confused with one another. The equation must be run twice; once in XNOR and then in XOR, and the results of both equations are summed together.

Using a simple polynomial example, we obtain

$$(x!\Delta + y\Delta)(x!\Delta + y\Delta)$$
$$a: -x!\Delta^2 - 2x!\Delta y\Delta - y\Delta$$
$$b: x!\Delta^2 + 2x!\Delta y\Delta + y\Delta$$
$$a + b = 0$$

Using this polynomial equation, it is possible to graph various surfaces in both XOR and XNOR spaces. The XOR universe has three spatial dimensions. The fourth spatial dimension is the XNOR imaginary axis. When the three coordinates of the real axes are combined with the fourth imaginary axis, they always cancel each other out. This cancellation results in the flat plane that denotes the particle being in all positions or momentums at once.

Plotting the above example in dimensions 'Δ, Δ, !Δ' gives the result shown in Figure 1. Whereas plotting 'Δ, Δ, Δ, !Δ', which is a fourth-dimensional coordinate, results in the flat plane shown in Figure 2.

This achieves the same results as the complex quantum mechanical equation with a minimum of effort. These

Corresponding author e-mail: chris.ozneill@gmail.com

new multiplicative rule sets are called 'Dimensional Gate Operators' (DGO) because they express dimensionality through operators based on the logic gates.

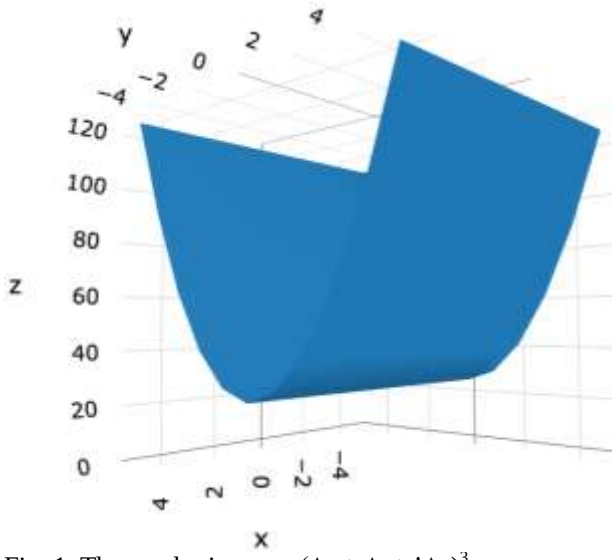

Fig. 1. The quadratic curve $(\Delta z + \Delta y + !\Delta x)^3$.

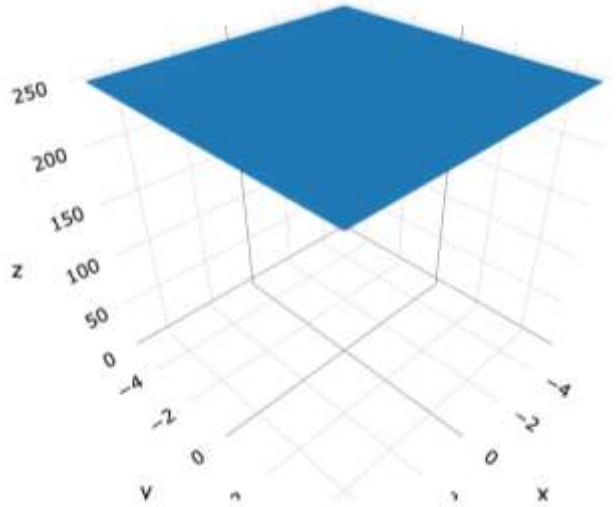

Fig. 2. Infinite plane $(\Delta w + \Delta z + \Delta y + !\Delta x)^3$.

A Better Example and Interference

When graphing the position or momentum of a particle, it is more accurate to use waveforms than mere polynomials. This waveform represents the exact momentum of a particle at time *t*. Once again, applying the XNOR and XOR gates to this returns the position value for this wave function (Fig. 3). Since it is possible to graph the XOR momentum-space component, it is a trivial matter to calculate the XNOR position-space component, which will simply be its inverse. This scenario is shown in Figure 4.

Both wave functions have so far been graphed separately. It is possible now to graph them simultaneously, see Figure 5. This is something which is ordinarily forbidden in quantum mechanics.

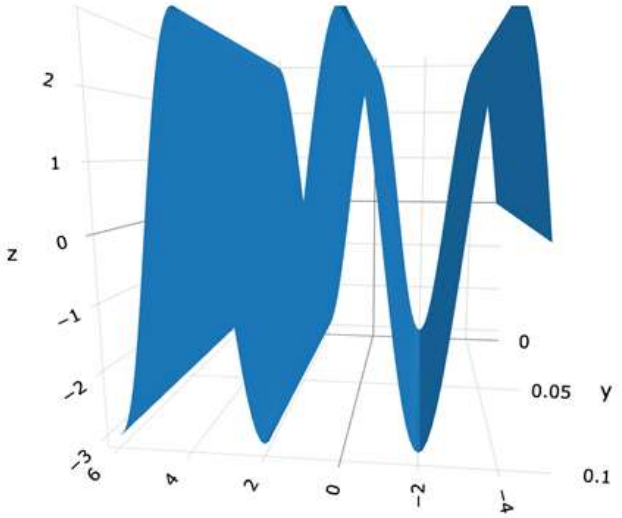

Fig. 3. Cos(Δ*x*) waveform for the momentum of a particle.

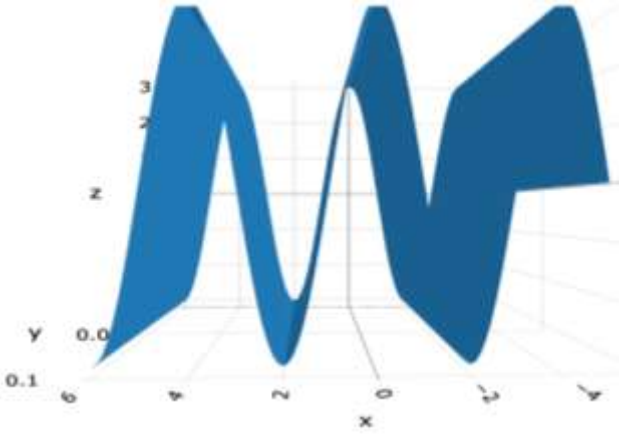

Fig. 4. Cos(!Δ*x*) waveform for the position of a particle.

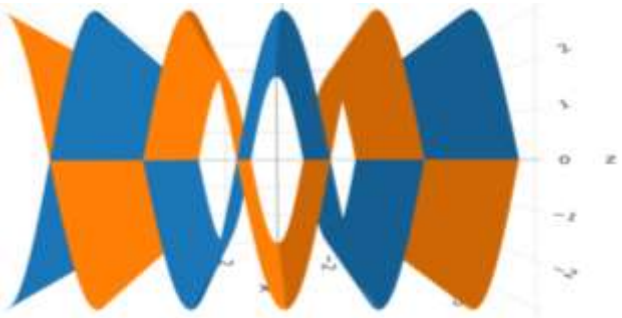

Fig. 5. The exact momentum and position-state superimposed.

From this perspective, it becomes apparent why the Heisenberg Uncertainty Principle exists. The two wave functions cancel out and what is left is the infinite value

plane in the fourth dimension (Fig. 6). This cancellation is like that of orthogonality in linear algebra. Although this waveform is only a toy model, it reveals how particles look, when viewed from both sides of the XOR and XNOR axes simultaneously.

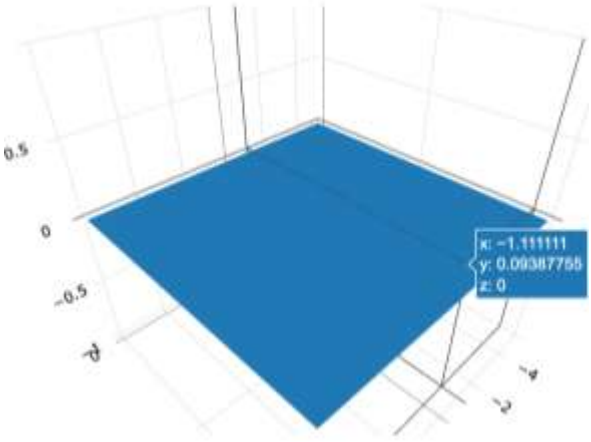

Fig. 6. The cancelled out infinite plane.

A More Complex Example

So far, a plane sine wave function has been employed to describe fundamental particles. If a truer understanding is to be had, it will be necessary to progress to a more accurate model of the photon. For this, the author has chosen initially the following Mexican Hat function:

$$z = \frac{\sin\left(\sqrt{x^2 + y^2}\right)}{\sqrt{x^2 + y^2}}$$

This function $z(x, y)$ produces the graph in XOR shown in Figure 7.

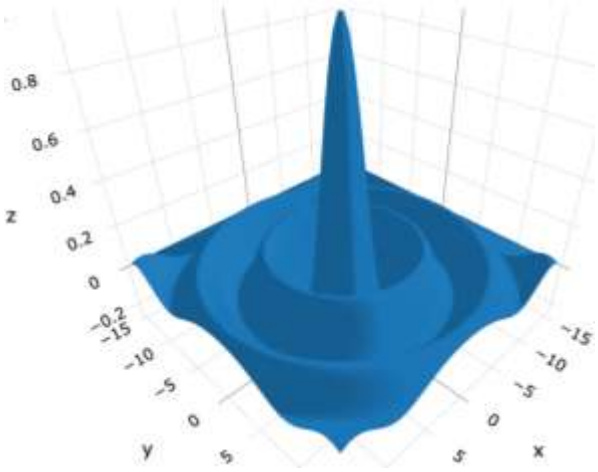

Fig. 7. The Mexican Hat graph in XOR.

For practical reasons this model is too simple, as it does not include the discrete nature of a particle that we might expect to see. This will be remedied in the next section. For now, consider Figure 8, or how the graph looks like in XNOR (see in Appendix 1 for the computer code).

Notice how this 'wave function' – although it no longer looks like a wave – curves downwards at the bottom. This characteristic is suggestive of hyper-dimensionality and has been observed in other higher-dimensional algebraic graphs (https://chart-studio.plotly.com/~robotwax/931/#/). There are also visible series of strange lines in Figure 8. These lines represent the points at which the square roots of the x^2 and y^2 are equal to zero. These points go to infinity or are otherwise undefined. Their cross shape is the result of the traces of the matrix division/multiplication (depending on the used function). By subtracting one infinity from another any real number (real value) can be produced. In this case, the value of '1' is provided. Adding in the value of –1 produces an entirely different result, which will be examined later in more detail.

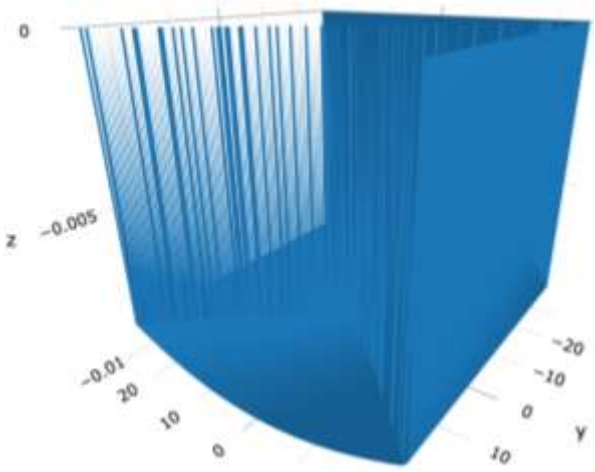

Fig. 8. The XNOR Mexican Hat graph.

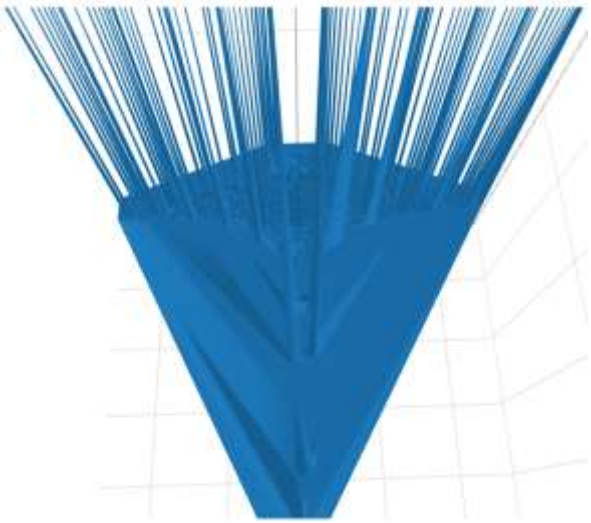

Fig. 9. The Parametric Mexican Hat graph with XOR as the *x*-axis and XNOR as the *y*-axis.

The Parametric Mexican Hat graph with XOR as the *x*-axis and XNOR as the *y*-axis is shown in Figure 9 (see in

Appendix 2 for the computer code, where the interference pattern is also shown). Another way to view these data is to set the results of our XOR calculation as our *y*-axis and the results of our XNOR calculation as our *z*-axis. This means that the two separate results of the XOR and XNOR calculation become a new coordinate set, which obviously has its advantages, when visualizing 4-dimensional space.

The waveform completely cancels out in 4D space, leaving only the infinite values. This reveals that the Mexican Hat diagram is not a valid waveform for the photon. An even more complex is therefore needed.

An Even More Complex Example

Asides from some complications with *sin*, *cos*, and exponential function, the mathematics in XNOR and its confluence with XOR is simple and straight forward enough. The function for a discrete wave packet in a 3D XOR state is

$$z = 2\exp(-1.2\sqrt{x^2+y^2})\cos(7\sqrt{x^2+y^2})\cos(x)$$

Plotting this results in the image shown in Figure 10 (see in Appendix 3 for the computer code).

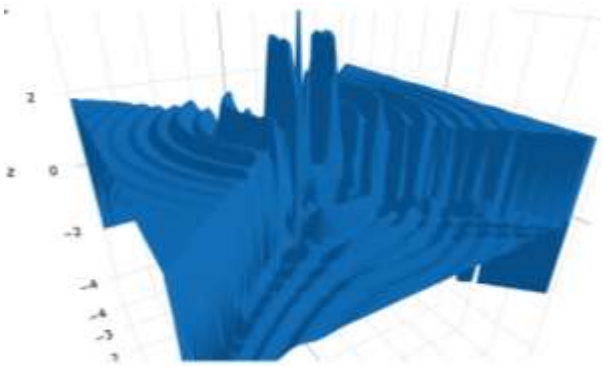

Fig. 10. The XNOR exponential function.

Again, we see this cross-shape, where the x^2 and y^2 components are undefined. Previously this value had been replaced with an '1', but now a value of '– 0.8' is more expedient. This flattens the graph down to a much more reasonable result (Fig. 11).

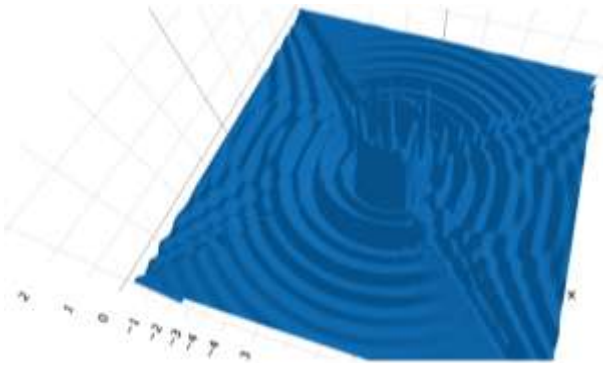

Fig. 11. The exponential XNOR graph.

Interestingly, this XNOR wave function for the photon looks very similar to the theoretical predictions based on the Schrödinger equation (Fig. 12b), as well as experimental imaging evidence carried out by physicists at the University of Warsaw (Fig. 12a). (Available at: https://cosmosmagazine.com/physics/what-shape-is-a-photon/). Graphing Figure 11 in purely XNOR gives the result shown in Figure 13.

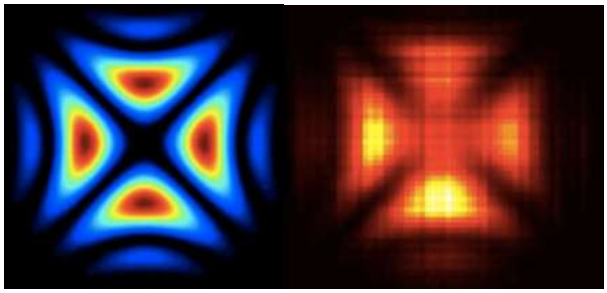

(a) (b)

Fig. 12. (a) The theoretical predictions based on the Schrödinger equation and (b) the experimental imaging carried out by physicists at the University of Warsaw.

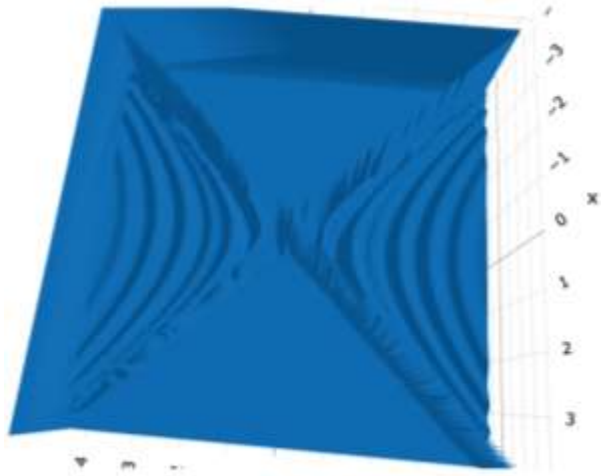

Fig. 13. The other XNOR exponential graph.

Fig. 14. The photon graph rotated by 90 degrees and superimposed.

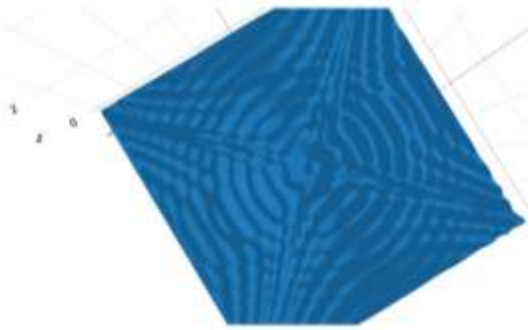

Fig. 15. The result of summation of the graphs shown in Figures 10 and 14.

With this more complex example, only half of the wave function cancels itself out. This promises this result is at least half right. To create a full XNOR momentum-space waveform, it will be necessary to graph a spherical wave front and then transform into XNOR. In leu of that, Figure 13 can be rotated by 90 degrees and summed with the original graph that is shown in Figure 14. This produces the result even closer to the result obtained at the University of Warsaw. Summing the graph shown in Figure 14 with the original flattened graph (Figure 10) results in Figure 15 (see in Appendix 4 for the code).

The Flattened Mexican Hat

Let us examine what happens with the Parametric Mexican Hat graph (see Fig. 9), when our undefined variable is set to –1. The result shown in Figure 16 is the decidedly flattened (and elongated) Mexican Hat. This is reminiscent of the theoretical Alcubierre warp drive (Fig. 17), which operates by compressing space time in front of a spacecraft and expanding the space behind it.

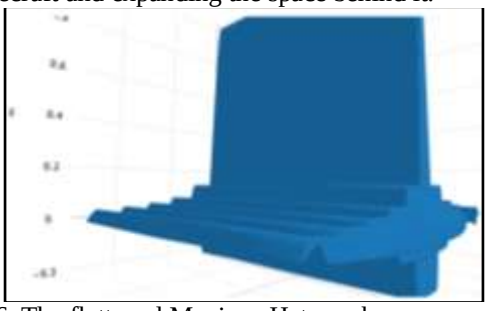

Fig. 16. The flattened Mexican Hat graph.

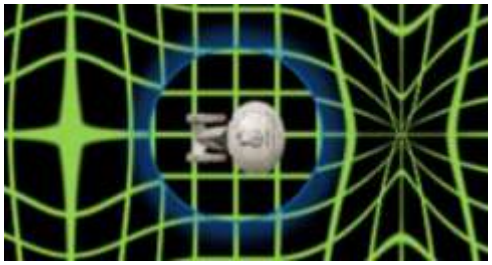

Fig. 17. The Alcubierre warp drive (Image source: https://www.universetoday.com/77005/astronomy-without-a-telescope-warp-drive-on-paper/).

Transformations of this kind can either be done on the object in question (in this case a spacecraft) or on the coordinate system surrounding them (in this case space time). These transformations are logically considered equivalent. However, notice that in the case of the flattened Mexican Hat diagram, no such transformational algorithm has been applied. Instead, the shape simply *falls out* of the XNOR and XOR data, with the XNOR axis privileged in the *y*-axis and the inclusion of the variable (–1). This means that, according to the Dimensional Gate Operator hypothesis, this is truly the momentum-state information of our particle. This is what the wave function of the photon looks like when it is travelling at light speed. This is a remarkable confirmation of the concepts set out early on in this paper, in the opinion of the author.

If indeed this is an accurate depiction of the motion of the particle, then there are numerous conclusions that can be drawn from it. First, notice the similarity between this graph and the Alcubierre warp drive. This drive is said to function on negative matter, or exotic matter. Some researchers have postulated that Dark Energy and Dark Matter may be a type of negative matter that is driving the expansion of the Universe (Farnes, 2018). If this is correct, then the arithmetic of the Dark Matter Universe is in XNOR. When a positive number is added to a positive in XOR a positive value is obtained. But doing the same thing in XNOR results in a negative. This is a good description for negative matter and since the momentum-state of the particle appears to be represented in XNOR, it would appear all matter has a dark matter component to it. This can potentially give us a way to test dark matter theory. Make note that we say 'appears', as the momentum-state is the second derivative of speed and XNOR has, as yet, no such equivalent definition.

Fig. 18. 4-D XNOR space.

As mentioned earlier, the distortion of space time by any negative energy is equivalent to distorting the metric coordinate system. Notice how there is no distortion of the metric in the 'Flattened Mexican Graph' (Fig. 16). This implies that what is being depicted in this figure is more akin to a traditional Doppler Effect than space time warping. Precisely the same perspective can be applied to the more complex wave function of the photon (Fig. 18). Figure 18 shows a slice of what a photon looks like in 4-D

XNOR space. It has a pressure front and a wake. The fact that this can be derived without recourse to relativistic motion, suggests that it is entirely non relativistic in character.

CONCLUSION

Using the XNOR logic gates in place of imaginary numbers can reproduce some of the results shown in the Warsaw experimentation. This suggests a relationship between the mathematics of XNOR space and particle physics. The method therefore provides good insight into these quantum systems. It also hints at the mechanism behind the results of the Double Slit experiment.

REFERENCES

Alcubierre, M. 1994. The warp drive: Hyper-fast travel within general relativity. Classical and Quantum Gravity. 11(5):L73. DOI: https://doi.org/10.1088/0264-9381/ 11/5/001.

Farnes, JS. 2018. A unifying theory of dark energy and dark matter: Negative masses and matter creation within a modified ΛCDM framework. Astronomy and Astrophysics. 620:A92-112. https://doi.org/10.1051/0004-6361/201832898.

Gode, DB. 2014. Complex number theory without imaginary number (i). Open Access Library Journal. 1(7):e856-869. DOI: https://doi.org/10.4236/ oalib. 1100856.

Hay, MA. 2016. Recursive distinctioning, tetracoding and the symmetry properties of chiral Tetrahedral molecules. Journal of Space Philosophy. 5(2):28-55. http:// keplerspaceinstitute.com/wpcontent/uploads/2017/11/JSP -Fall-2016-11_Hay-Final.pdf.

Merli, PG., Missiroli, GF. and Pozzi, G. 1976. On the statistical aspect of electron interference phenomena. American Journal of Physics. 44(3):306-307. DOI: https://doi.org/10.1119/1.10184.

O'Neill, CC. 2021. Reimagining complex numbers. Canadian Journal of Pure and Applied Sciences. 15(2):5261-5268. DOI:https://doi.org/10.13140 /RG.2.2. 26666.44480/1.

Received: June 29, 2021; Revised: August 17, 2021;
Accepted: Sept 24, 2021

Appendix 1.
The Python code used in the generation of the kind of graph shown in Figure 8.

```
t = np.linspace(-35, 35, 300)
c = []
lo = []
p = []
for x in t:
for y in t:
      s = math.sin(math.sqrt(x**2 + y**2))/(math.sqrt(x**2 + y**2))
      a = (x**2)*-1
      b = (y**2)*-1
if b < 0:
        a1 = a + (b*-1)
elif b > 0:
        a1 = a - b
else:
        a1 = 1
try:
        c1 = (math.sqrt(a1))*-1
exceptValueError:
        c1 = 1
if c1 == 0:
        c1 = 1
try:
        g = math.sqrt(a1)*-1
exceptValueError:
        g = 1
gb = math.sin(g/c1)*-1
     r = s + gb
p.append(gb)
c.append(x)
lo.append(y)
data = [go.Mesh3d(
           x = c,
           y = lo,
           z = p
        ),
     ]
layout = go.Layout(dict(title='Sine',
titlefont= {"size": 14},
font={'color':'black'},
paper_bgcolor= 'white',
plot_bgcolor= "white",
hovermode='closest',
xaxis={"range":[-15, 15]}))
figure = dict(data=data, layout = layout)
iplot(figure)
```

Appendix 2.
The computer code for the graph shown in Figure 9. If c1==-1 and [x, y, z] == [c, p, lo], the graph in Figure 16 (the squashed Mexican Hat graph) is obtained:

```
t = np.linspace(-15, 15, 100)
c = []
lo = []
p = []
for x in t:
for y in t:
      s = math.sin(math.sqrt(x**2 + y**2))/(math.sqrt(x**2 + y**2))
      a = (x**2)*-1
      b = (y**2)*-1
if b < 0:
        a1 = a + (b*-1)
elif b > 0:
        a1 = a - b
else:
        a1 = -1
try:
        c1 = (math.sqrt(a1))*-1
exceptValueError:
        c1 = -1
if c1 == 0:
        c1 = -1
try:
        g = math.sqrt(a1)*-1
exceptValueError:
        g = -1
gb = math.sin(g/c1)*-1
     r = s + gb
p.append(gb)
c.append(x)
lo.append(s)


data = [go.Mesh3d(
           x = c,
           y = lo,
           z = p
        ),
     ]
layout = go.Layout(dict(title='Photon XOR XNOR',
titlefont= {"size": 14},
font={'color':'black'},
paper_bgcolor= 'white',
plot_bgcolor= "white",
hovermode='closest',
xaxis={"range":[-1, 1]}))
figure = dict(data=data, layout = layout)
iplot(figure)
```

Also, steps can be taken to extract the data from Figure 9, which results in the interference pattern shown in Figure 19 below.

The reader should note however that this is not a new interference pattern. It is simply the Mexican Hat diagram

viewed in a different way. However, the ‘spikes’ shown in Figure 9 would produce the correct, although inverted, interference result (Merli *et al.*, 1976).

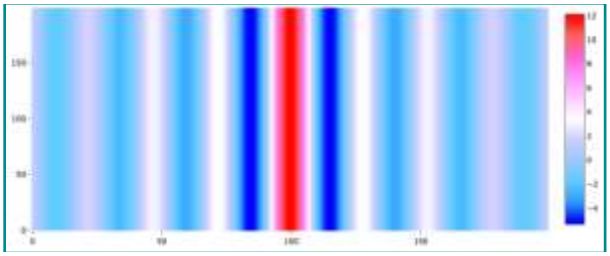

Fig. 19. The interference pattern.

Appendix 3.

The computer code for the graph shown in Figures 10 is below. To produce the graph shown in Figure 11, simply change ‘a1 = 1’ to ‘a1 = -1’ or minus phi.

```
t = np.linspace(-4, 4, 100)
c = []
lo = []
p = []
ee = []
fe = []
pv = []
uu = []

met=-1.2

tet= 10

for x in t:
for y in t:
    s = 2*math.exp(met*math.sqrt(x**2+y**2))*math.cos(((tet*math.sqrt(x**2+y**2))))*math.cos(x**2+y**2)
    a = (x**2)*-1
    b = (y**2)*-1
if b < 0:
        a1 = a + (b*-1)
elif b > 0:
        a1 = a - b
else:
        a1 = 1
try:
        c1 = (math.sqrt(a1))*-1
exceptValueError:
        c1 = 1
    tet2 = ((met*c1)*-1)
if tet2 <= 0:
        tet3 = math.exp(tet2)
elif tet2 > 0:
        tet3 = (math.exp(tet2))-tet2
gb = ((2*tet3)*-1)*(math.cos(((tet*c1)*-1))*-1)
    gb1 = (math.cos(c1)*-1)
    gb2 = (gb*gb1)*-1
    m = s + gb2
if gb2 < 0:
        r = (s+(gb2*-1))
elif gb2 > 0:
        r = (s-gb2)
qq = s + r
uu.append(m)
p.append(r)
pv.append(qq)
ee.append(s)
fe.append(gb2)
c.append(x)
lo.append(y)
data = [go.Mesh3d(
            x = c,
            y = lo,
            z = pv
        ),
    ]
layout = go.Layout(dict(title='Photon XNOR',
titlefont= {"size": 14},
font={'color':'black'},
paper_bgcolor= 'white',
plot_bgcolor= "white",
hovermode='closest'))
figure = dict(data=data, layout = layout)
iplot(figure)
```

Appendix 4.

Change the ‘*z*’ parameter to ‘o11’, ‘o13’, or ‘o14’ to produce the graphs shown in Figures 13, 14, and 15, respectively.

```
ou9 = np.array(fe).reshape(100, 100)
o10 = np.rot90(ou9, 1)
o11, o12 = np.ravel(ou9), np.ravel(o10)
o13 = [o11[i]+o12[i] for i in range(len(pv))]
o14 = [pv[i]+o12[i] for i in range(len(pv))]
data = [go.Mesh3d(
            x = c,
            y = lo,
            z = o13
        ),
    ]
layout = go.Layout(dict(title='Photon XNOR',
titlefont= {"size": 14},
font={'color':'black'},
paper_bgcolor= 'white',
plot_bgcolor= "white",
hovermode='closest'))
figure = dict(data=data, layout = layout)
iplot(figure)
```

Canadian Journal of Pure and Applied Sciences
Vol. 15, No. 3, pp. 5341-5344, Oct 2021
Online ISSN: 1920-3853; Print ISSN: 1715-9997
Available online at www.cjpas.net

AURA DETECTOR BASED ON LUMINESCENCE

*Vitaliy Zamsha[1] and Vladimir Shevtsov[2]
[1]International Institute for Experimental Physics, Perth, Australia
[2]International Institute for Experimental Physics, Novopolotsk, Belarus

ABSTRACT

In this short communication, the authors described the proposed aura detection system based on the luminescence phenomena in combination with the photomultiplier. This system can detect aura of living organisms and nonliving objects. Such aura detecting systems can be used in various fields of activity: in medicine, biology, ecology, etc. It can be also used as the receiver in new communication systems, in which the torsion field participate.

Keywords: Aura detection, spin-torsion field, luminescence, new telecommunication.

INTRODUCTION

There are several methods to detect aura of objects (the aura can be treated also as some spin-torsion field (Arcos and Pereira, 2004; Shipov, 1998) of the object.) To detect the aura of an object, it can be used the luminescence phenomena, which is a light emission by a substance (luminophore) as the result of an external influence of different types of radiation: like X-ray, any other high energy emission, chemical reaction, torsion field, scalar wave, etc. The idea of such "detector" was proposed by the outstanding Russian scientist Alexander Barchenko (Fig. 1).

Fig. 1. The outstanding Russian scientist A. Barchenko.

Barchenko has discovered this phenomenon in the first quarter of the 20th century. He demonstrated how luminophore can detect the human aura. In his "aura detector", he used a piece of paper covered with luminophore such as calcium sulfide (CaS). To use that "detector", it needs first to be activated by the sun lights for a short time and then it can be placed above the human head as shown in Figure 2. That experiment was confirmed by several extrasensoric people because they can see similar aura around the human head by their 3rd eye. In the book by Shkatov and Zamsha (2015), it was also discussed some aura detection system based on the luminescence phenomena (Valeur and Berberan-Santos, 2011). The term "luminescence" was introduced by Lum (1888).

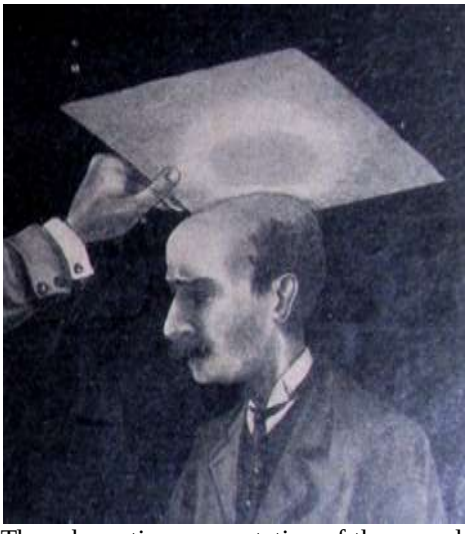

Fig. 2. The schematic representation of the aura detection by the activated detector.

*Corresponding author e-mail: spincom@yahoo.com

RESULTS AND DISCUSSION

The authors of this paper have developed a modern aura detecting system based on the Barchenko's method by using modern electronics and computer. The proposed aura detection system consists of the photomultiplier (FEU-79 - Russian), high voltage (2kV) supply, microcomputer ATMEGA-8, pre-amplifier, luminophore activator. It was also used a white LED with solenoid control and a chamber for luminophore screen, and test samples representing objects whose aura will be tested. All these components were assembled in the metal box. Instead of separate luminophore screen it can be used some test sample (or photo address object) coated with luminophore. This system detects the aura by counting photons of the light emission from the luminophore screen, which is "bombarded" by the test sample's spin field (or influences by its aura). Should note that the luminophore screen plays a role of "translator" (or in other words, a scintillator) that "translates" the test object's spin field emission into the visible light necessary to count by the photomultiplier. Sampling rate of the measurement is 1 second. The luminophore screen activation time is by about 0.5 second. Each result is processed by the local microcomputer (ATMEGA-8) and then the results are sent to the big computer for further mathematical processing.

The built Aura Detecting System (Fig. 3) can work in two modes: the active mode and the passive mode. In the active mode, the luminophore screen is periodically activated with the LED's light and then activated luminophore emits light which brightness depends in accordance to the influence of the test sample's aura or its strength changes. This mode is nonlinear as can be seen in Figures 4 and 5. The examples of the nonlinear measurements are shown in Figures 5a and 5b, in which all the six consecutive measurements are combined into the one graph for convenience of the observation of the difference between the background noise and the actual signal.

The passive mode is used when the test sample can emit its own light and whole measured photon counts are almost aligned horizontally as shown in Figure 6. In this mode, the activation LED is not used.

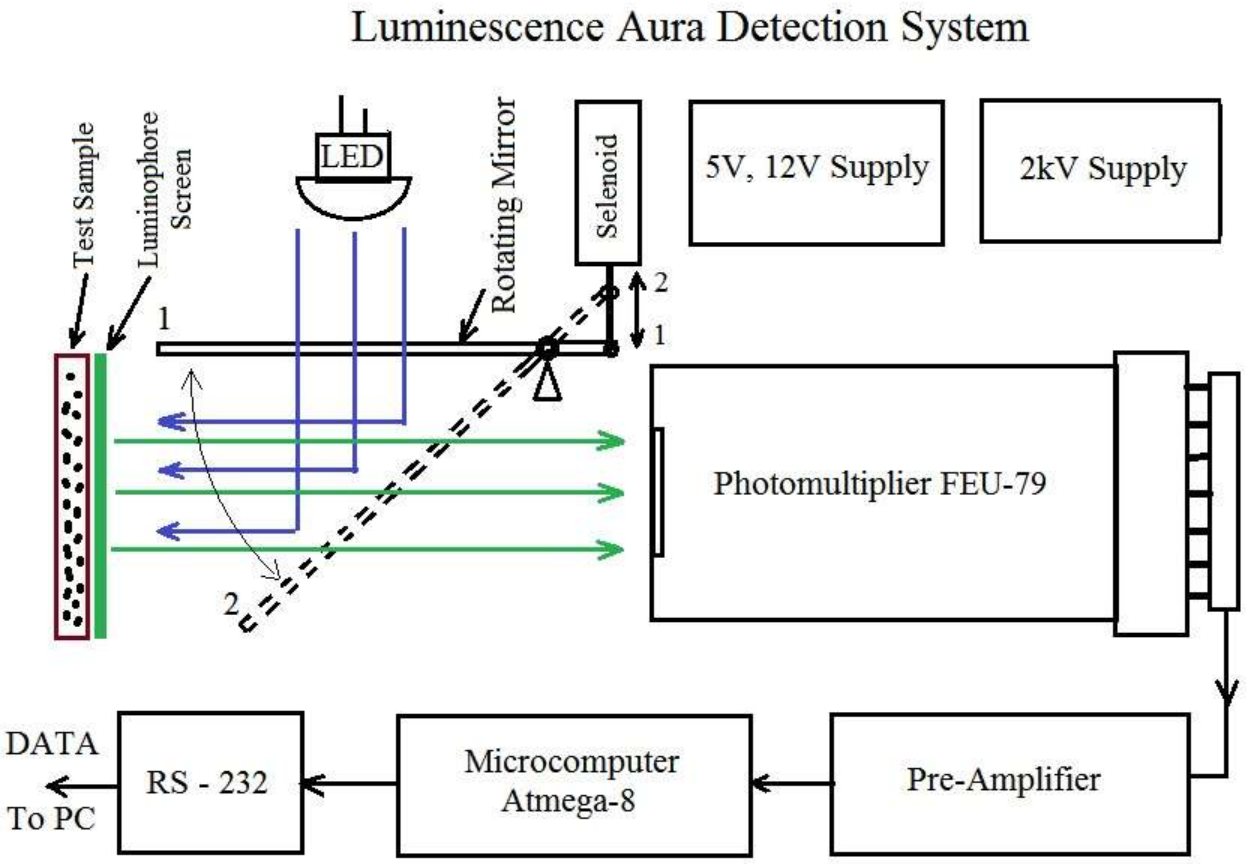

Fig. 3. The activation stage: The mirror rotates to position 2 and the LED sends light to the luminophore (the blue lines). The green lines show the "signal" light modulated by the Test Sample when the mirror is closed to position 1.

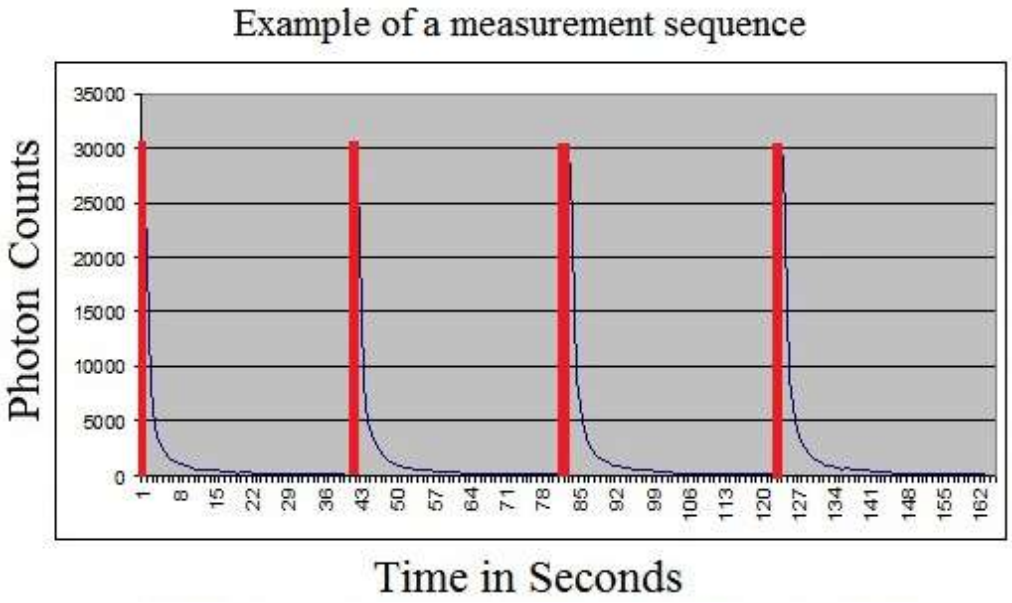

Fig. 4. The luminophore activation time by the LED (the red lines) and the light emission of the activated luminophore (the blue lines).

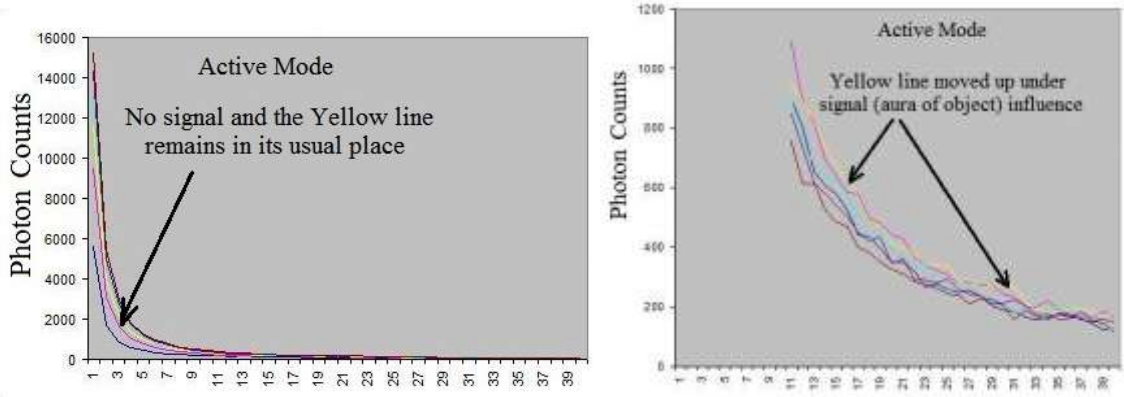

Fig. 5. The examples of the nonlinear measurements: (a) no signal and (b) with the aura signal.

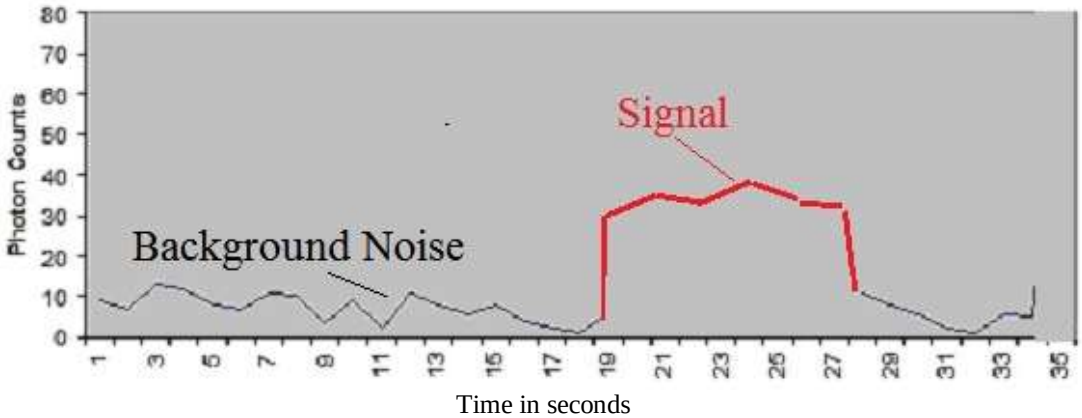

Fig. 6. The clear signal in the red colour above the background noise.

CONCLUSION

According to the first results of the object's aura detecting, the aura detecting system proposed by the authors can be used in various fields of activity: in medicine, biology, ecology, new type of telecommunication, etc. Some examples of the new (tele)-communication, in which it is necessary to take into account the torsion field, were recently discussed in (Zakharenko, 2018, 2020). The authors of this short report continue to improve their system.

REFERENCES

Arcos, HI. and Pereira, JG. 2004. Torsion gravity: A reappraisal. International Journal of Modern Physics D. 13(10):2193-2240. DOI: https://doi.org/10.1142/S0218271804006462.

Lum, QC. 1888. Über Fluorescenz und Phosphorescenz, I. Abhandlung. (On fluorescence and phosphorescence, first paper). Annalen der Physik. 34:446-463.

Shipov, GI. 1998. A Theory of Physical Vacuum. A New Paradigm. ZAO "GART", Moscow, Russia, pp.312. In Russian.

Shkatov, V. and Zamsha, V. 2015. Torsion Field and Interstellar Communication. Easy Print, China. pp.30. http://www.iga1.ru/pribor/TorsionField.pdf

Valeur, B. and Berberan-Santos, MN. 2011. A brief history of fluorescence and phosphorescence before the emergence of quantum theory. Journal of Chemical Education. 88(6):731-738. DOI: https://doi.org/10.1021/ed100182h.

Zakharenko, AA. 2018. On necessity of development of instant interplanetary telecommunication based on some gravitational phenomena for remote medical diagnostics and treatment. Canadian Journal of Pure and Applied Sciences. 12(2):4481-4487. DOI: https://doi.org/10.5281/zenodo.1301289.

Zakharenko, AA. 2020. On evaluations of fast speeds of propagation of gravitational phenomena: A review. Canadian Journal of Pure and Applied Sciences. 14(1):4947-4963. DOI: http://doi.org/10.5281/zenodo.3688779.

Final Revised: June 30, 2021; Accepted: August 30, 2021

Canadian Journal of Pure and Applied Sciences
Vol. 15, No. 3, pp. 5345-5352, Oct 2021
Online ISSN: 1920-3853; Print ISSN: 1715-9997
Available online at www.cjpas.net

REVIEW OF CLIMATE CHANGE AND ITS EFFECTS ON BIODIVERSITY

*Sehrish Khan[1], Saima Siddiqui[2], M. Asif Iqbal[1], Ghazala Yasmeen[1], Ubaid Ullah[1], Afsheen Zehra[1], Tahira A Lateef[1], Shaista Aslam[1] and Naseem Samreen[1]
[1]Wildlife Section, Department of Zoology, University of Karachi, Karachi-75270
[2]Department of Zoology, Federal Urdu University of Arts, Science and Technology, Karachi, Pakistan

ABSTRACT

Globally climate change and loss of biodiversity are major environmental threats that we are facing today. Changes in species habitats compositions, and consequently changes in ecosystem functioning are some major effects of climate changes. There are various natural or anthropogenic activities that cause fluctuations in the climatic condition. Natural causes are volcanic eruptions, variability in the solar radiations, plate tectonic and orbital fluctuations of the Earth. While other are human activities that causes the climatic variations such as deforestation, over exploitations of natural resources, industrial toxic effluents, extensive agricultural practices, mismanagement of valuable resources and many more. When climate fluctuates from normal level, it has adverse effects on the biodiversity. Firstly it affects the temperature either increase or decrease at extreme level that leads to various changes within the ecosystem and then their interaction with wild or aquatic species causes disruption in different activities perform by the producers, herbivore and carnivore fauna. Due to climatic variations glaciers are starting to melt, increases the aquatic level which ultimately leads to the flooding conditions and produce harm to human being, destruct the habitat as well as disturbs the animals of aquatic ecosystem. On the other hand when the water of these melting glaciers enter into the sea it decreases its salinity which causes threats to the survival of many marine species. Ice covers in the upper surface of water also melts due to temperature increase and this phenomenon influence the productivity of phytoplankton upon which the whole marine life depends on. In addition it causes strong storms and tornados which made severe destructions, also drought due to less rains and prolonged heat waves influence badly on biodiversity. Several species are also affected by the threats of climate fluctuations as they adapt themselves or migrate for their survival. Other impacts of climate change includes early migration of birds and delayed return due to harsh weather conditions, changes in breeding cycle and the synchrony of two mutual species that are interlinked with each other in various aspects of predation and availability food. Species of sea turtle lost several nesting sites, due to sea levels rise and unsustainable coastal developments. In this paper we review natural causes and anthropogenic activities and their effects on biodiversity, terrestrial ecosystem, change on species phenology, population range and its composition, habitat fragmentations, affected functions of ecosystem, coral bleaching, migration of aquatic species, and rising sea levels.

Keywords: Terrestrial ecosystem, population range, habitat fragmentation, migration of birds, species phenology.

INTRODUCTION

The continuous changing in weather patterns is termed as climate change. Now a days it is of main concern because it affects the world in several way. In 1990's many countries become the signatories of UNFCCC known as Kyoto Protocol whose aim is to reduce the carbon emission. According to which developed signatories countries have to reduce about 18% from total emission. Then new agreement was introduced in 2015 called Paris Agreement whose work is to make balance with the draft of action plan to limit global warming below 2°celcius (Rafi, and Riaz, 2018).

There are several natural and anthropogenic activities direct and indirect sources that causes climate change:

1. Natural causes

a). Volcanic Eruptions

Different gases are expel out from the volcanic eruptions like carbon dioxide and sulfur dioxide also they discharge aerosols (ash, viruses, bacteria or dust) in the stratosphere. These aerosols are in the form of liquids and solids that floats freely in the atmosphere. Aerosols scatter in the stratosphere blocks the sunlight radiation and produce a cooling effect that may continue for 1-2 years (NASA, 2019).

*Corresponding author e-mail: sehrishnaeem7@gmail.com

b). Solar Variability

The solar production fluctuates through time depends on the quantity of sunspots that causes the climate change. These sunspots are darker areas on the surface of sun, appear due to lower temperature as compared to the surrounding area. These spots presents at the point where an intense magnetic field reduces the flow of gases that transmit heat energy from the sun's interior. Large quantity of these sunspots may contribute to warmer global climate, less appearance of sunspots indicates the cooler global climate. About 300 years ago, there was an epoch of decreased solar activity, called as "Little Ice Age" (NASA, 2019).

c). Plate Tectonics

Tectonic plates carried landmasses at different latitudes. These modifications in the positions, effects the circulation patterns of sea water and air also produce fluctuations in the climate of continents. Coal mines are the best evidence that how the plate tectonics affects the climate. These mines were produced over millions of years ago in the regions of tropics, now they are found at higher latitudes.

Industrial revolution also play important role in climate change, the Northern Hemisphere has been warmed as compared to the Southern Hemisphere. The reason behind which is that the Northern Hemisphere have a greater quantity of Earth's continent, less of ocean than the Southern Hemisphere (NASA, 2019).

d). Orbital Fluctuations

Three cyclical alterations in the orbit and tilt of earth were described by the Milankovitch in his theory that produced the modifications in climate. These modifications include; (1) alteration of Earth's orbit tool place at every 100,000 years, (2) produced tilt (obliquity) in the axis of Earth that took place at every 41,000 years, and (3) formation of wobbling (precession) in the axis of Earth about 23,000 years.

Glacial periods began when these three cycles regulate to favor an extended period in which the solar radiation become high in the winter season and become less in the summer season at 65°N latitude. In this case the temperature at northern latitudes increases as well as the high amount of precipitations in the air resulted in the snowfall. Cool summer at the northern latitudes promotes the formation of glaciers and inhibits the melting of winter snow (NASA, 2019).

2. Anthropogenic Activities

The other sources of climatic fluctuations impacted by the human activities are the disproportionate use of chemical fertilizers, secretion of greenhouse gases, fossil fuels burning, deforestation, over exploitations and over grazing of livestock (Rafi and Riaz, 2018).

The carbon dioxide which is one of the greenhouse gas, confined heat in the atmosphere which then produce fluctuations in the climate. Greenhouse gases are naturally present on the earth, but anthropogenic activities further increased their quantity by deforestation, and industrial effluents. Greenhouse gases performs like a cover. The broadness of this cover is directly proportional to the warming of the planet Earth. Meanwhile, the extra amount of carbon dioxide are stored in the aquatic ecosystem of earth that leads the environment more acidic which not suitable for the organisms live their also causes threats to their survival (WWFa, 2019).

In the Arctic region, wild and marine fauna are also affected by the mining, spilling of oil, and other activities like drilling for the resources of gas and oil etc. Human activities also causing depletion of ozone layer which leads to the melting of glaciers in Antarctica and Arctic regions. Ultimately the water comes out from glaciers due to melting is subjected for rising of sea levels worldwide. The rise in the ocean level causing high threats to island countries like Sri Lanka and Maldives (Rafi and Riaz, 2018).

Effects of Climate Change

As a result of effects of climate changing effect changes to ecosystems under the adverse effects climate change are likely to have significant and often negative economic, social and cultural consequences (Birdlife International, 2021). There are several effects of climate change that have been felt already, and by the time they will get worse. It is observed that the Global warming has increased nearly 1°C as compared to the pre-industrial conditions. There is a big importance of fluctuations in temperature and the increase of just half degree (or even less than half degree) of global warming have negative impacts on earth or biodiversity that ultimately leads to the survival of human in danger (Amnesty international, 2019). Some effects of climate change are as follows:

1. Heat waves and Drought Conditions

Climatic fluctuations causes the severe drought and prolonged heat waves. Progressively, nevertheless, hot and dry places will become hotter and drier, and those places that were once temperate and had regular rainfall will become more and more sizzler and with less humidity.

These heat waves and droughts will become an increasingly important killer, (especially for the very young and the old ones) and puts much pressure on water availability and sewage systems, also reduce the ability of

a country to feed themselves or export agricultural products (Shafer, 2017).

2. Downpours and Storms

Torrential downpour and destructive storms will largely effects the agricultural areas, cities, shipping and electric power systems and the industries of countries by destructing them without the financial or human capital resources to return (Shafer, 2017).

3. Rise in the Sea Level

Due to climate change temperature start increasing that causes melting of glaciers which ultimately leads to the rise up of sea level and the increase sea level wont penetrate the light much deeper also effect the productivity of phytoplankton and disturbs the marine biodiversity (Shafer, 2017). In Pakistan the last 50 years, the annual mean temperature has increased by roughly 0.5°C, while Sea level along the coast of Karachi has risen approximately 10 centimeters in the last century (Chaudhry, 2017). Another earlier study Rabani *et al*. (2008) reported that the Sea level rise for Pakistan is estimated at 1.1 mm per year (mm/year) from 1856–2000 along the Karachi coast.

4. Melting of Glaciers

Ice caps, snowed areas and glaciers are melting day by day that covers 17% of Himalayan region (Dyurgerov and Meier, 2005; IPCC, 2007a). They are departure more rapidly in recent years (Ren *et al.*, 2004; Liu *et al.*, 2006; Zemp, 2008). Continues increase in temperatures causes the shrinkage glaciers present on Tibetan Plateau nearly from 500,000 km^2 to 100,000 km^2 by the year 2035 (Cruz, 2007; Ye and Yao, 2008).

DISCUSSION

Effects of Climate Change on Biodiversity

The variations among all living organisms present on earth and their interactions associated with marine, terrestrial and other aquatic ecosystems and the ecological interactions of their habitat. It includes variations within species, between different species, and many ecosystems (Heywood and Watson, 1995). Several components of climate change are anticipated to affect all the levels of biodiversity, from organism to biome levels (Parmesan, 2006).

There are three levels of biodiversity:

1) Species level
2) Ecosystem level
3) Genetic level

Earlier studies shows that throughout the world number of species are about 13 million from which only around 1.6 million species have been identified along with their description (Heywood and Watson, 1995). Specific areas of world indicates the fast rates of species depletion leads to high levels of endemism which is called as hotspots found in the areas of tropical forest, Mediterranean sea and coral reefs (Myers, 1988).

Threats to biodiversity have a prolonged list among which some are over exploitation, industrial pollution, modification of habitat, alien species and population growth. Among these all the major threat that causes destruction to biodiversity is the Climate change which is due to natural as well as human activities.

Due to continuous climate change humans and other wild animals face increased threats for their survival. Disastrous storms, prolonged heat waves, severe drought, increasing aquatic levels, fluctuations in the temperatures of ocean, melting of glaciers and polar ice reduction these all are due to climate change and it influence upon the human life by altering their habitat and also affects their economy by disrupting biological diversity (WWFb, 2019).

Scientists believed that disruption of biodiversity leads to the destruction of ecosystems that ultimately effects the survival of human (Myers, 1979, 1989; Ehrlich and Ehrlich, 1981). A recent study (WWF, 2018a) reported that up to 86% of birds, 80% of mammals and 90% of amphibians could potentially become locally extinct in the Miombo Woodlands in Southern Africa, while 89% of amphibians could become locally extinct in southwest Australia. Green turtle, Leatherback turtle and Loggerhead turtle were reported in the Mediterranean area, due change of climate all three species are threatened (WWF, 2018b).

Effect of Climate Change on Terrestrial Ecosystem

Warming due to the climate change may possibly shows four types of variations in species characteristics. (1) The population of species may vary at specific location, also they starts movements towards the areas that are suitable for the maintenance of their metabolic temperature. (2) The phenology like flowering and egg lying of different species were modified in the history due to the temperature fluctuations. (3) Change in the physical appearance and behavior of a species. (4) Shifting in the genetic frequencies (Root *et al*., 2003).

Effects of Climate Change on Species Phenology

The developmental pattern, species interaction and geographical distribution of amphibians and reptiles are highly affected by the fluctuations in climatic conditions as compared to the other ectotherms. The variations in temperature and moisture influenced upon their population status and reproductive success. The process of oogenesis and spermatogenesis in different species of

reptiles and amphibians based on seasonal temperature system.

The sex of offspring in reptiles are influenced by the variations in temperatures thus, it directly effects the composition of a population. The number of male and female offspring of Painted turtles (*Chrysemys picta*) largely dependent upon the mean temperature of July and the slight increase (2-4℃) in temperature can cause the birth of female offspring while the male sex would negotiate (Janzen, 1994; Rhen and Lang, 1998). Meanwhile the reproductive period in some species of amphibians that are found in Britain are also influenced by the winter warming (Beebee, 1995).

That variations modify the habitat of breeding ponds that sudden respond by the interaction of other species or predators, causes early migration of newts (*Triturus* spp.) in ponds, meanwhile frog (*Rana temporaria*) not able to significantly modify their phenology associated to reproductive cycle. Early-birth of embryos and larvae of frogs then remain uncover leads to extreme predation by newts.

The above mention points are great examples that indicates the effect of climatic fluctuations upon a specific species or population dynamics, composition including reproductive success and survival are very severe. Indirect influences also noticed upon the population composition of montane amphibian species (Pounds *et al.*, 1999).

Reduction in the acute population have been observed in the region of Western USA and Costa Rica which is associated with the epidemic disease and the alteration in the pattern of precipitations caused by the sudden increase in temperature (Pounds *et al.*, 1999; Kiesecker *et al.*, 2001). In addition, the population status of frogs and Anoline lizards (*Norops* spp.) are also reduced in Costa Rica due to the variations in climatic conditions (Pounds *et al*., 1999).

High chances of competition for nestling sites between the birds, those migrated due to late arrival of spring season and other species whom arrived earlier (Both and Visser, 2001).

Some observations point out that the simultaneous development between oak bud burst and hatching of Winter moth (*Operophtera brumata*) are affected because of the warmer spring season in Europe that resulted in the imbalancement of high food demands by Great tit (*Parus major*) nestlings and the availability of high level of insects population (Visser and Holleman, 2001; Visser *et al*., 1998).

Further studies shows that the juvenile of large mammals are threatened due to extreme climatic conditions, generally in winter, even though vulnerable upon population composition (Post and Stenseth, 1999; Milner *et al*., 1999). The fertility and developmental patterns of Soay sheep (*Ovis aries*) (Forchhammer *et al*., 2001) and Red deer (*Cervus elaphus*) (Post *et al*., 1997) also affected by the long durations of warm winters related to NAO in the UK and Norway. And the affected conditions over population composition can only be observed after some time from months to years when the cohorts are able to reproduce (Post and Stenseth, 1999; Forchhammer *et al*., 2001). Climatic fluctuations can directly affects the tropic level of producer, herbivore and carnivore by producing impacts on various compositions of their basic needs (Post and Forchhammer, 2001) and indirectly by the arbitration of interactions in the tropic level like wolf predation and moose herbivore (Post *et al*., 1999).

Effects of Climate Change on Population Range and Its Composition

Some studies reported that populations of several wild species have declined, and although in many cases climate change is believed to have contributed to the decline, attributing this is fraught with difficulty as it is likely to be only one driver amongst many (Birdlife International, 2021). Variations in the population distributions of butterflies in Britain have been observed due to minor increase in temperature which is less than one degree during the recent century (Ford, 1982). In addition, warming also causes the growth of birch towards north in the Swedish tundra during the first half of present century (Kullman, 1983). Nonetheless, species those are affected by the climate change have to migrate or adapt the change for the survival (Kappelle *et al*., 1999).

Some specific species are sensitive to the climatic fluctuations, indicates the condition of environment called as bio indicators used to know the conditions of a whole ecosystem. (Kappelle *et al*., 1999). These indicator species occupy six criteria are; (1) Constant habitat, (2) Position in a particular area, (3) Sensitive to the climatic variations, (4) Dispersal range, (5) Easily available for monitoring and (6) Functional position within the environment.

In the region of Western Europe and Netherlands different species of herbaceous plants, butterflies and birds are indicated as convenient for the purpose of bio indicators (De Groot *et al*., 1995). Korean pine trees are long-lived, but change of climate can lead to reduced cone formation and increase the risk of loss of some species (Warren *et al*., 2018).

Variations in the geographic range of particular species or its proportion can be easily determine by the prolong analysis of monitoring with the help of Geographic Information Systems- GIS (Heil and Deursen, 1996).

Climatic fluctuations and their effects may also observed by the natural transitions of eco-climate or other eco-tones due to their highly sensitive nature to climatic changes (Kappelle *et al*., 1999).

Habitat Fragmentations

From the historic periods the disruption and fragmentation of habitat causes threats to the survival of species also decreased in the Biodiversity within local, regional or global ranges (Harris, 1984; Myers, 1989). The effects of habitat fragmentation associated with the climatic fluctuations may be result in the high rates of extinction (Myers, 1989; Peters and Lovejoy, 1992). Fragmentation effects upon the isolation of species population also decreased the genetic variability. It is also act as a barrier and inhibit the migration and distribution of particular species or population towards the habitat of their interest where they tolerate the temperature (MacArthur and Wilson, 1967; Peters and Lovejoy, 1992; Bierregaard *et al*., 1997).

Native of an area which is a patch of fragmented habitat have to migrate and adjust their geographic range for their survival during climate fluctuations which rely on their migration potential also the size of patch, distance between two patches and level of connectivity by means of corridors, and the strength of barrier between two patches. Creating a potential barrier between to patches is the human way of managing the migration potential of animal but we not truly know about it, that either it increases the strength of migration or not. Also no proper research found on the topic like their width, position of placement in an area and the ratio (from edge to area) (Halpin, 1997).

Affected Functions of Ecosystem

Under the effects of climate change several ecosystems are highly vulnerable such as alpine meadows in the Rocky mountains and some barrier islands (Khan, 2006). Due to the fluctuations in the climatic conditions the functions of ecosystem also affected by the change in the physiology of species due to the temperature fluctuations and humidity. This variations in the climatic conditions may influence upon species as either they are adapted to this situation or disrupt their interactions with other species or individual led to the extinction or migration towards the suitable habitat which causes the reduction or loss of biodiversity in a specific ecosystem (Kappelle *et al*., 1999).

There are 80,000 plant species recorded in Amazon area. These plant help local water cycles and regulate the global climate, and sustain the rainforest's rich faunal life, but increasing of temperature all plant species at risk of local extinction (Warren *et al*., 2018). Climatic variations also causes the separation within a species, effect upon the heredity of a species and led them to the risk of extinction (Kappelle *et al*., 1999).

Impact of Climatic Fluctuations upon Aquatic Ecosystem

ICE Cover Reduction

The fluctuations in climatic conditions on northern hemisphere will decreased the ice covers from the lakes (Magnuson *et al*., 2000), that effects different processes includes the light penetration associated with aquatic plants and algae, also increase the time period in which aquatic organisms may have threats of predation by birds and terrestrial animals (Rahel, 2008).

Events of Coral Bleaching

Climate change causes the increase in temperature which affects the coral reefs, including Australia's Great Barrier Reef by increasing their mortality rate, as they are severely sensitive to temperatures. This coral bleaching causes malnutrition, decreased and mortality of the coral reefs upon which many aquatic species are dependent (Fujita, 2013).

Migration in Aquatic Species

It is observed that the fishes of North Sea migrates furthermore towards the north or into deeper sea because of the increase in water temperatures. Several other species also suffer due to climatic changes or other problems. Decreased in the ice cover of ocean which is due to the high temperature has influenced the population distribution of penguin species in the region of Antarctic Peninsula (WWFb, 2019).

Reduction in Mixing of Sea Water

The mixing of sea water are of great importance because during the period of mixing different nutrients scattered throughout the water body and amount of nutrient become equal everywhere. Oxygen which is present in the surface water at high level also distributes to the deeper water but due to climate change the process of mixing water become decreased which causes the low level of oxygen in bottom that ultimately leads to many problems for bottom dwellers like difficulty in breathing or aerobic respiration (WWFb, 2019).

Rising Sea Levels

Due to the climatic fluctuations the polar ice and glaciers starts melting and water starts warming day by day that causes thermal expansion and if it continues then it is predicted that the global level of sea risen up during the next 100 years about 69 cm. This increase in water levels will disrupt and affect the marine life. The penetration of light will be limited at upper surface that influenced the productivity of phytoplankton upon which whole marine life dependent also the increase of water level can

contribute to increase amount of floods. The Rapid increase in sea level is also a threat for mangrove ecosystems because they need constant level of sea for their survival (WWFa, 2019).

Mitigation Measures For Global Warming

Renewable Energies

We have to close the chapter of fossil fuels to control the climate variations and in contrast we can use solar energy, wind waves, biomass and geothermal energy (Global Warming Prevention, 2019).

Sustainable Use of Water and Energy

We can use alternative for the water and energy sources that produce energy by the help of bulbs of LED light, and sustainable shower system these are of cheap cost with same quality (Global Warming Prevention, 2019).

Transport System

To reduce the global temperature we can use local transport for public with the addition of hydrogen and electric transport leads to the reduction in the CO_2 (Global Warming Prevention, 2019).

Recycling

Consumption of food, clothing, and cosmetics should be reasonable. Also recycling is the major thing upon which we can easily reduce the climatic variations at some level (Global warming prevention, 2019).

Banned Plastics

Plastics made material should be banned or may introduce its alternate because it is the major threat at all levels.

CONCLUSION

In last two years almost every part of the world, the Covid-19 pandemic caused devastating human, economical and social distress and has reinforced the need for urgent action on reversing ecological degradation. Drivers of biodiversity loss like climate change and unsustainable land practices disrupt the balance of nature and can raise the risk of zoonotic disease transmission. The urgent actions required to improving the conservation of all globally threatened plant and animal species have been identified. We can control the climate change at some extent at least the remaining biodiversity or natural resources we have be used sustainably so that the future of earth would be more protective for future generation. The Paris Agreement for climate change is aims to hold the increase in global average temperatures to well below 2 degrees Celsius, while striving to limit the increase to 1.5 degrees Celsius. All member countries filed nationally determined contributions indicating the climate actions they plan to implement by 2030.

REFERENCES

Amnesty international. 2019. Climate change.

Beebee, TJC. 1995. Amphibian breeding and climate change. Nature. 374:219-220.

Bierregaard, RO., Laurance, WFJ., Sites, JW., Lynam, AJJ., Didham, RK., Andersen, M., Gascon, C., Tocher, MD., Smith, AP., Viana, VM., Lovejoy, TE., Sieving, KE., Kramer, EA., Restrepo, C. and Moritz, C. 1997. Key priorities for the study of fragmented tropical ecosystems. In: Tropical Forest Remnants: Ecology, Management, and Conservation of Fragmented Communities. Eds. Laurance, WF. and Bierregaard, RO. Jr. University of Chicago Press, Chicago, IL. USA. 515-525.

Birdlife International. 2021. Impacts of climate change on biodiversity and ecosystem services. http://www.birdlife.org

Both, C. and Visser, ME. 2001. Adjustment to climate change is constrained by arrival date in a long-distance migrant bird. Nature. 41:296-298.

Chaudhry, QUZ. 2017. Climate Change of Pakistan. Asian Development Bank. 6 ADB Avenue, Mandaluyong City, 1550 Metro Manila, Philippines. pp 130.

Cruz, R. 2007. Climate change 2007: impacts, adaptation and vulnerability. Contribution of Working Group II to the Fourth assessment report of the Intergovernmental Panel on Climate Change. 469- 506.

De Groot, RS., Ketner, P. and Ovaa, AH. 1995. Selection and use of bio-indicators to assess the possible effects of climate change in Europe. Journal of Biogeography. 22: 935-943.

Dyurgerov, MD. and Meier, MF. 2005. Glaciers and changing earth system: a 2004 snapshot. Institute of Arctic and Alpine Research, University of Colorado, Boulder, Colorado, USA.

Ehrlich, P. and Ehrlich, A. 1981. Extinction: The Causes and Consequences of the Disappearance of Species. Random House, New York, NY, USA.

Forchhammer, MC., Clutton-Brock, TH., LindstroÈm, J. and Albon, SD. 2001. Climate and population density induce long-term cohort variation in a northern ungulate. J. Anim. Ecol. 70:721-729.

Ford, M. 1982. The Changing Climate. Georg Allen & Unwin, London.

Fujita, R. 2013. 5 ways climate change is affecting our oceans. Environmental Defense Fund.

Global Warming Prevention. 2019. Solutions to global warming, the solar impulse foundation.

Halpin, PN. 1997. Global climate change and natural-area protection: management responses and research directions. Ecological Applications. 7:828-843.

Harris, LD. 1984. The Fragmented Forest. The University of Chicago Press, Chicago, IL, USA.

Heil, GW. and Deursen, WPAV. 1996. Searching for patterns and processes: modelling of vegetation dynamics with geographical information systems and remote sensing. Acta Botanica Neerlandica. 45:543-556.

Heywood, VH. and Watson, RT. 1995. Global Biodiversity Assessment. UNEP. Cambridge University Press, Cambridge, UK.

IPCC (Intergovernmental Panel on Climate Change). 2007[a]. Climate Change 2007: The physical science basis. In: Contribution of Working Group I to the Fourth assessment report of the Intergovernmental Panel on Climate Change. Cambridge University Press, Cambridge, United Kingdom. 235- 336.

Janzen, FJ. 1994. Climate change and temperature dependent sex determination in reptiles. Proc. Natl. Acad. Sci. USA. 91:7484-7490.

Kappelle, M., Van Vuuren, MMI. and Baas, P. 1999. Effects of climate change on biodiversity: a review and identification of key research issues. Biodiversity & Conservation. 8(10):1383-1397.

Khan, MZ. 2006. Impacts of Climate Change and Environmental Pollution on Ecosystem and Wildlife. J. Exp. Zool. India. 9 (1):77-84.

Kiesecker, JM., Blaustein, AR. and Belden, LK. 2001. Complex causes of amphibian population declines. Nature. 410:681-684.

Kullman, L. 1983. Past and present tree lines of different species in the Handolan Valley, Central Sweden. Eds. Morisset, P. and Payette, S. Tree Line Ecology Centre d'Etude Nordiques de l'Université Laval, Québec. 25-42.

Liu, SY., Ding, YJ., Li, J., Shangguan, DH. and Zhang, Y. 2006. Glaciers in response to recent climate warming in Western China. Quaternary Sciences. 26:762- 771.

MacArthur, RH. and Wilson, EO. 1967. The Theory of Island Biogeography. Princeton University Press, Princeton, NJ, USA.

Magnuson, JJ., Robertson, DM., Barbara, JB., Wynne, RH., Livingston, DM., *et al*. 2000. Historical Trends In Lake And River Ice Cover In The Northern Hemisphere. Science. 289(5485):1743-1746. DOI: 10.1126/science. 289.5485.1743

Milner, JM., Elston, DA. and Albon, SD. 1999. Estimating the contributions of population density and climatic fluctuations to inter-annual variation in survival of Soay sheep. J. Anim. Ecol. 68:1235-1247.

Myers, N. 1979. The Sinking Arc. Pergamon Press, Oxford.

Myers, N. 1988. Threatened biotas: 'Hot spots' in tropical forests. The Environmentalist. 8:187-208.

Myers, N. 1989. Deforestation Rates in Tropical Forests and Their Climate Implications. Friends of the Earth, London.

NASA. 2019. Natural causes of climate change. Climate Science Investigations, South Florida, USA.

Parmesan, C. 2006. Ecological and evolutionary responses to recent climate change. Ecology Evolution. 37:637-669.

Peters, RL. and Lovejoy, TE. 1992. Global Warming and Biological Diversity. Yale University Press, New Haven, CT., USA. pp 386.

Post, E. and Forchhammer, MC. 2001. Pervasive influence of large-scale climate in the dynamics of a terrestrial vertebrate community. BMC Ecol. 1:5.

Post, E. and Stenseth, NC. 1999. Climatic variability, plant phenology, and northern ungulates. Ecology. 80: 1322-1339.

Post, E., Peterson, RO., Stenseth, NC. and McLaren, BE. 1999. Ecosystem consequences of wolf behavioral response to climate. Nature. 40:905-907.

Post, E., Stenseth, NC., Langvatn, R. and Fromentin, JM. 1997. Global climate change and phenotypic variation among red deer cohorts. Proc. R. Soc. Lond. B. 264: 1317-1324.

Pounds, JA., Fogden, MPL. and Campbell, JH. 1999. Biological response to climate change on a tropical mountain. Nature. 398:611-615.

Rafi, F. and Riaz, DU. 2018. Climate Change and its effects on Pakistan. Weekly Technology Times.

Rahel, FJ. and Olden, JD. 2008. Assessing the effects of climate change on aquatic invasive species. Conservation Biology. 22(3):521-533.

Rabani, RR. *et al*. 2008. The Impact of Sea Level Rise on Pakistan's Coastal Zone in a Climate Change Scenario. National Institute of Oceanography. Second International Maritime Conference, Bahria University, Karachi.

Ren, JW., Qin, DH., Kang, SC., Hou, SG., Pu, JC. and Jing, ZF. 2004. Glacier variations and climate warming and drying in the central Himalayas. Chinese Science Bulletin. 49:65- 69.

Rhen, T. and Lang, JW. 1998. Among family variation for environmental sex determination in reptiles. Evolution. 52:1514-1520.

Root, TL., Price, JT., Hall, KR., Schneider, SH., Rosenzweig, C. and Pounds, JA. 2003. Fingerprints of global warming on wild animals and plants. Nature. 421(6918):57-60.

Shafer, DM. 2017. Climate Change Primer. Warm heart Partnering With Communities, Building Sustainable Futures.

Visser, ME. and Holleman, LJ. M. 2001. Warmer springs disrupt the synchrony of oak and winter moth phenology. Proc. R. Soc. Lond. B. 268:289-294.

Visser, ME., van Noordwijk, AJ., Tinbergen, JM. and Lessels, CM. 1998. Warmer springs lead to mistimed reproduction in Great tits (*Parus major*). Proc. R. Soc. Lond. B. 265:1867-1870.

Warren, R., Price, J., Van Der Wal, J., Cornelius, S. and Sohl, H. 2018. The implications of the United Nations Paris Agreement on Climate Change for Globally Significant Biodiversity Areas. Climatic Change.

WWF[a]. 2019. Threats: Effects of climate change.

WWF[b]. 2019. Marine Problems: climate change.

WWF. 2018[a]. Wildlife in a Warming world: The Effects of Climate Change on Biodiversity in WWF's Priority Places. WWF, UK.

WWF. 2018[b]. Wildlife in a Warming World: The Effects of Climate Change on Biodiversity. WWW.Worldwildlife.org/publications.

Ye, Q. and Yao, TD. 2008. Glacier and lake variations in some regions on Tibetan Plateau using remote sensing and GIS technologies. In Geophysical research abstracts. 10:1607-792.

Zemp, M. 2008. Global glacial changes: facts and figures. World Glacier Monitoring Service, Zurich, Switzerland.

Received: Sept 7, 2021; Revised: Sept 30, 2021;
Accepted: Oct 7, 2021

Canadian Journal of Pure and Applied Sciences
Vol. 15, No. 3, pp. 5353-5358, Oct 2021
Online ISSN: 1920-3853; Print ISSN: 1715-9997
Available online at www.cjpas.net

A REVIEW ON THE BOOK BY KHMELNIK: NAVIER-STOKES EQUATIONS ON THE EXISTENCE AND THE SEARCH METHOD FOR GLOBAL SOLUTIONS

Aleksey Anatolievich Zakharenko
International Institute of Zakharenko Waves, Krasnoyarsk, Russia

ABSTRACT

In 2010, Khmelnik has developed his theoretical method applicable for resolving problems existing in mechanics, electrodynamics, electrical engineering, hydrodynamics. For hydrodynamics, this method allowed for Khmelnik to resolve the Navier-Stokes equations. However, this work by Khmelnik is not widely known. As a result, there are still both analytical and numerical attempts to find a suitable method of resolving of the Navier-Stokes equations. The work by Khmelnik provides the obtained results in both analytical forms and color graphical three-dimensional illustrations. Therefore, this review has the purpose to briefly acquaint the reader with the resolving method that was successfully applied to the Navier-Stokes equations and the other problems in physics.

Keywords: Navier-Stokes equations, hydrodynamics, lagrangian formalism, compressible and incompressible fluids, turbulent flow.

INTRODUCTION

It is mentioned in (Bratsun and Vyatkin, 2019) that in hydrodynamics at pre-computer times, to find exact solutions for some cases described by hydrodynamic equations was irreplaceable event. Indeed, to obtain exact solutions means to have the key tools for fluid motions' obtaining information. Let's mention here some classical examples: the Taylor flow confined between two rotating coaxial cylinders (Taylor, 1923), the Poiseuille flow in a pipe under applied pressure drop (Poiseuille, 1840), and the Couette flow between two surfaces, one of which is moving tangentially relative to the other (Couette, 1890).

However, there are problems in hydrodynamics that still are unresolved during the last centuries. One of such problems is the Navier-Stokes equations. The importance of resolving of the Navier-Stokes equations consists in their multi-promising applications. As a result, the Clay Mathematics Institute (CMI), see here http://www.claymath.org/millennium-problems/navier%E2%80%93stokes-equation, has included this problem in the list of the seven most important mathematical problems to be resolved in this millennium, see also in (Ladyzhenskaya, 2003). Khmelnik from Israel has stated that he has resolved the Navier-Stokes equations and he has published his method of resolving of the Navier-Stokes equations in 2010 in both Russian (Khmelnik, 2010a) and English (Khmelnik, 2010b). Several years ago, Dr. Khmelnik has contacted to the Clay Mathematics Institute, sending his book with his method of resolving of the Navier-Stokes equations and claiming that he has resolved this problem. The Clay Mathematics Institute has answered that somebody (but not Dr. Khmelnik himself) should introduce the work by Khmelnik to the CMI in or-der that the CMI can treat his method.

This review has the purpose to quaint the reader with already the sixth edition (Khmelnik (2021)) of his results initially published in 2010 (Khmelnik, 2010a, 2010b). This last sixth edition of the book represents the three-books-in-one edition because two books by Khmelnik (2018a, 2018b) with the computer programs in the MATLAB codes and their explanations, respectively, were added as Appendices 8 and 9 to the fifth edition (Khmelnik, 2018c) of his book to compose the sixth edition. So, the book by Khmelnik (2021) is supplemented by the corresponding computer program codes of the MATLAB platform, namely by functions that realize the calculation method and the computer program test codes.

In his book, Khmelnik (2010b, 2018, 2021) starts with the Lagrangian formalism in Chapter 1 and introduces the Energian that can be understood as an extended or modified Lagrangian. It is well-known that the Lagrangian formalism is used for many problems of physics, for instance, it was recently applied for antimatter gravity study (Jentschura, 2020). So, the main formulas in the book Khmelnik (2021) are written down

Corresponding author e-mail: aazaaz@inbox.ru

in Chapters 1 and 2 as well as in the appendices from 1 to 7. The obtained method by Khmelnik can be applied to many problems. Today the reader can find a lot of literature where the Navier-Stokes equations are used. For instance, within the last several years it is possible to find ~ 100 published papers among only the MDPI Journals such as Mathematics, Fluids, and Mathematical and Computational Applications. This review has no objective to review all of them. However, it is possible to mention some of them to demonstrate different problems where the Navier-Stokes equations can be applied.

Ersoy *et al*. (2021) have derived the model via asymptotic reduction from the two-dimensional Navier-Stokes equations under the shallow water assumption, with boundary conditions including recharge via ground infiltration and runoff. Ersayın and Selimefendigil (2013) have numerically investigated the effects of various parameters such as nanoparticle volume fraction, pulsating frequency, plate velocity, Reynolds number on the heat transfer characteristics, where the Navier-Stokes equations and energy equations are solved with a commercial finite volume based code. Moschandreou (2018) has proposed a solution to the three-dimensional Navier-Stokes equations in the cylindrical coordinates coupled to the continuity and level set convection equation. Akkari *et al.* (2019) have considered the problem of constructing a time stable reduced order model of the three-dimensional Navier-Stokes equations in the incompressible and turbulent case. Semenov (2014) has discussed the exact estimates for solutions in the Cauchy problem for the Navier-Stokes equations and Euler equations. Metivet *et al*. (2018) have presented the simulation of multifluid flows based on the implicit level-set representation of interfaces and on an efficient solving strategy of the Navier-Stokes equations. In the study by Kang and You (2021), a cell-centered finite-volume method for compressible Naiver-Stokes equations was developed. Saito (2021) has shown time-decay estimates of solutions to linearized two-phase Navier-Stokes equations with surface tension and gravity. Galdi (2021) has provided conditions for the occurrence of time-periodic Hopf bifurcation for the coupled system constituted by a rigid sphere moving under gravity in a Navier-Stokes liquid. The paper by Azlan *et al*. (2021) has studied the linearized problem for the compressible Navier-Stokes equation around space-time periodic state. Kubo and Shibata (2021) have treated the problem formulated mathematically by the Navier-Stokes equations in a time-dependent domain separated by an interface, where one part of the domain is occupied by a compressible viscous fluid and another part by an incompressible one. Aksenov and Polyanin (2021) have described a number of simple methods for constructing exact solutions of nonlinear partial differential equations, including the Navier-Stokes equations, that involve a relatively small amount of intermediate calculations. Bourantas (2021) has studied a model consisting of the Navier-Stokes equations expressed in the velocity-vorticity variables including the energy and microrotation transport equation. For the Navier-Stokes equations, Yakhlef and Murea (2021) have used the fictitious domain method with penalization. Mimeau and Mortazavi (2021) have reviewed the vortex methods belonging to Lagrangian approaches and allowing one to solve the incompressible Navier-Stokes equations in their velocity-vorticity formulation. The work by Sarthou *et al*. (2020) has studied the interactions between fictitious-domain methods on structured grids and velocity–pressure coupling for the resolution of the Navier-Stokes equations. Murea (2019) has used the updated Lagrangian framework for the linear elasticity equation modeling the structure and the Navier-Stokes equations governing the fluid. In (Jabbari *et al*., 2019), a first-order projection method was used to numerically solve the Navier-Stokes equations for a time-dependent incompressible fluid inside a 3D lid-driven cavity.

Also, there are a lot of publications where the method called the Reynolds-averaged Navier-Stokes equations (or RANS equations) is used. among the aforementioned 100 articles on the Navier-Stokes equations, at least half of them refers to this specified method. For instance, Huilier (2021) has stated that instead of Reynold-Averaged Navier-Stokes (RANS)-based studies, the computer evolution and performance allowed development of large eddy simulation (LES) and direct numerical simulation (DNS) of turbulence coupled to Generalized Langevin Models. A dual approach is applied in (Wenig *et al*., 2021), in which the LES is used as reference for the unsteady RANS computations. Mai and Ryu (2021) have used the RANS equation coupled with the turbulence model to solve the problem of high-speed and high-pressure compressible flow through the gas-turbine model. In (Lluesma-Rodríguez *et al.*, 2021), it was designed a numerical method to solve the time-dependent incompressible 3D Navier-Stokes equations in turbulent thermal channel flows. Also, Lluesma-Rodríguez *et al*. (2021) state that it is well-known that we still even lack an existence and uniqueness theorem about the solution of the governing equations of turbulent flows, the Navier-Stokes equations.

In Chapter 4 of the book by Khmelnik (2021), it is discussed that strictly speaking the treated RANS equations cannot be called Navier-Stokes equations and the considered method of constructing the functional is not applicable to them. In Chapter 10 of the book, the other method of calculation of turbulent flows is demonstrated. For turbulent flows, some equations similar to the Navier-Stokes equations can be obtained. Next, a functional can be constructed for the obtained turbulent flow equations and these equations represent the necessary conditions for the existence of the extremum

for this constructed functional. The turbulent flow equations are equations (10.8.1) and (10.8.1) in Subsection 10.8 of Chapter 10 in the book by Khmelnik (2021). This functional is not convex. Therefore, there may be more than one solution for these turbulent flow equations, read the context after equation (10.8.9) in Subsection 10.8. However, there are flows with weak turbulences, which can be represented by the sum of a high-speed laminar flow and a turbulent flow with relatively low speeds. Such flows are described by two independent set of equations and there are unique solutions for each of these sets, see the algorithm at the end of Subsection 10.8.

The author of this review is familiar with many published papers and books by Solomon Itskovich Khmelnik from Israel, including his work on the Navier-Stokes equations (Khmelnik, 2021)and has contacts with him already during the last two years. The author has found that Khmelnik has developed a variational principle that can be applied to dissipative systems. This review has no aim to rewrite all the results obtained by Khmelnik (the reader must read his book (Khmelnik, 2021)) but only concisely acquaints the reader with the main results obtained by Khmelnik and states that namely the Navier-Stokes equations were resolved by Khmelnik in 2010, according to his first work published in both Russian (Khmelnik, 2010a) and English (Khmelnik, 2010b).

The concise description of the method by Khmelnik (2021)

If in the existing principle the integrand is the difference between the kinetic energy and the potential energy, then in the proposed functional the integrand is the difference (ΔH) between the kinetic energy and the sum of the potential and thermal energies. In the absence of a dissipation process, such an expression turns into Lagrangian. When constructing a functional, each desired function splits into two independent functions, and the functional contains pairs of such split functions. The integrand itself depends on pairs of independent split functions. The optimum of a functional is the saddle point where one group of split functions minimizes the functional and the other maximizes it. The sum of the pair of optimal values of these split functions gives the desired function. The variational principle in this case states that the extremals of this functional (defining the saddle point) are real dynamic variables that can be realized in reality. Khmelnik calls it the principle of general action.

This principle allows one to design a functional for various physical systems and, most importantly, for dissipative systems. This functional has a global saddle point. Therefore, to calculate physical systems with this functional, one can apply the method of gradient descent to the saddle point. The solution always exists because the global extremum exists. The initial step in constructing this functional is as follows: for some physical system, the energy conservation equation or the power balance equation is written, taking into account both energy losses (for instance, friction or heating) and the flow of energy into and out of the system.

The proposed variational principle allows one to construct a functional for various physical systems with a single saddle point of the optimum. Khmelnik also proposed a computational method for moving to the saddle point, which allows one to calculate the extremals of this functional. Therefore, the real equations of motion for some treated system can be determined. Thus, the new formalism is not only a universal method for deriving physical equations from a certain principle but also a way to calculate these equations.

Khmelnik has applied this principle to various physical problems. First of all, the proposed formalism is applicable to electrical circuits. It should be noted that for DC circuits (where there are only resistances) the solution was found by Maxwell, who showed that the currents are distributed in such a way that they minimize heat losses. However, for AC electrical circuits, a principle similar to the principle of least action has not yet been found in spite of the fact that there were many attempts. These searches are understandable because the absence of the principle of extremality for electrical circuits seems strange. The proposed variational principle for electrical circuits is such that it follows from the Kirchhoff equations for AC electrical circuits. This means that there is a definite integral of the split functions of charges, which are functions of time. This integral has a single optimum point and its extremals coincide with the Kirchhoff equation. Thus, in the electrical circuit, the principle of the extremum of the aforementioned value of ΔH is objectively observed.

This functional can be also found for electric power systems, which are nonlinear electrical circuits. It is shown that the resulting functional is optimized when the stationary value of the integrand function is the equation of the power system mode. Khmelnik has also demonstrated that the solution of a set of linear algebraic equations is also reduced to the calculation of an electric circuit of sinusoidal currents by the proposed method. It was shown that the solution of sets of partial differential equations also reduces to the search for the optimum of a certain functional. For instance, the equations of Poisson, Helmholtz for homogeneous and inhomogeneous media, the telegraph equation, and many others can be resolved by the proposed method. In addition, this principle is generalized to electromechanical systems. For some treated electromechanical system, the formed functional contains thermal, mechanical, electrical, and magnetic energies, functions depending on the configuration of the treated system, and functions describing perturbations'

effects both electrical and mechanical. The same method can be readily applied to Maxwell's equations, which involve currents in a medium with a certain electrical conductivity. Therefore, there is a heat loss, i.e. energy dissipation. This means that in addition to electric and magnetic energies, the functional for the principle of minimum action must include thermal energy. Hence, the Lagrange formalism for Maxwell's equations is not applicable in this case.

It should be mentioned that the calculus of variations has one drawback because it is assumed that the functions are continuous. In practice, discontinuous functions such as the Dirac function and step functions are often found. For optimization problems with such functions there is a Pontryagin maximum method. Khmelnik has demonstrated that the Pontryagin maximum method can be combined with the method of gradient motion to the saddle point. As a result, an algorithm for resolving a set of Maxwell's differential equations with discontinuous perturbations is formulated. All calculations in this algorithm consist of operations with coefficients of polynomial functions. The result is also given in the form of polynomial functions, i.e. an analytical solution is obtained.

The most interesting thing is how Khmelnik has applied this principle in hydrodynamics, namely to the problem of proving the uniqueness of the solution of the Navier-Stokes equations that has not been resolved for the last couple of centuries. As an outstanding researcher, Khmelnik works alone already for a long time and therefore, his results are not widely known, although the solution to this problem was first published in 2010 in Russian (Khmelnik, 2010a) and then in 2010 in English (Khmelnik, 2010b). In this regard, it is necessary to briefly describe below the resolving method found by Khmelnik. This method is suitable for the three-dimensional case. It worce here noting that in the two-dimensional case, the the solution metod has been knownfor a long time (Ladyzhenskaya, 1969), also for the more difficult case of the Eulerequations. However, this gives no hint about the three-dimensional case because the maindifficulties are absent in the two-dimensional case.

The resolving method by Khmelnik (2021) for the Navier-Stokes equations

First of all, Khmelnik offers that the following functional (certain integral) can be called some full action: $\Phi(q) = \int_{t_1}^{t_2} \Re(q)dt$, where $\Re(q) = (K(q) - P(q) - Q(q))$ is called the Energian by Khmelnik (by analogy with the Lagrangian.) $K(q)$, $P(q)$, $Q(q)$ are the kinetic, potential, and thermal energies, respectively. q is a vector of generalized coordinates, dynamic variables that depend on time t. Here, the integral is taken at a certain time interval $t_1 \le t \le t_2$. It should be noted here that when $Q = 0$, the functional $\Phi(q)$ turns into some action.

Next, it is natural to consider the quasi-extremal of the full action, which has the following form:

$$\frac{\partial(K-P)}{\partial q} - \frac{d}{dt}\left(\frac{\partial(K-P)}{\partial q'}\right) - \frac{\partial Q}{\partial q} = 0 \qquad (1)$$

The functional $\Phi(q)$ definitely takes an extreme value on quasi-extremals. The principle of extremum of full action states that the quasi-extremals of this functional are equations of real dynamic processes. It is possible to determine the extreme value of the functional $\Phi(q)$. For this purpose, it is possible to split the function $q(t)$ into two independent functions $x(t)$ and $y(t)$, and to correspondingly treat the following functional instead of the functional $\Phi(q)$: $\Phi_2(x,y) = \int_{t_1}^{t_2} \Re_2(x,y)dt$ called the "split" full action. The function $\Re_2(x,y)$ is called the "split" Energian. This functional is minimized by the function $x(t)$ for a fixed function $y(t)$ and maximized by the function $y(t)$ for a fixed function $x(t)$. The minimum and maximum are the only ones.

Thus, the extremum of the functional $\Phi_2(x,y)$ is a saddle line, where one group of functions (x_0) minimizes the functional, and the other (y_0) maximizes it. The sum of the pair of optimal values of the split functions gives the desired function $q = x_0 + y_0$, which satisfies the aforementioned equation of quasi-extremal (1). In other words, the quasi-extremal of the functional $\Phi(q)$ is the sum of the extremals (x_0, y_0) of the functional $\Phi_2(x,y)$, which determine the saddle point of this functional. It is important to note that this point is the only extreme point because there are no other saddle points and no other minimum or maximum points. This is the meaning of the expression "extreme value on quasi-extremals". The statement is that in every field of physics, one can find a correspondence between the complete action and the split complete action, and thus prove that the complete action takes on a global extreme value on quasi-extremals.

In order to show the validity of this statement for hydrodynamics, Khmelnik uses the well-known work of Umov, who considered for a liquid the condition of the balance of specific (by volume) capacities in the liquid flow for both incompressible and compressible liquids. From this condition, after long transformations, it is possible to find the quasi-extremal equation. Next, Khmelnik constructs a computational algorithm. Stationary and dynamic problems are also considered, and the proposed algorithm is implemented in MATLAB program codes. Examples of flows are also shown graphically and corresponding MATLAB program codes are also considered in the book.

Let's also shortly introduce the ten chapters of the book. Chapter 1 acquires the reader with the principle of extremum of full action. Chapter 2 this principle for viscous incompressible fluids. Chapter 3 briefly discusses the computational algorithms applied. Chapter 4 concisely discusses the method called the Raynolds-average Navier-Stokes equations (RANS equations) stating that strictly speaking the RANS equations cannot be called Navier-Stokes equations and the method of constructing the functional is not applicable to the RANS equations. Chapters 5 and 6 treat the stationary and dynamic problems, respectively. Chapters 7 and 8 provide the following examples: Computations for a mixer and flow in a pipe, respectively. In Subsections 7.2 and 7.3 of Chapter 7, the polar and Cartesian coordinates are also treated. In these chapters, the results are also shown graphically in eleven and thirteen figures, respectively, some of them are three-dimensional plots. Chapter 9 describes the principle of extremum of full action for viscous compressible fluids. Chapter 10 represents the emergence mechanism and calculation method of turbulent flows. In this chapter, the results were also graphically shown in eleven figures, some of them are three-dimensional plots. In addition, this book also contains nine appendices, of which the first seven contain a lot of complicated formulas used by Khmelnik in his work. Appendices 8 and 9 contain the relevant computer programs in the MATLAB codes and their explanations, respectively.

CONCLUSION

It is suggested that the reader pay attention to the book on the obtained method of resolving of the Navier-Stokes equations. Indeed, his work has many practical applications.

REFERENCES

Akkari, N., Casenave, F. and Moureau, V. 2019. Time stable reduced order modeling by an enhanced reduced order basis of the turbulent and incompressible 3D Navier-Stokes equations. Mathematical and Computational Applications. 24(2):45. DOI: https://doi.org/10.3390/mca24020045.

Aksenov, AV. and Polyanin, AD. 2021. Methods for constructing complex solutions of nonlinear PDEs using simpler solutions. MDPI Mathematics. 9(4):345. DOI: https://doi.org/10.3390/math9040345.

Azlan, MN., Enomoto, S. and Kagei, Y. 2021. On the spectral properties for the linearized problem around space-time-periodic states of the compressible Navier-Stokes equations. MDPI Mathematics. 9(7):696. DOI: https://doi.org/10.3390/math9070696.

Bourantas, GC. 2021. Micropolar blood flow in a magnetic field. MDPI Fluids. 6(3):133. DOI: https://doi.org/10.3390/fluids6030133.

Bratsun, D. and Vyatkin, V. 2019. Closed-form non-stationary solutions for thermo and chemovibrational viscous flows. MDPI Fluids. 4(3):175. DOI: https://doi.org/10.3390/fluids4030175.

Couette, M. 1890. Ètudessur le frottement des liquides. Ann. Chim. Phys. 21:433-510.

Ersayın, E. and Selimefendigil, F. 2013. Numerical investigation of impinging lets with nanofluids on a moving plate. Mathematical and Computational Applications. 18(3):428-437. DOI: https://doi.org/10.3390/mca18030428.

Ersoy, M., Lakkis, O. and Townsend, P. 2021. A Saint-Venant model for overland flows with precipitation and recharge.Mathematical and Computational Applications. 26(1):1. DOI: https://doi.org/10.3390/mca26010001.

Galdi, GP. 2021. On time-periodic bifurcation of a sphere moving under gravity in a Navier-Stokes liquid. MDPI Mathematics. 9(7):71. DOI: https://doi.org/10.3390/math9070715.

Huilier, DGF. 2021. An overview of the Lagrangian dispersion modeling of heavy particles in homogeneous isotropic turbulence and considerations on related LES simulations. MDPI Fluids. 6(4):145. DOI: https://doi.org/10.3390/fluids6040145.

Jabbari, M., McDonough, J., Mitsoulis, E. and Hattel, JH. 2019. Application of a projection method for simulating flow of a shear-thinning fluid. MDPI Fluids. 4(3):124. DOI: https://doi.org/10.3390/fluids4030124.

Jentschura, UD. 2020. Antimatter gravity: Second quantization and Lagrangian formalism. MDPI Physics. 2(3):397-411. DOI: https://doi.org/10.3390/physics2030022.

Kang M. and You, D. 2021.A low dissipative and stable cell-centered finite volume method with the simultaneous approximation term for compressible turbulent flows.MDPI Mathematics. 9(11):1206. DOI: https://doi.org/10.3390/math9111206.

Khmelnik, SI. 2010[a]. Navier-Stokes Equations.On the Existence and the Search Method for Global Solutions. Published by "MiC" - Mathematics in Computer Corp., printed in the USA, Lulu Inc., ID 8828459, Israel. ISBN 978-0-557-48083-8 (in Russian). DOI: https://doi.org/10.5281/zenodo.5057229.

Khmelnik, SI. 2010[b]. Navier-Stokes Equations.On the Existence and the Search Method for Global Solutions (1st ed.). MiC - Mathematics in Computer Corp., Lulu Inc., USA. ID 9036712, Israel. ISBN 978-0-557-54079-2. (In English) DOI: https://doi.org/10.5281/zenodo.5037593.

Khmelnik, SI. 2018[a]. PROGRAMS for Solving the Equations of Hydrodynamics in the MATLAB SYSTEM. MiC- Mathematics in Computer Corp. Lulu Inc., USA. ID 22833773, Israel. ISBN978-1-387-77626-9.http://www.lulu.com/content/22833773

Khmelnik, SI. 2018[b]. Fluid Flow in Tube with Obstacle: The New Calculation Method and the MATLAB-program. MiC - Mathematics in Computer Corp. Lulu Inc., USA. ID 22407028, Israel. ISBN978-1-387-50952-2. DOI: https://doi.org/10.5281/zenodo.3924902.

Khmelnik, SI. 2018[c]. Navier-Stokes Equations.On the Existence and the Search Method for Global Solutions. (5th ed.). MiC- Mathematics in Computer Corp., Lulu Inc., USA. ID 9971440, Israel. ISBN 978-1-4518-1953-1. (In English) DOI: https://doi.org/10.5281/zenodo.1307614.

Khmelnik, SI. 2021. Navier-Stokes Equations. On the Existence and the Search Method for Global Solutions. (6th ed.). MiC - Mathematics in Computer Corp., Lulu Inc., USA. ID kg2gpm, Israel. ISBN 978-1-6780-5491-5. (In English) DOI: http://doi.org/10.5281/zenodo.5090021

Kubo, T. and Shibata, Y. 2021. On the evolution of compressible and incompressible viscous fluids with a sharp interface. MDPI Mathematics. 9(6):621. DOI: https://doi.org/10.3390/math9060621.

Ladyzhenskaya, OA. 1969. The Mathematical Theory of Viscous Incompressible Flows. (2nd ed.). Gordon and Breach, New York, USA.

Ladyzhenskaya, OA. 2003. Sixth problem of the millennium: Navier-Stokes equations, existence and smoothness. Russian Mathematical Surveys. 58(2):251-286. DOI:https://doi.org/ 10.1070/ RM2003v058n02ABEH000610.

Lluesma-Rodríguez, F., Álcantara-Ávila, F., Pérez-Quiles, MJ.and Hoyas, S. 2021. A code for simulating heat transfer in turbulent channel flow.MDPI Mathematics.9(7):756.DOI:https://doi.org/10.3390/math9070756.

Mai, TD. and Ryu, J. 2021. Effects of damaged rotor blades on the aerodynamic behavior and heat-transfer characteristics of high-pressure gas turbines. MDPI Mathematics. 9(6):627. DOI: https://doi.org/ 10.3390/ math9060627.

Metivet, T., Chabannes, V., Ismail M. and Prud'homme, C. 2018.High-Order Finite-Element Framework for the Efficient Simulation of Multifluid Flows. MDPI Mathematics. 6(10):203. DOI: https://doi.org/ 10.3390/ math6100203.

Mimeau, C. and Mortazavi, I. 2021. A review of vortex methods and their applications: From creation to recent advances. MDPI Fluids. 6(2):68. DOI: https://doi.org/ 10.3390/fluids6020068.

Moschandreou, TE. 2018. A new analytical procedure to solve two phase flow in tubes. Mathematical and Computational Applications. 23(2):26. DOI: https://doi.org/10.3390/mca23020026.

Murea, CM. 2019. Three-dimensional simulation of fluid–structure interaction problems using monolithic semi-implicit algorithm.MDPI Fluids. 4(2):94. DOI: https://doi.org/10.3390/fluids4020094.

Poiseuille, J. 1840. Récherches experiment ellessur le mouvement des liquids dans les tubes de trèspetitsdiamètres. Comptes Rendus. 11:961-967.

Saito, H. 2021. Time-decay estimates for linearized two-phase Navier-Stokes equations with surface tension and gravity. MDPI Mathematics. 9(7):761. DOI: https://doi.org/10.3390/math9070761.

Sarthou, A., Vincent, S. and Caltagirone, JP. 2020. Consistent velocity-pressure coupling for second-order L^2-penalty and direct-forcing methods. MDPI Fluid. 5(2):92. DOI: https://doi.org/10.3390/fluids5020092.

Semenov, VI. 2014. Some new integral identities for solenoidal fields and applications. MDPI Mathematics. 2(1):29-36. DOI: https://doi.org/10.3390/math2010029.

Taylor, GI. 1923. Stability of a viscous liquid contained between two rotating cylinders. Philos. Trans. R. Soc. Lond. A. 223:289-343.

Wenig, PJ.,Ji, R., Kelm, S. and Klein, M. 2021. Towards uncertainty quantification of LES and URANS for the buoyancy-driven mixing process between two miscible fluids-differentially heated cavity of aspect ratio 4. MDPI Fluids. 6(4):161 DOI: https://doi.org/10.3390/ fluids 6040161.

Yakhlef, O. and Murea, CM. 2021.Numerical simulation of dynamic fluid-structure interaction with elastic structure–rigid obstacle contact.MDPI Fluids. 6(2):51. DOI: https://doi.org/10.3390/fluids6020051.

Received: July 14, 2021; Revised: Aug 13, 2021;
Accepted: Sept 15, 2021